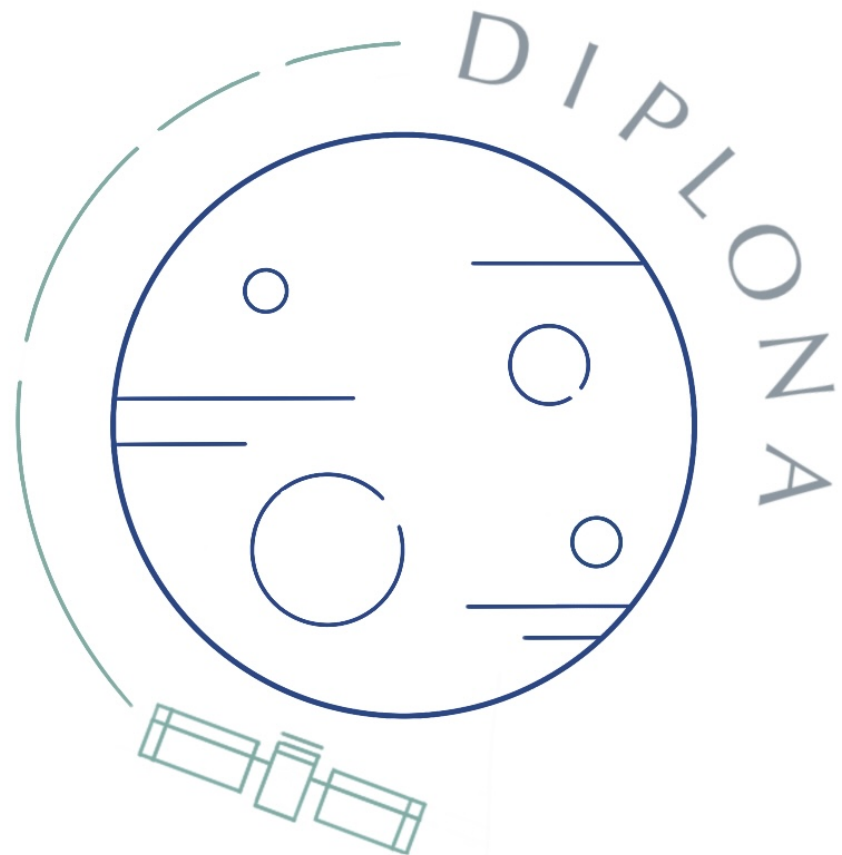


DIPLONA

A mission to Ceres: insights of the closest icy world



Alexandre Haubout, Allan Denis, Emma Vellard, Félix Vayrac, Iarotiana Rakotoharinandrasana, Mathieu Martinez, Md Salman Raza, Noé Le Becq, Noé Martin, Nolwenn Sire, Orianne Sohier, Théo St Georges

ESTACA 4th year and Planetary Science and Space Exploration MSc students
February 2023

Abstract

English version

Ceres is known as the smallest dwarf planet of the Solar System. To date only one mission has been able to reach Ceres and to provide results such as the first picture of the dwarf planet in 2015. The NASA Dawn mission has also provided information about cryovolcanism and other phenomena occurring on the surface but the knowledge about it are still limited.

Faced with this lack of understanding and insights to the closest icy world, a group made up of ESTACA engineers and scientists specialised in planetary sciences propose the Diplona mission. This study suggest to establish radar measurements of some key places of interest on Ceres in order to characterize some geophysical properties.

The Diplona mission proposed in this study is a 3U cubesat with a sounder radar on board. Once it reaches Ceres to study it's subsurface, a seven meters antennae is proposed to deployed to probe Ceres subsurface until tens of meter down with a few meters vertical resolution.

Ceres surface has various interesting areas to study in order to highlight cryovolcanism, ice and carbonate deposits. Four of these places have been proposed to be the best promising targets of the DIPLONA orbits: Occator, Haulani and Urvara craters and Ahuna Mons. The orbits followed by the spacecraft are also expected to cross secondary targets such as Juling and Ikapati craters or Samhain Catena.

French version

Cérès est connue comme la plus petite planète naine du système solaire. Une unique mission a été en mesure d'atteindre Cérès et de fournir des résultats tels que la première photo de la planète naine en 2015. La mission Dawn de la NASA a également fourni des informations sur le cryovolcanisme et d'autres phénomènes se produisant à la surface, mais les connaissances à ce sujet sont encore limitées.

Face à ce manque de compréhension, un groupe composé d'ingénieurs et de scientifiques de l'ESTACA spécialisés dans les sciences planétaires a conçu la mission DIPLONA. Cette mission a été créée pour établir des mesures radar de certains endroits clés d'intérêt sur Cérès afin de caractériser certaines propriétés géophysiques.

La sonde Diplona est un cubesat 3U équipé d'un radar sondeur. Une fois Cérès atteint pour étudier le sous-sol, une antenne de 7 mètres est déployée pour sonder le sous-sol de Cérès jusqu'à des dizaines de mètres de profondeur avec une résolution verticale de quelques mètres.

La surface de Cérès présente différentes zones intéressantes à étudier afin de mettre en évidence le cryovolcanisme, la glace et les dépôts carbonatés. Quatre de ces endroits ont été sélectionnés pour être les cibles principales des orbites de Diplona : les cratères Urvara, Haulani et Occator et le mont Ahuna. Les orbites suivies par le vaisseau spatial traversent également des cibles secondaires telles que les cratères Juling et Ikapati ou Samhain Catena.

Table of contents

1 Mission Overview	2
1.1 Definition of a SIMPLEx mission	2
1.2 Outline of the DIPLONA mission	2
2 Science Motivations for Ceres' Exploration	4
2.1 Before the Dawn mission	4
2.2 Insights from the Dawn mission	4
2.2.1 Composition of the cerean surface	5
2.2.2 Detection of organic compounds	7
2.2.3 Cryovolcanism and hydrothermalism	8
2.2.4 Other geomorphological structures on Ceres	10
2.2.5 Ceres' internal evolution	14
3 Scientific questions and mission objectives	16
3.1 Ceres: a new first-class target	16
3.2 A proper instrument to investigate Ceres characteristics	16
3.3 Main goals of Diploma mission	18
4 Diploma's Radar Sounder (DRS)	19
4.1 DRS in a nutshell	19
4.1.1 Data acquired by DRS	19
4.1.2 Heritage	19
4.2 Description of DRS	20
4.2.1 Design	20
4.2.2 Signal and data	25
4.3 Performances of DRS	32
4.3.1 Impact of topography on stretch processing parameters	32
4.3.2 Global performances	35
4.4 Summary	40
5 Cubesat dimensioning	41
5.1 Components	42
5.1.1 OnBoard Computer	42
5.1.2 Communication	43
5.1.3 Thermal control	43
5.1.4 Electric Power System	51
5.1.5 Attitude and Determination Control System	54
5.1.6 Structure	55
5.2 Payload	56
5.2.1 IDM-CIC	57
6 Mission Plan and Operations	61
6.1 Journey to Ceres	61
6.2 Orbit constraints: four main targets	64
6.2.1 Occator Crater	65
6.2.2 Ahuna Mons	67

6.2.3	Haulani Crater	69
6.2.4	Urvara Crater	71
6.3	Orbit determination	74
6.4	More than 60 possible secondary targets	76
6.5	Final instrument phases	78
6.5.1	Flight modes	78
6.5.2	Flight management	80
6.6	Planetary Protection Plan	80
7	Scientific data management	83
7.1	Size and shape of data	83
7.2	Data chain details	84
7.3	Post-processing of radargram data	84
8	Mission life cycle, planning and management	87
8.1	Scheduling : Mission phases	87
8.2	Phase-wise budget Estimation	88
8.2.1	Phase A: Concept and Technology development	90
8.2.2	Phase B: Preliminary design and technology completion	90
8.2.3	Phase C: Final design and fabrication	91
8.2.4	Phase D: System Assembly, Integration and Test, Launch	92
8.2.5	Phase E: Operations and Sustainment	92
8.3	Diplona overall team	94
9	Conclusion	96
10	Acknowledgement	97
11	Appendix	98
	Bibliography	99

List of Figures

1.1	The contribution of future Ceres exploration missions to the exploration of the solar system ocean worlds and their habitability. From [1, 2, 3]	3
2.1	Topographic Ceres Map obtain from the Dawn mission, Credit: NASA / JPL-Caltech / UCLA / MPS / DLR / IDA	5
2.2	a) Measured average spectrum of Ceres from visible and IR channels of Visible and Infrared spectrometer (VIR). b) Average spectrum of Ceres in the IR channel with error bars of calibration uncertainties and best fit (grey) as modeled including Mg-phyllosilicates, NH ₄ -phyllosilicates and Mg-Ca carbonate. Figure from [4].	6
2.3	Distribution of surface compounds in Oxo crater. a) Water ice, b) sodium carbonates, c) hydrated sodium carbonates. Abundances are derived from spectral fitting methods. The Figure comes from [4].	6
2.4	Distribution of the 3.4 μm band depth at the Ernutet crater region, on Ceres. Figure reproduced from De Sanctis et al. [5]	7
2.5	Simulated image of bright sodium carbonate deposits at the floor of Occator crater on Ceres (20°N, 240°E) using images from the Dawn mission, Credit: NASA/JPL-Caltech/UCLA/MPS/DLR/IDA.	8
2.6	Ahuna Mons, a cryovolcanic dome at the surface of Ceres. The top (3D image constructed from topography data) and bottom left images were obtained by the Dawn mission's Framing Camera. The bottom right image represents the sodium carbonate concentration labeled in color, on Ahuna Mons, Credit: NASA/JPL-Caltech/UCLA/MPS/DLR/IDA/ASI/INAF.	9
2.7	Schematic representation of a cryovolcano's structure and the ascent of the cryomagma to the surface. This representation is obviously simplified but allows a general perception of the mechanism.	9
2.8	Schematic and simplified representation of the Occator crater cross section. Carbonate deposits are shown at the floor of the crater with more or less liquid brine table at depth passing through fractures into the base of the crater[6].	10
2.9	Global geologic map of Ceres, produced using Low Altitude Mapping Orbit (LAMO) images as a basemap. This map is the unification of 15 quadrangles maps published in a series of papers in Icarus, Volume 316, December 2018, by Andrea Nass and David M. Nelson [7].	10
2.10	Morphologies of impact craters on Ceres. (A) Simple bowl-shaped crater (105°E and 3°N). (B) Modified simple crater (161.7°E and 13°S). (C) Complex crater (279°E and 23°S). (D)Complex crater with central peak (108°E and 10°N). (E) Achita, a polygonal complex crater (65.8°E and 25.8°N). (F) Gaue crater (84 km, 85.9°E and 30.9°N) showing multiple terraces, a central pit, a smooth and flat floor, and a small peak close to the central pit. (G) Dantu crater (125 km, 137.8°E and 24.4°N), with concentric terraces, a possible peak ring structure or central pit, a smooth and flat floor. (H) Urvara crater (170 km, 248.6°E and 46.3°S), with concentric terraces, a small elongated central peak, a smooth and flat floor, and a relaxed morphology. (I) Kerwan crater (284 km, 123.6°E and 10.9°S) with a partially relaxed morphology. Arrowheads point north. Figure from [8].	11

2.11 Examples of typical landslides of each class. Color indicates topography in meters. Bold triangles indicate the margin of the landslide. a) Type 1 landslide at 50.804°, 27.326°. b) Type 2 landslide at -48.723°, 4.457°. c) Type 3 landslide at 22.061°, -126.711°. Figure from [9].	12
2.12 Example of tectonic features from Dawn LAMO images. a) The pit chain of Samhain Catena. b) The floor fractures and the concentric fractures of Azacca crater.	13
2.13 Global interior structure for Ceres. [6]	14
4.1 Principles of a radar sounder.	19
4.2 Radargram obtained on Mars from SHAllow RADar (SHARAD). Credit : NASA / JPL-Caltech / University of Rome / Southwest research institute / University of Arizona.	20
4.3 (Left) - Radargram of Arsian Mons obtained by SHARAD. (Right) - Schematic representation of the 3 potential scenarios of subsurface stratigraphy interpreted from radargram. A : Scenario 1 - Stacked lava flows with vesiculated and less dense flows overlying very dense lava. B : Scenario 2 - Less dense lava flow and a thick tehra deposit overlying denser bedrock. C : Scenario 3 - Pyroclastic or other low-density material deposited over dense lava flows in the southern part of the caldera, adjacent to the wall [10]	20
4.4 View of Diplona's orientation from our IDM-CIC model, the dipole is fully deployed and the Diplona's Radar Sounder (DRS) is pointing toward Ceres.	21
4.5 This table is presenting all the critical elements of the payload.	21
4.6 Side view of our folded antenna in our IDM-CIC model on the side of the cubesat.	22
4.7 Diplona's side view still from our IDM-CIC model where we can observe the dipole's antenna completely deployed, hence measuring 7.3m.	23
4.8 Folding system used for the dipole. On the left side, we can see the elbow when the antenna will be folded and on the right side of the image the elbow is deployed. The figure is also coming from our IDM-CIC model.	23
4.9 Comparison between two commonly used alloys in space applications. The Al6061 is the alloy used for the satellite's structure. The Al7075 will be used for our DRS from ddprototype.com.	24
4.10 Illustration of the cross-correlation between a replica of the emitted signal and 2 far echoes. With the introduced notations, $\tau = 2 * 10^{-7}$ s, $f_0 = 40$ MHz. Distance between both targets is high enough to be able to resolve both targets.	26
4.11 Illustration of the cross-correlation between a replica of the emitted signal and 2 close echoes. With the introduced notations, $\tau = 2 * 10^{-7}$ s, $f_0 = 40$ MHz. Distance between both targets isn't high enough to be able to resolve both targets.	26
4.12 Principles of the linear frequency modulation.	27
4.13 (a) Illustration of the emitted signal and the reference delayed signal. (b) Illustration of the Intermediate Frequency (IF) signal generated for 2 close echoes. We see that the signals associated to the echoes are superimposed, which would lead to no targets resolution in the case of non linearly modulated frequency pulses. (c) Fast Fourier Transform (FFT) of the IF signals for 2 echoes $1 * 10^{-7}$ s apart. The peaks of the FFT happen for each target at a frequency called intermediate frequency and thus allow us to retrieve the time of arrival of the corresponding echoes. Even if echoes are close, we are able to resolve them. $\tau = 2 * 10^{-7}$ s, $\Delta f = 60$ MHz, $f_{min} = 10$ MHz, $t_{LO} = 2.5 * 10^{-7}$ s, $\tau_{LO} = 3 * 10^{-7}$ s.	29

4.14	Stretch processing block diagram.	30
4.15	Timing chart of DRS. Radio Frequency (RF) pulse width is set to $150 \mu\text{s}$. The local signal is generated $186 \mu\text{s}$ after the RF pulse. This value may change accordingly to the altitude of the spacecraft. The local signal width is set to $189 \mu\text{s}$, accounting for the maximum penetrating depth of DRS. This configuration is considered as the baseline configuration for DRS i.e. the configuration when there is no topography but may be slightly different depending on the altitude of the spacecraft.	31
4.16	Simulation of 3 echoes. FFT of the simulated IF signals. $\tau = 150 \mu\text{s}$, $\Delta f = 40 \text{ MHz}$, $f_{min} = 10 \text{ MHz}$, $t_{LO} = 186 \mu\text{s}$, $\tau_{LO} = 189 \mu\text{s}$. Peaks in the Fourier domain happen for each target at a frequency called Intermediate Frequency.	32
4.17	4 main targets of the mission and associated profiles (see part 6.2 for more details). Top left : Occator crater. Top right : Urvara crater. Bottom left : Haulani crater. Bottom right : Ahuna Mons. Images from Dawn LAMO mosaics.	34
4.18	Impact of topography of the 4 main targets on maximum expected Intermediate Frequency of the stretch processed signal. Parameters of the stretch processed signal : $\Delta f = 40 \text{ MHz}$, $\tau = 150 \mu\text{s}$. $t_{LO} = 157 \mu\text{s}$ (Occator crater), $211 \mu\text{s}$ (Urvara crater), $181 \mu\text{s}$ (Haulani crater), $163 \mu\text{s}$ (Ahuna Mons). Right : Intermediate Frequency for each target along the profiles drawn on figure 4.17. Left : Histogram of the Intermediate Frequency of each target.	34
4.19	Skin depth as a function of vertical resolution on Ceres.	35
4.20	Illustration of the radar equation.	36
4.21	calculated SNR for different RMS slopes.	37
4.22	Illustration of quantization of a signal.	37
4.23	Principle of SAR.	38
4.24	Hyperbolic curve traced by a point target in the azimuth range plane. Left : illustration of the variation of the distance between a point target and the satellite. Right : Hyperbolic curve also called range migration curve.	39
5.1	Different Cubesat sizes comparaison from AmericaSpace.com.	41
5.2	A picture of the Ka-Band Microchip Patch from Printech as an example of a Ka-band antenna for cubesat from satsearch.com.	44
5.3	Structure of Diplona, 1 is front side 5 is rear side.	47
5.4	Satellite temperature/time for 2 orbits. The red curve corresponds to the moment when the satellite passes into the Sun and the blue curve when it is in the shadow of Ceres.	49
5.5	Satellite temperature/time for its entire life. We notice that the temperature decreases until it stabilizes at around -19.5 degrees Celsius.	49
5.6	SimScale simulation, hot case / simulation, cold case. The sunny side is warmer and the temperature decreases along the satellite.	50
5.7	SimScale simulation, cold case with initial condition at infinity.	50
5.8	Power Management Unit (PMU): This is a picture of the GomSpace NanoPower P31u that will be used in the satellite from Gomspace.com.	52
5.9	PMU : A picture of the GomSpace NanoPower BPX from Gomspace.com.	52
5.10	View of Diplona's Solar Panels. We have four 3U solar panels deployed, two 3U solar panels on the side and one 1U solar panel on top of Diplona.	53
5.11	Attitude Determination and Control System (ADCS) subsystems. Description of the roles during an ADCS action.	54

5.12	ADCS subsystems. This graph gives us the link between the OnBoard Computer (OBC), Electrical Power System (EPS) and the ADCS system.	55
5.13	ISIS 3U, Diplona's Structure made in AL6061. www.isispace.nl.	56
5.14	Example of a dispenser: the ISISPOD 3U.	57
5.15	Assembly of Diplona. We have in pink, our payload composed of the DRS and the antennas on the side. In green, it's all the electric power system. In gray, the OBC is used to control the satellite. In blue, the communication system is combined with our TX/RX antennas. And finally, in brown we have the ADCS, used to control the position of the satellite. The solar and nadir sensor is used to know the geographic position of Diplona.	58
5.16	Diplona's Budget Mass from our Iteractive Data language Multi-mission altimetry and science (IDM-CIC). As we see, we are practically at 6kg with 20% of margin which allows us more possibilities for the next phases.	59
5.17	Diplona's Power Budget from IDM-CIC. It shows us the power we have during all the modes we will face during the mission.	59
5.18	Launch Mode. Everything is OFF, the dipole's antenna and the solar panels are folded onto the satellite sides. This model is coming from the IDM-CIC model. . .	60
5.19	Deployment mode. The solar panels and the radar are being deployed. This is what the first detumbling mode will look like. This model is coming from the IDM-CIC model.	60
5.20	Orbital mode. Everything is deployed and Diplona is in active mode this is how it will look after the first detumbling mode. This model is coming from the IDM-CIC model.	60
6.1	The Ceres Sample Return (Ceres Sample Return (CSR)) Solar Electric Propulsion (SEP)-lander spacecraft in cruise configuration from [2]. The total ΔV for the trip to Ceres will be achieved through solar electric propulsion (SEP) powered by solar panels nearly 25 metres long with 68.5 m^2 of active cell area.	62
6.2	Example trajectory of the cruise to Ceres piggybacking on the CSR mission for a launch in December 2030. The gravity assist around Mars would happens 8 month later in August 2031 and the arrival at Ceres' orbit would be in July 2037.	63
6.3	The four regions of high scientific interest considered as main targets in this report. The global map of Ceres is based on Dawn FC HAMO data in equal-area "Mollweide" projection. The photometrically corrected I/F reflectances are displayed in RGB color space ($R = R0.965\mu\text{m}$, $G = R0.749\mu\text{m}$, $B = R0.438\mu\text{m}$), showing differences in absolute reflectance and relative differences between color filters. The 4 side images of the targets are from NASA/JPL-Caltech/UCLA/MPS/DLR/IDA. . .	64
6.4	Left: Occator crater and its bright faculae, from a high-resolution mosaic from LAMO images. Right: Elevation profiles (from N to S) corresponding to the lines on the mosaic. The red one cross all the eastern side of the crater, and shows that no elevation change is associated to the bright spots of Vinalia Facula. The yellow profile is going through a topographic high ground (tholus) in the direct vicinity of the facula supposed to be made of massif material. The blue profile is going through the Cerealia Facula, showing that it is located in a depression. Radar profiles along those profiles would allow to understand the configuration of the contacts between all these geomorphological units.	65

6.5	Occator Crater geologic map from [11] on the LAMO mosaic (25 m/px) basemap at a scale of 1:200,000 and with a simple cylindrical projection. It is interesting to notice the bluish areas which correspond to the bright faculae, the black lines corresponding to fractures, pits and grooves, and the brighter crossed areas showing clusters of mounts and domes.	66
6.6	Left: Ahuna Mons, a possible cryovolcanic dome, from a high-resolution mosaic from LAMO images. Right: Elevation profiles corresponding to the lines on the mosaic.	67
6.7	Geological map of the Ahuna Mons region derived from Dawn data, with colors corresponding to units shown in the stratigraphic column, from [12]. Note the younger smooth unit surrounding Ahuna Mons and the ridges on summit unit. . . .	68
6.8	Left: Haulani crater, with possible cryo-domes in the center and a few pits around it in the carbonates deposits, from a high-resolution mosaic from LAMO images. Right: Elevation profiles corresponding to the lines on the mosaic.	69
6.9	Detailed geologic map of Haulani crater and surroundings illustrating the tectonic and geological history from [13].	70
6.10	Left: Urvara crater, with a very irregular floor with the presence of carbonates deposits , ammoniated phyllosilicates and salts and a possible cryo-dome in the center, from a high-resolution mosaic from LAMO images. Right: Elevation profiles corresponding to the lines on the mosaic.	72
6.11	Urvara Bassin geologic map on the LAMO mosaic (25 m/px) basemap, from [14]. It is interesting to notice the smooth material unit blanketing the older crater floor and terrace units. See also the central ridge and the grooves and pits in the basin floor.	72
6.12	STK Orbit Simulation, main specificities.	74
6.13	STK, one example of satellite's ground track with our near-polar orbit. Each colored rectangle correspond to a main target. Yellow for Occator, red of Ahuna, blue for Urvara and white for Haulani.	75
6.14	STK, flight over frequency for each of the four main targets. Every cross correspond to one fight over. The bigger is the target, the more flight over they are. . . .	75
6.15	STK, Ground Tracks on each target for a 50 days orbit simulation.	76
6.16	Synthesis of all components use in the different modes, you can find the detail and the explanation of each mode at 6.5.1. The color green represent a component completely activated, the orange represent a passive or limited state and the red means a component fully off.	80
6.17	Flights modes. We can clearly see how every mode presented is interacting with each other. The red arrows represent the errors that the OBC can detect, it will then automatically in detumbling mode to diagnostic any issues. In this representation, the acquisition mode include the reception of the waves.	80
6.18	Power consumption during all flight modes during one critical orbit, during this exceptionally power consuming orbit the cubesat is using the DRS to perform measurements before transferring data. Hence combining two extremely power consuming modes.	81
6.19	Assessment of the questions for the Categorization of Sample Return Missions from Small Solar System Bodies based on the COSPAR Planetary Protection Policy. Reproduced from [15].	82
7.1	Analog to Digital conversion of data.	83
7.2	Data Management Plan Functionnal Diagram.	84

7.3	(a) The waveform of sounder echo, (b) A-scan plot derived from the waveform data, (c) radargram in longitude of 69.5°W made by series of A-scan plots, and (d) radargram in longitude of 69.1°W. Figure reproduced from [16].	85
7.4	Illustration of the gain function. The gain function allows the correction of amplitude of reflectors given their time of arrival.	86
7.5	Illustration of how stacking improve signal to noise ratio.	86
8.1	Anticipated phase timelines for Diplona. The duration is not to scale.	88
8.2	Key Decision points and Reviews at each phases and transfers. The picture has been redrawn, reproduced, and adjusted as per Diplona requirements from the NASA project management handbook 2014 version.	89
8.3	Phase wise budget.	93
8.4	Budget percentage sector wise. Note how science and engineering represent half of the total mission budget, including only 6% for components (instrument and parts).	94
8.5	DIPLONA overall Team.	95
11.1	Multiple views of Diplona from our IDM CIC model.	98

List of Tables

4.1	AL7075 Composition from pa-international.com.	24
4.2	Parameters used for stretch processing on DRS.	30
4.3	Impacts of topography of the 4 main targets.	33
4.4	Parameters used for estimation of Signal-to-Noise Ratio (SNR).	37
4.5	Values of along-track resolution obtained for different altitudes.	39
4.6	Summary of DRS description.	40
5.1	Operating temperature ranges of all components.	44
5.2	Beam irradiance function of distance.	45
5.3	Material properties of Diplona.	46
5.4	Average of optical surface properties for partially covered surfaces.	47
5.5	Temperature of side oriented to Ceres.	48
6.1	Summary of the 2 European Space Agency (ESA) and 1 National Aeronautics and Space Administration (NASA) missions to Ceres proposed for the next decade. As the NASA Ceres Sample Return mission seems to be very advanced, keep in mind the two ESA missions seems to be only proposal and have not be investigated deeper for now.	61
6.2	Non-exhaustive list of possible secondary targets, classified by the feature type. IMxx landslides are taken from the list of [9]. Type 1 landslides are exhibit lobate, tongue-shaped morphology, with a well-defined toe. Type 2 landslides have a thin, sheet-like structure, distinctive toe, and long run-out length. Type 3 landslides are cuspatc and sheeted, characteristic of fluidized appearing ejecta.	78
8.1	Post Level names.	90
8.2	Key areas of Phase A and team required.	90
8.3	Key areas of Phase B and team required.	91
8.4	Key areas of Phase C and team required.	91
8.5	Key areas of Phase D and team required.	92
8.6	Key areas of Phase E and team required.	93

Glossary

A/D Analog to Digital. 28, 30, 33, 37, 38, 83

ACT Actuator. 54

ADCS Attitude Determination and Control System. vi, vii, 41–44, 54, 55, 58, 79

CAN Controller Area Network. 42, 43

CNES Centre National d'Etude Spatiale. 57

CNRS Centre national de la recherche scientifique. 90

CNSA China National Space Administration. 61

COSPAR Committee on Space Research. 80, 81

CSR Ceres Sample Return. vii, 2, 61–64, 96

DRS Diploma's Radar Sounder. v–viii, 19–21, 23, 25, 28, 30–32, 35, 37, 39, 40, 44, 56, 58, 66, 69, 71, 76, 81, 83

DSN Deep Space Network. 84

EPS Electrical Power System. vii, 41, 51, 54, 55

ESA European Space Agency. x, 19, 61–63

FC Dawn's Framing Camera. 10

FFT Fast Fourier Transform. v, vi, 28–30, 32

FPGA Field-Programmable Gate Array. 43

I2C Inter-Integrated Circuit. 42, 43

IDM-CIC Iteractive Data language Multi-mission altimetry and science. vii, 57, 59, 60

IF Intermediate Frequency. v, vi, 28–33, 83, 84

JUICE JUpiter Icry Moons Exploration. 20

KDP Key Decision Points. 88

LAMO Low Altitude Mapping Orbit. iv–vi, 10, 13, 34

LATMOS Laboratoire Atmosphères, Observations Spatiales. 92

LO Local Oscillator. 30

LRS Lunar Radar Sounder. 20

MARSIS Mars Advanced Radar for Subsurface and Ionosphere Sounding. 19, 20

MPPT Max Pointing Power Tracking. 51

MRO Mars Reconnaissance Orbiter. 19

NASA National Aeronautics and Space Administration. x, 4, 16, 19, 42, 43, 61, 62, 78, 79, 81, 87, 88, 90

OBC OnBoard Computer. vii, viii, 41–44, 55, 58, 78–80

PI Principal Investigator. 91

PMU Power Management Unit. vi, 51, 52

PSD Power Spectral Density. 36

RF Radio Frequency. vi, 31

RIME Radar for Icy Moons Exploration. 20

RMS Root Mean Square. 36

SELENE SELenological and ENgineering Explorer. 20

SEP Solar Electric Propulsion. vii, 62

SHARAD SHAllow RADar. v, 19, 20

sinc sinus cardinal. 28

SNR Signal-to-Noise Ratio. x, 25, 31, 36, 37

SPI Serial Peripheral Interface. 42

VIR Visible and Infrared spectrometer. iv, 4–7

Chapter 1

Mission Overview

1.1 Definition of a SIMPLEx mission

The SIMPLEx project, for Small, Innovative Missions for PLanetary Exploration, is a NASA-led project to assist in the development of small spacecraft to explore solar system bodies, except the Earth and the Sun.

To have a chance to be developed as SIMPLEx projects, these missions need to respect some constraints. They must not exceed a mass of 180 kg and be considered as secondary payloads on larger missions. Furthermore, the missions are intended to be low cost, under 55 million dollars excluding launch and operation costs. Despite these limited conditions, some SIMPLEx missions already had great results about Solar System objects such as hydrogen concentration on Moon surface or collision for low velocity particles in microgravity environment.

A SIMPLEx mission for a 3U cubesat has both limitations and advantages. Limitations include limitations on payload capacity, which can limit the scientific and technical capabilities of the mission, limitations on power, which can limit communication and instrument capabilities, limitations on lifespan due to limited propulsion and energy management systems, and limitations on orbital maneuvers which can limit trajectory and orbital positioning options. Advantages of a SIMPLEx mission for a 3U cubesat include relatively low cost for construction and launch compared to larger missions, speed of development and implementation of the mission, the ability to launch demonstration or educational missions, the ability to combine multiple cubesats for more complex missions, and the ability to launch missions in tandem with larger missions for complementary observations.

1.2 Outline of the DIPLONA mission

The flexibility of a SIMPLEx mission allows to study objects that are not really well known for now, ones that don't have many space missions dedicated to them. These kind of objects can be as well comets, asteroids or satellites. These last few years the study of icy moons has been one of the main field of investment in space exploration in order to try to answer the question of life. However, some other celestial bodies could answer this question according to their compositions and especially their water content.

Ceres is one such object. In addition to its scientific interest, the dwarf planet is one of the closest to Earth, making it one of the most accessible for a SIMPLEx space mission. The exploration of such an object will need several steps and missions as described in the Figure 1.1. The search for life will be the last step after identifying the ocean world, characterize them and access the habitability. Indeed life as we defined it requires specific condition and chemical element to have a chance to occur. The solvents or organics compounds have to be in an environment that provides physico-chemical conditions for life.

According to all these elements one past mission - Dawn - and three futures ones - CSR, Gauss and Diploma - have been developed. This report is a overview of the Diploma mission for the first step in its development. The mission results will complete the three others and highlight some specific

aspects such as the rock ocean interface and the search for a liquid reservoir. Diplona will use a sounder radar to explore the subsurface of Ceres. This kind of instrument is a all new instrument around Ceres and its development for a 3U cubesat is a real breakthrough in the field. The mission would allows us to answer three of the main fields of Ceres exploration as in Figure 1.1 and to be a cost-effective part of the strategy for exploring icy worlds.

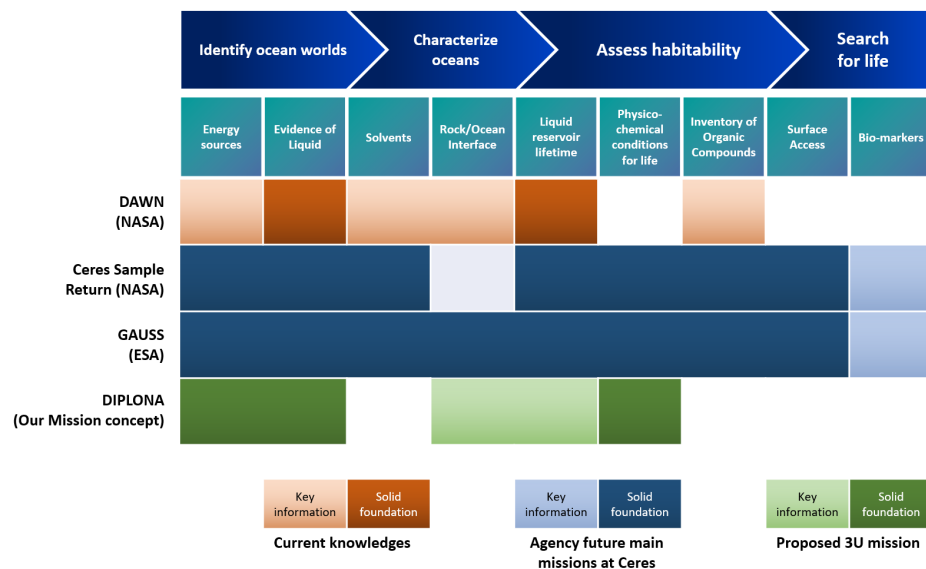


Figure 1.1: The contribution of future Ceres exploration missions to the exploration of the solar system ocean worlds and their habitability. From [1, 2, 3]

Chapter 2

Science Motivations for Ceres' Exploration

Ceres is a dwarf planet discovered by accident (but then lost) at the Palermo Astrophysical Observatory on January 1st, 1801, by the astronomer Giuseppe Piazzi. Its location was confirmed the same year in December by Frederich Gauss. Since 1768, the idea of an unknown planet between the orbits of Mars and Jupiter was suggested by the Titius-Bode law. Ceres was then considered at the time of its discovery as this missing planet. A past mission, the Dawn mission was able to bring new elements, a deeper knowledge of this unique body of the main asteroid belt. We will present in this part the scientific characteristics of this dwarf planet, the evolution of the knowledge and the perspectives and discoveries related to the Dawn mission.

2.1 Before the Dawn mission

Ceres is the most massive body of the asteroids belt, concentrating 30% of its mass. Its diameter is around 940 km, so about 1/13 the size of the Earth. Ceres is orbiting at 2.8 AU, has a sidereal orbit period of 1 682 days (4.6 Earth years) and a rotation period of 9h04. The orbit is markedly inclined from the ecliptic plan with an angle of 10.6°, the excentricity is of 0.0785 and the obliquity is of 4°, so there is no seasonal variations. Ceres was able to temporary capture asteroids in a 1:1 resonance, from 100 000 to 2 million years. It means that the dwarf planet Ceres stabilises asteroids in its vicinity, when Ceres makes a revolution around the Sun, asteroids also do one. Ceres shares spectral similarities with C-type asteroids, and has a really low albedo. The surface is relatively warm. Indeed, at the maximum of insolation, on the face exposed to the sun, the temperature is about 239K (average: 167 K).

It was known from calculation to have a low bulk density of 2100 kg/m^3 [6], intermediate between water ice and silicates which implies a really high bulk fraction of water. Thermal evolution models predicted that Ceres have differentiated into a stratified water-rich outer layer and a silicate core [6]. These models also predicted the existence of a past global subsurface ocean, and some even show that it would still be present. Ceres was then already known to be closer to a proto-planet than to an asteroid. That is why it is a celestial body of great interest and was selected to be visited by the Dawn mission.

2.2 Insights from the Dawn mission

On March 6, 2015, Ceres became the first dwarf planet to be visited by a spacecraft; the NASA Dawn mission. This mission towards two bodies of the main asteroid belt, Vesta and Ceres, aimed to better understand the solar system's less evolved bodies and furthermore the history of planetary formation. During more than three years, Dawn's spacecraft orbited around Ceres and performed geological, chemical and geophysical mapping of the body with multispectral imager, VIR, gamma ray and neutron detector, radio science, and stereoimagery for topography mapping, giving us a new high-resolution insight of Ceres.

Indeed, the spacecraft was able to map Ceres' global topography and geomorphology with a resolution of 35m (during the Low Altitude Mapping Orbit) using the onboard Framing Camera (see

Figure 2.1) and the surface mineralogy with a resolution of 90m. The gravity measurements also revealed the mean crustal thickness, between 27 and 43 km, and the surface density between 1 200 and 1 600 kg/m³ [17]. This very low bulk density implies high water content [18].

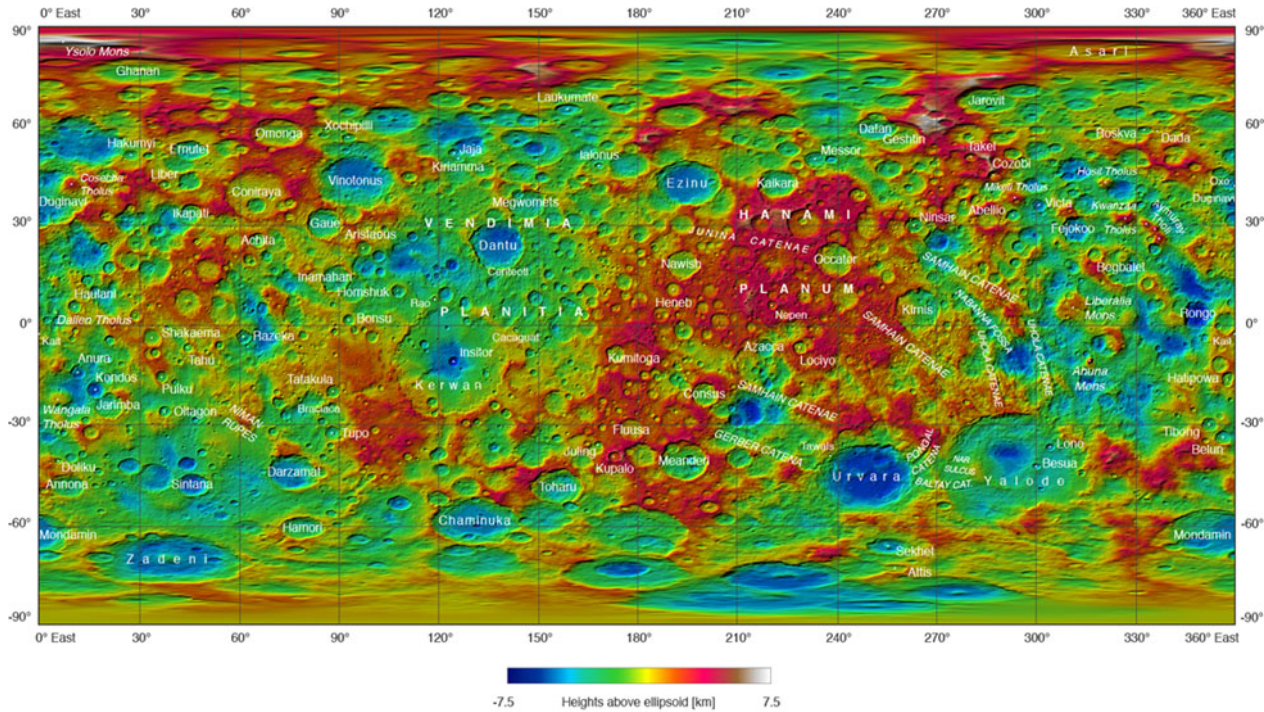


Figure 2.1: Topographic Ceres Map obtain from the Dawn mission, Credit: NASA / JPL-Caltech / UCLA / MPS / DLR / IDA

2.2.1 Composition of the cerean surface

2.2.1.1 Ceres' average composition

The average reflectance spectrum of Ceres acquired by VIR onboard Dawn is presented on Figure 2.2. This spectrum is the result of the large dataset produced during the mission. It confirmed that Ceres is a dark object with an average albedo of 0.09 [19]. The spectrum is characterized by a steep positive slope between 0.3 and 0.5 μm and then by an almost neutral slope up to 2.6 μm . However, this part of the spectra still shows a very wide signature centered at 1.2 μm interpreted as magnetite. The presence of this mineral may be a part of the explanation for the very low albedo of Ceres.

Beyond 2.6 μm , the spectrum become more complex showing several signatures within a large composite band extending to 4.2 μm . Hence, the 2.72 - 2.73 μm band is typical of OH-bearing silicates that are supposed to be Mg-serpentine, Mg-smectite or other phyllosilicates [5]. Moreover, the band at 3.06 μm can be interpreted as a signature of NH₄-phyllosilicates but the lack of experimental spectra on this species prevent from fully constraining the observation. And last but not least, the succession of bands from 3.4 up to 4.1 μm can be interpreted as carbonates. Also, as the band center changes according to the cation in the carbonate, it was possible to conclude that predominant carbonates on cerean surface are dolomite or magnesite. Nevertheless, Na-carbonate has also been observed in high concentration in various sites such as Occator crater (as described in the next part).

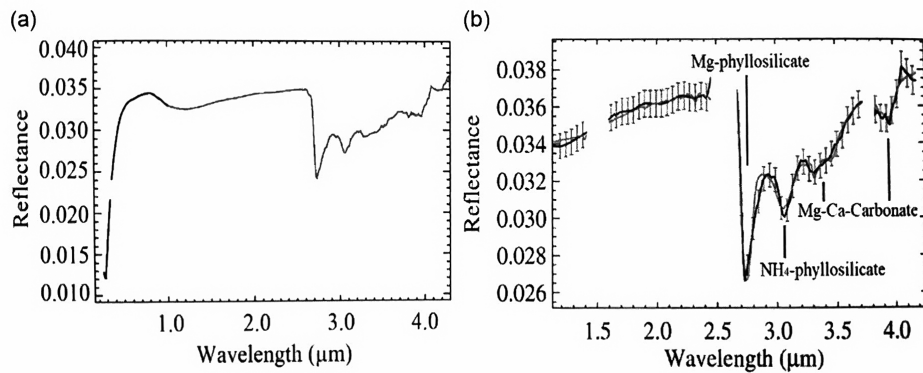


Figure 2.2: a) Measured average spectrum of Ceres from visible and IR channels of VIR. b) Average spectrum of Ceres in the IR channel with error bars of calibration uncertainties and best fit (grey) as modeled including Mg-phyllosilicates, NH₄-phyllosilicates and Mg-Ca carbonate. Figure from [4].

Finally, apart from these mineral phases, a few localized exposures of water ice have been detected, in craters or shadowed sites. Hence, although the mean surface mineralogy of Ceres is complex, it is clear that the identified species indicate a strong global aqueous alteration relating the important role of water in the geochemical evolution of cerean surface.

2.2.1.2 Location with specific mineralogies

VIR spectral imaging capabilities and in particular its high spacial resolution power allow for the first time to link geochemistry with surface geology. Hence, it make it possible to build mineralogical maps of all cerean surface. So was the carbonate distribution analysed by correlating with surface geomorphologies. It was shown that the highest-albedo area, located in Occator crater and visible on Figure 2.5 are associated with changes in their spectral parameters comparing to the surrounding regions. It indicates a higher concentration in Na-carbonate, ammonium salts and Na-phyllosilicates, hence being maybe related to recent hydrothermalism or cryovolcanic activity (see part 2.2.3).

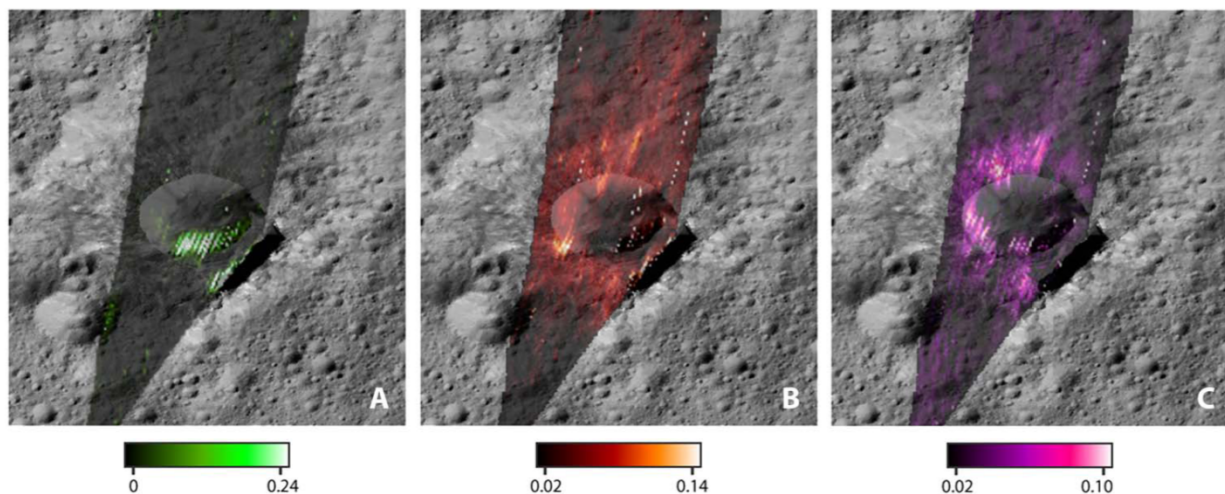


Figure 2.3: Distribution of surface compounds in Oxo crater. a) Water ice, b) sodium carbonates, c) hydrated sodium carbonates. Abundances are derived from spectral fitting methods. The Figure comes from [4].

Besides Occator, other regions also show a specific mineralogy such as Oxo crater, Ikapati crater, Ahuna Mons or Kupalo crater. They exhibit a band which is characteristic of Na-carbonates. But as it is shown on Figure 2.3, the spectra of some small areas cannot be fully fit with Na-carbonates and so indicate the presence of hydrated Na-carbonates such as thermonatrite or hydrohalite. Those minerals being unstable on airless surfaces, it indicated either the presence of water ice as shown on the southern side of Oxo crater Figure 2.3, either a recent/continuous refurbishment of hydrate brines from subsurface reservoirs.

2.2.2 Detection of organic compounds

Another stunning result of Dawn was the detection in 2017 by VIR of an absorption feature at 3.4 micrometers which is characteristic of aliphatic organic matter [20]. The VIR instrument was able to map the locations of this material, as shown for Ernutet in Figure 2.4. These organic materials are mainly located in the northern-hemisphere of Ceres, within a broad region of about 1,000 square kilometers close to the Ernutet crater.

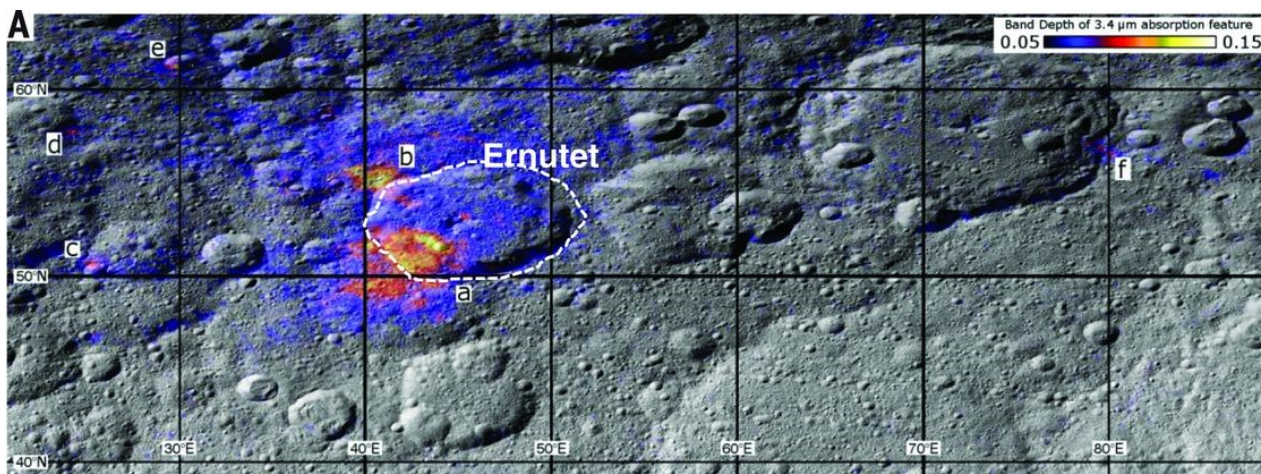


Figure 2.4: Distribution of the $3.4 \mu\text{m}$ band depth at the Ernutet crater region, on Ceres. Figure reproduced from De Sanctis et al. [5]

The strongest signature is observed on the floor and on the south-western rim of the crater in a region containing high concentration of Na-carbonates. To the north of the crater are other smaller well-defined signatures, and some other points with weaker signature of organics are also localized further from the crater in the west and east. Surprisingly, either the organics nor the carbonates can be associated to a specific crater. The signature are very patchy and span the region of Ernutet, spilling into adjacent, older crater. The only other clear signature of organics was found in Inamahari Crater, about 400 kilometers away from Ernutet, also showing no correlation with the morphology. One of the hypothesis to explain the presence of organic compounds, associated with an enrichment in Na-carbonates and phyllosilicates would be to assume an extrusion of cryovolcanic fluids and/or hydrothermalism processes. Such kind of an endogenic mechanism could so explain the non-correlation between impact morphologies and organic compounds detection.

2.2.3 Cryovolcanism and hydrothermalism

In the continuity of the organic matter measurements, the mission allowed the detection of sodium carbonate Na_2CO_3 , measurement performed in the near infrared, [21], in the floors of several craters, such as Occator crater a 92 km diameter crater, as shown in Figure 2.5. These salt deposits, also called *facula*, such as bright spots, are the residues of a water ascent from the depths of Ceres to the surface and subsequently to a sublimation of the water ice, leaving a sodium carbonate residual layer. These same sodium carbonate deposits have been detected on a unique geological structure at Ceres' surface: Ahuna Mons (see Figure 2.6). Ahuna Mons is a dome-formation of approximately 4 km of altitude and 17 km wide, explained by a recent cryovolcanic activity, of approximately 210 ± 30 million years. [12].

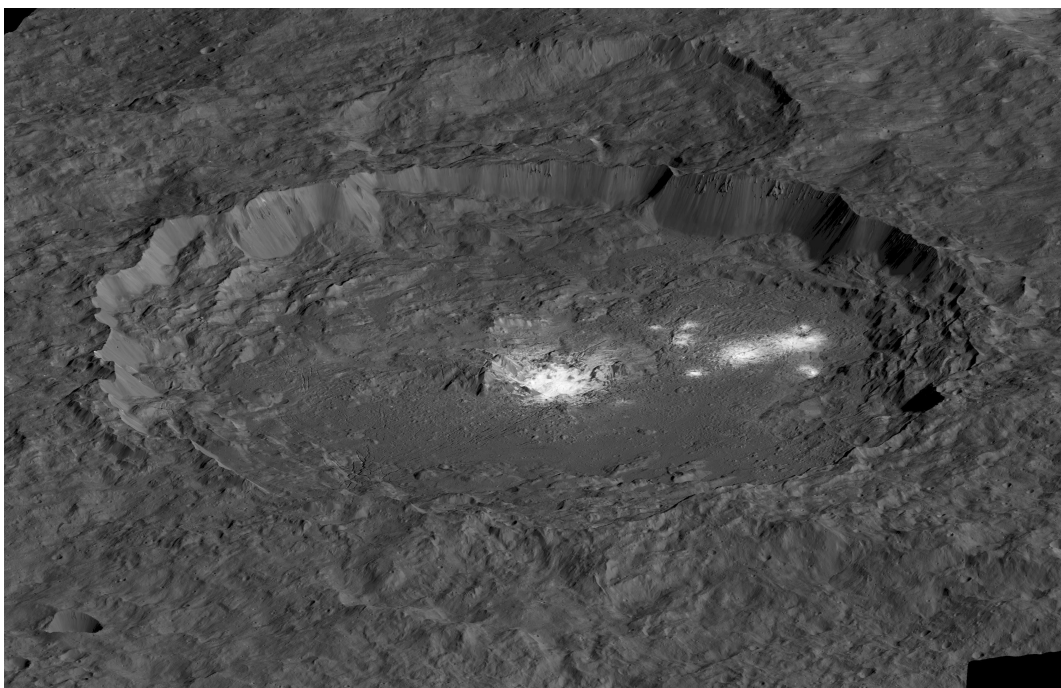


Figure 2.5: Simulated image of bright sodium carbonate deposits at the floor of Occator crater on Ceres ($20^{\circ}N$, $240^{\circ}E$) using images from the Dawn mission, Credit: NASA/JPL-Caltech/UCLA/MPS/DLR/IDA.

Similarly to silicate volcanism on rocky planets like Earth, cryovolcanism forms domes. Cryovolcanism is a phenomenon occurring on icy bodies (moons or bodies of the outer solar system) or on bodies of the main asteroid belt. Intense internal energy, due to tidal effects or internal radioactive energy, forms deep water tables. If an ice "crust" forms around this liquid water table, the water ice acquiring a larger volume than the liquid water, an overpressure occurs in the water table, causing a fracture and thus a rise of the cryomagma onto the surface [22]. Water vapor and water ice is then ejected, leaving deposits of salt and other molecules/elements on Ceres' surface. The structure and the mechanisms governing cryovolcanism are represented, in a simplified and schematic view, in Figure 2.7.

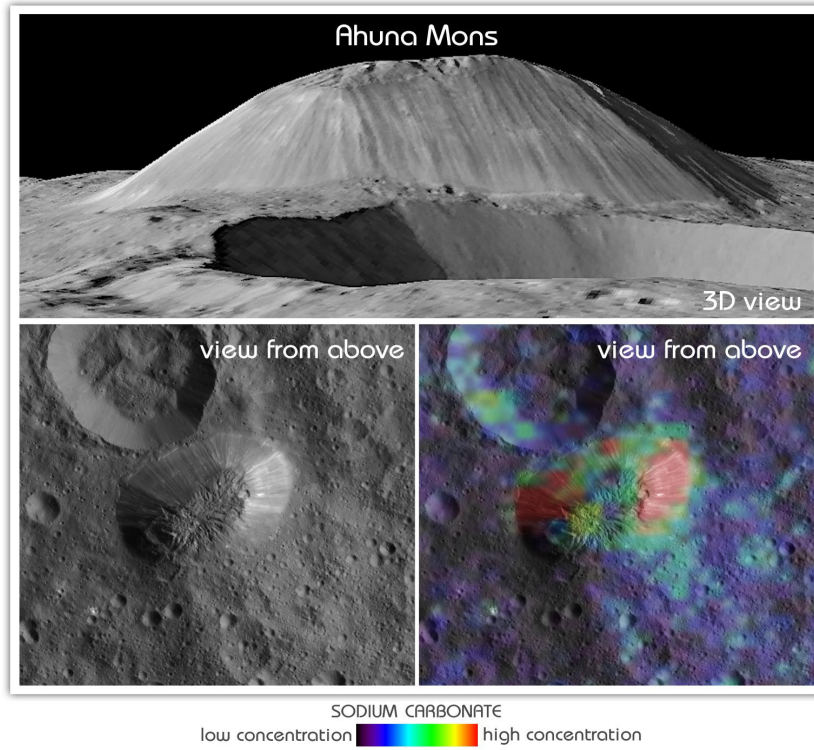


Figure 2.6: Ahuna Mons, a cryovolcanic dome at the surface of Ceres. The top (3D image constructed from topography data) and bottom left images were obtained by the Dawn mission's Framing Camera. The bottom right image represents the sodium carbonate concentration labeled in color, on Ahuna Mons, Credit: NASA/JPL-Caltech/UCLA/MPS/DLR/IDA/ASI/INAF.

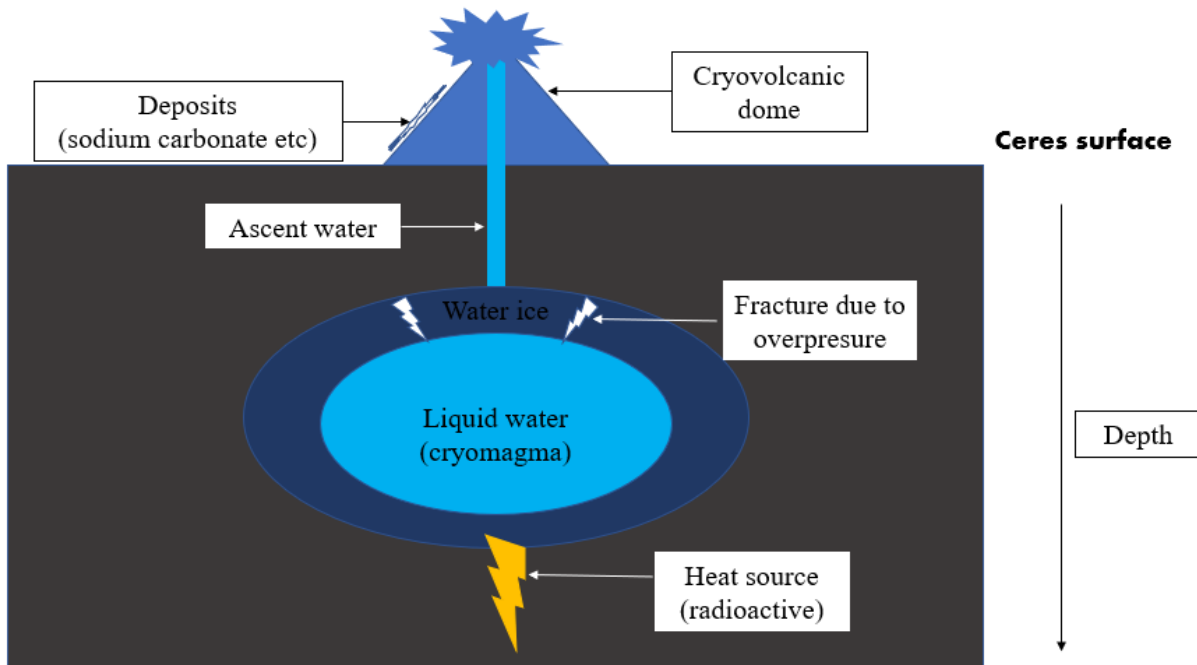


Figure 2.7: Schematic representation of a cryovolcano's structure and the ascent of the cryomagma to the surface. This representation is obviously simplified but allows a general perception of the mechanism.

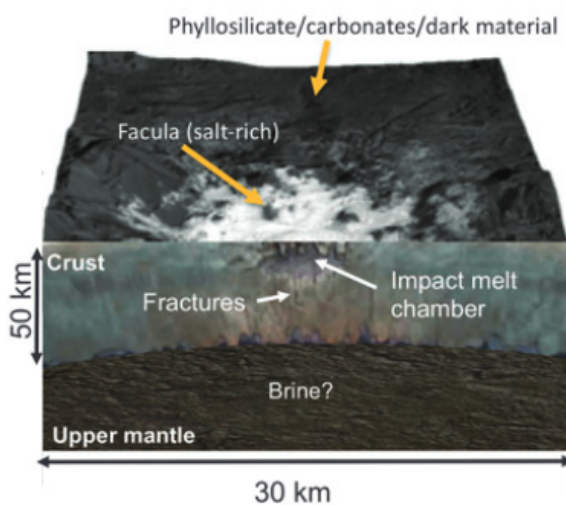


Figure 2.8: Schematic and simplified representation of the Occator crater cross section. Carbonate deposits are shown at the floor of the crater with more or less liquid brine table at depth passing through fractures into the base of the crater[6].

In the case of Occator Crater, the water upwelling and thus the deposition of a layer of sodium carbonate, may be due to fractures in the crater bedrock [23]. Indeed, major impacts, such as the one that led to the formation of the Occator crater, created fractures in the crust favoring a rise of brine present in depth 2.8. These deposits are called faculae, a latin word (plural) meaning "bright spot" in English. The brine is a mixture of water and salt, and an intrinsic property of this brine is mainly a decrease in the glaciation (solidification) temperature, thus allowing salty liquid water to be more stable at low temperatures. The fracturing phenomenon observed in Occator has occurred in many other craters on Ceres' surface, but Occator is still one of the most representative to be observed by NASA's Dawn mission.

2.2.4 Other geomorphological structures on Ceres

Dawn's LAMO observations using Dawn's Framing Camera (FC) at a resolution of 35m/pixel revealed a heavily cratered surface showing complex features that were unexpected. During the primary mission, the science team worked on constructing a global geological map of Ceres according to geomorphological criteria that can be seen Figure 2.9. In the following sections, three main geological features will be discussed: impact craters, slopes processes and what is assumed to be tectonical features.

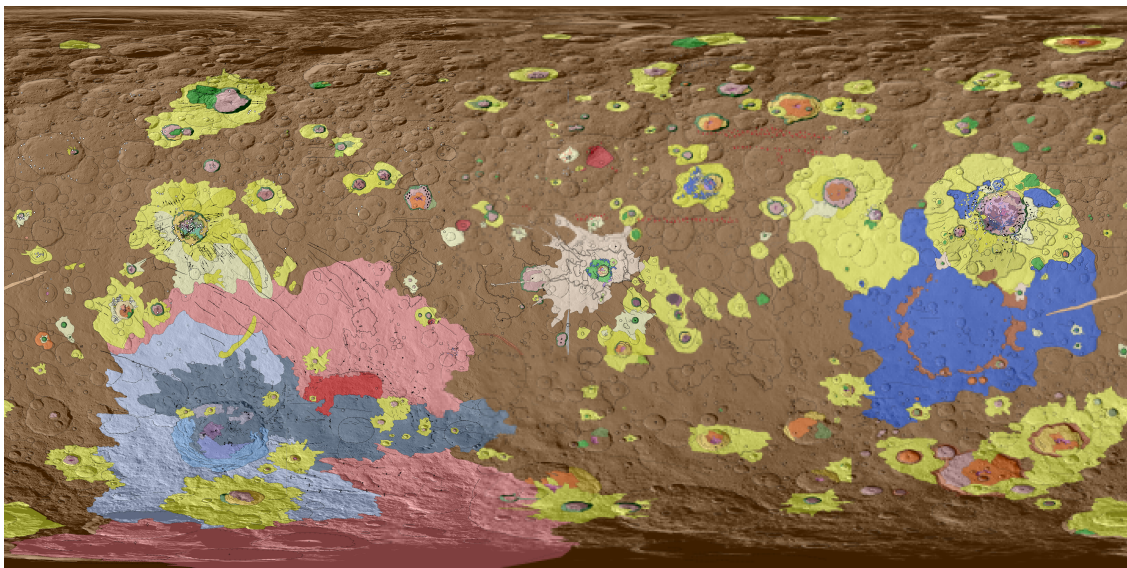


Figure 2.9: Global geologic map of Ceres, produced using LAMO images as a basemap. This map is the unification of 15 quadrangles maps published in a series of papers in Icarus, Volume 316, December 2018, by Andrea Nass and David M. Nelson [7].

2.2.4.1 Impact craters

Unlike other icy satellites where most impact craters have relaxed and disappeared, Ceres shows crater going from 300 km diameter down to the limit of image resolution. Largest basins, of more than 300 km diameter, have not been detected, although some gravity and topography data shows two or three large depressions that could be remnant of ancient basins that have been erased by some resurfacing processes early in Ceres' history, like Vendemia Planitia, a 800 km diameter depression [24].

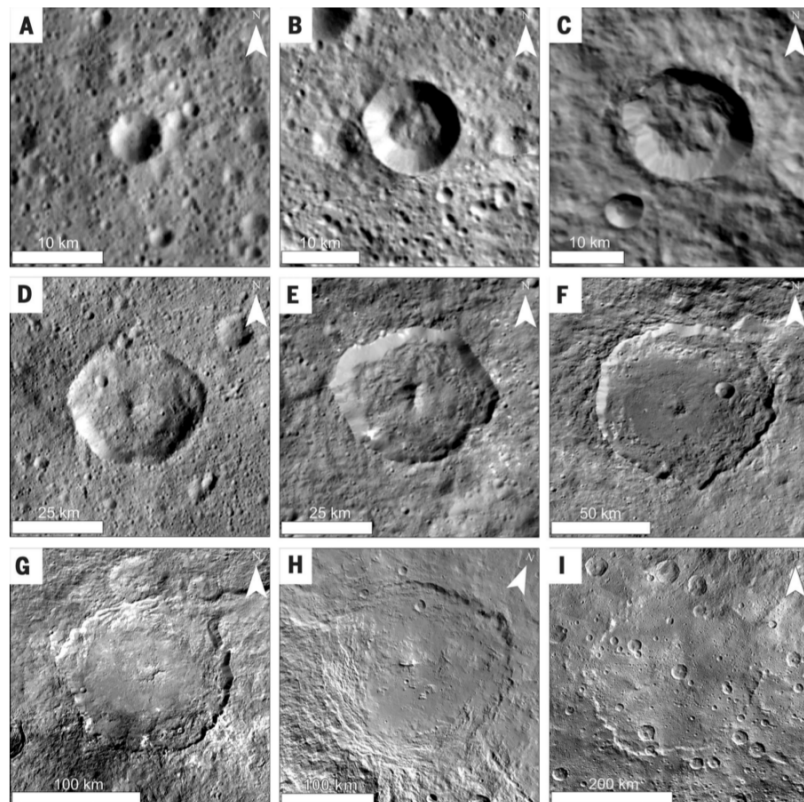


Figure 2.10: Morphologies of impact craters on Ceres. (A) Simple bowl-shaped crater (105°E and 3°N). (B) Modified simple crater (161.7°E and 13°S). (C) Complex crater (279°E and 23°S). (D) Complex crater with central peak (108°E and 10°N). (E) Achita, a polygonal complex crater (65.8°E and 25.8°N). (F) Gaeu crater (84 km, 85.9°E and 30.9°N) showing multiple terraces, a central pit, a smooth and flat floor, and a small peak close to the central pit. (G) Dantu crater (125 km, 137.8°E and 24.4°N), with concentric terraces, a possible peak ring structure or central pit, a smooth and flat floor. (H) Urvara crater (170 km, 248.6°E and 46.3°S), with concentric terraces, a small elongated central peak, a smooth and flat floor, and a relaxed morphology. (I) Kerwan crater (284 km, 123.6°E and 10.9°S) with a partially relaxed morphology. Arrowheads point north. Figure from [8].

The different morphologies of craters observed at cerean surface are similar to those found elsewhere in the solar system. However, due to the composition of Ceres' crust being transitional between ice and rocks, some morphologies are new. For example, a lot of craters displays a floor filled by a smooth materials that has not been observed elsewhere in icy satellites. It is supposed to be melt or slurries derived from altered phyllosilicates, carbonates and salts. Also, craters bigger than 40 km tend to shows pitted floors, fractures and sometimes central pits, indicative of a material weaker than silicate objects like the Moon or Vesta.

Most of the features that can be observed within Ceres' craters are displayed in the examples of Figure 2.10. All crater types are visible except for large multiring basins. Some craters shows evidences of lobates flows such as crater B, crater C or Urvara's flanks as it can be seen Figure 2.10.

Others are polygonal, as Kervan, Dantu or Achita, whose rims are composed of at least two straight segments, and have been identified on other asteroids and icy moons. This type of craters is widespread on Ceres so it suggests that its crust is highly fractured [25].

And some craters are rayed, or flood-fractured in analogy with the lunar class crater. The floor of these craters are cut by radial, concentric and/or polygonal fractures and their formation invoke floor uplift due to cryo-magmatic intrusion beneath the crater or floor shallowing due to viscous relaxation. These craters also exhibits bright bluish ejecta blankets.

Finally, it is clear that the craters scattered on the surface of Ceres are the most common objects but also those at the origin of the greatest diversity of morphologies. Cratering is the most important process that affect cerean resurfacing and impact craters are often related to specific compounds detection, due to their extrusion or exegetic deposition. Understanding the morphologies of craters on Ceres is one of the key point to discover its crust structure and composition.

2.2.4.2 Gradational features

The gradational features relate to those formed by erosion, or aggradation, which is material transport and deposition. On Ceres, these include mass wasting deposits and slope processes. These gradational features are appearing in over 20% of craters larger than 10 km in diameter, and after surveys of Dawn data, more than 170 of these morphologies have been cataloged.

Following their geologic context, their morphology and their physical properties, Ceres landslides were classified in three different archetypal categories [9].

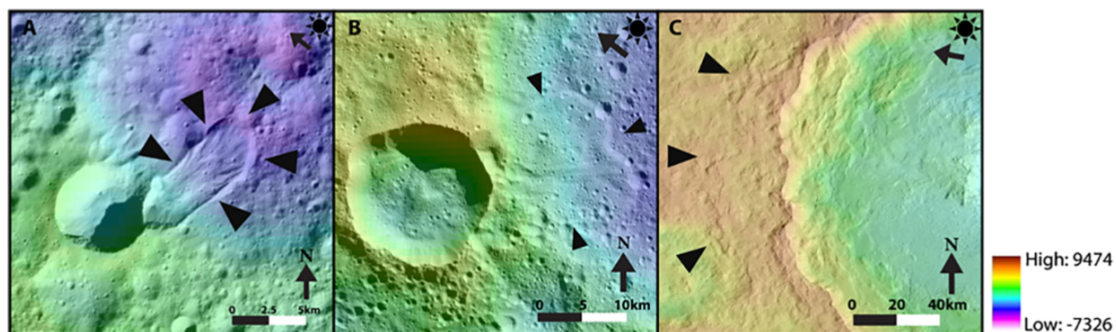


Figure 2.11: Examples of typical landslides of each class. Color indicates topography in meters. Bold triangles indicate the margin of the landslide. a) Type 1 landslide at 50.804° , 27.326° . b) Type 2 landslide at -48.723° , 4.457° . c) Type 3 landslide at 22.061° , -126.711° . Figure from [9].

An example of each of these categories is visible on Figure 2.11. Type 1 flows are thick, tongue shaped, furrowed flows often occurring on steep slopes. It suggests a not negligible water ice content in their composition, which is consistent with their observation mostly above 50° latitude where shallow ice is supposed to be stable. Conversely, type 2 flows are thin and spatulate and have long runouts that are observed on shallow slopes below 50° latitude. It suggest that they are mobilized by melted ice. Both type 1 and 2 landslides occurs on crater rims, flowing into or out of

the host crater and may have been triggered by the impact. Finally, type 3 landslides are cupstate, sheeted flows that appear to be fluidized located middle to low latitude either on the rims or within the ejecta blanket. A good example for those T3 flows is the Haulani crater western side, on Figure 6.8. In contrast to T1 and T2 flows, T3 flows are strongly coupled with the impact timing and are interpreted as fluidized ejecta, also consistent with a crust made of an high water-ice content.

2.2.4.3 Tectonic features

Following the analyses of Dawn images, it has been discovered that Ceres lacks both globally extensive compressional faults or tectonic features. However, some localized tectonic features have been observed such as larger pit chains and the smaller features found in the floor-fractured craters. Two examples for these features are showed on Figure 2.12.

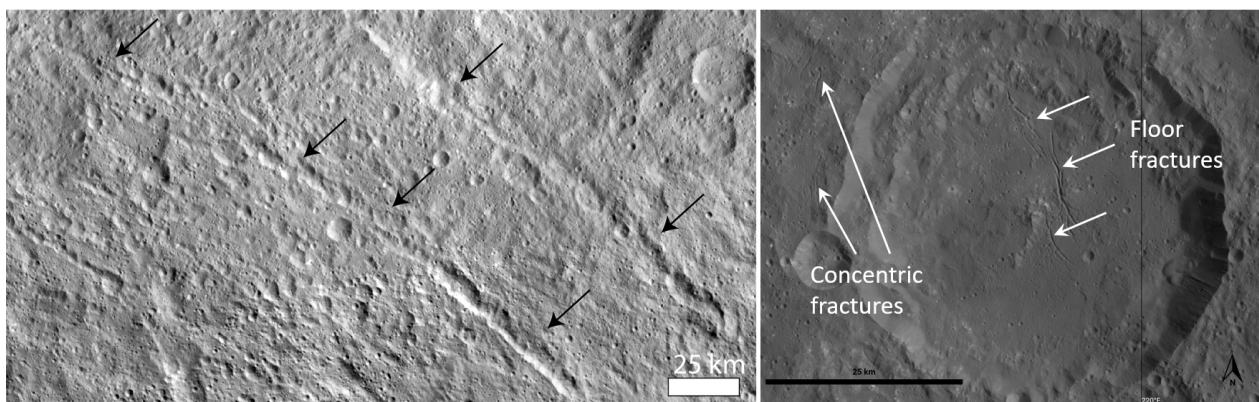


Figure 2.12: Example of tectonic features from Dawn LAMO images. a) The pit chain of Samhain Catenae. b) The floor fractures and the concentric fractures of Azacca crater.

The only well defined pit chain at Ceres surface are Samhain Catenae, as presented 2.12. Being more than 300 km long and up to 11 km wide, this structure clearly have a regional and even a global size. It is morphologically distinct from secondary impact chains associated with big impacts like Urvara or Yalode. Pit chains have more poorly define rims and more irregular shapes than secondary impact chains. Samhain Catenae are supposed to be formed during an extensionnal event, maybe resulting of a regional upwelling material arising from convection/diapirism. Other hypothesis like a basin-forming impact or freezing of a global/regional subsurface ocean are also possibilities [4]. An other feature called Nabanna fossa has the same orientation as Samhain and may also have formed during the same event. Lastly, other much smaller pit chains are observed within Ceres surface but have yet not been studied nor understood.

Others important tectonical structures are the fractures in crater floors. Twenty-one impact craters show such type of irregular grooves and some may sometimes grade into pit chains. This fractures are supposed to be due to crater floor extension probably due to cryomagmatic intrusions below the crater floors or intrusion of low density and low viscosity material into the crater walls via solid state flows. Some craters also show concentric fractures in their surroundings attributed to the presence of a shallow, low viscosity subsurface layer, which is consistent with the observations of pitted terrain and crater floor fractures.

2.2.5 Ceres' internal evolution

2.2.5.1 Internal structure of a water-rich body

From Dawn's observations, densities were inferred by Ermakov et al. [26]. Their analysis shows that Ceres is differentiated into a low-density crust of $1200\text{--}1300 \text{ kg/m}^3$ of 40 km thickness in average, and a rocky mantle of density $2390\text{--}2450 \text{ kg/m}^3$. The low crustal density implies a silicate volume fraction of less than 20%, contains 40% water ice and void space by volume [27], and presence of abundant salts and/or gas hydrates [27]. A study by Lu et al [28], based on the observation of Ceres' topography, determined that the viscosity of the crust decreases with depth. Moreover, with the use of simulation, still with the aim of correlating topography with internal structure, they were able to show that the crust would be composed of carbonate, phyllosilicates and water ice. This crust would be relatively strong with a viscosity of the order of 10^{25} Pa.s . To date, no additional information or data is available. Indeed, it is only based on simulations and therefore provides no more precise internal structure. A study, by using a seismometer on the surface would allow a better understanding of the structure of Ceres. The differentiation of Ceres into these two layers involves a partial melting of its volatile phase [6] early in its evolution while the short-lived radioisotopes provide intense heat.

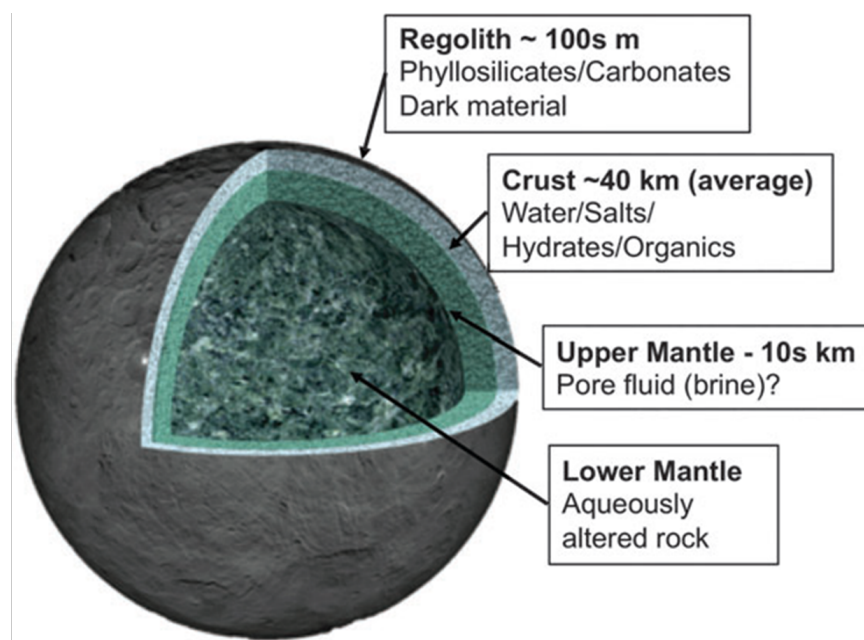


Figure 2.13: Global interior structure for Ceres. [6]

2.2.5.2 Evolution pathways for Ceres

The Dawn mission has demonstrated the eventful history of Ceres, a migration of the dwarf planet from the Neptunian environment to the inner solar system. The ammonia enrichment of hydrated silicates on the surface of Ceres opens the way to more concrete theories about the original location of Ceres[29]. Indeed, the latter presents many differences with the objects of the main asteroid belt. A light atmosphere, of ammonia and water vapor, not retained by the weak gravity of Ceres, is present, which is an unique property of the main asteroid belt. These observations are generally related to icy bodies, typically comets and more generally transneptunian objects.

Scientists hence believe that the dwarf planet Ceres originates from the cold regions of the Solar System, beyond the frost line, in the outer solar system. The frost line is a fictitious, isothermal limit within the solar system. It traces a border beyond which certain molecules condense, between this line and the external solar system. Obviously a shift of the line exists, depending on the species considered. The dwarf planet would have been captured by gravitational resonance by the planet Jupiter, which during his migration in the protoplanetary disk, would have scattered the matter and the massive bodies in the inner disk. This migration would explain today why Ceres is very distinct from its counterparts in the main asteroid belt. Moreover this major event allows and facilitates the study of transneptunian objects because Ceres, at its current orbit, is relatively accessible and makes it one of the most interesting objects of the main asteroid belt.

Chapter 3

Scientific questions and mission objectives

3.1 Ceres: a new first-class target

As reviewed in the precedent part, the unsuspected inspiring results of the Dawn mission have clearly put Ceres in the spotlight [4]. The discovery of cryovolcanism and carbonates deposits, the detection of organic materials on the surface and the supposed presence of a internal ocean, are major interest in the search for extraterrestrial life. Those places could indeed serve as havens where the conditions would be or would have been favourable for the appearance of life.

Thus has Ceres become a first-class target in the same way as Mars or Enceladus for the search of life in the Solar system. As a dwarf planet, largest member of the main asteroid belt, Ceres is the nearest ice-rich body to Earth and is unique in the inner solar system. Its exploration could so provide us insights into properties and processes that may affect icy satellites of the gaseous planets or other large water-rich asteroids.

This renewed interest in this rather easily accessible object (relative to other icy worlds) has not escaped the attention of the various space agencies. In its Decadal Strategy for Planetary Science and Astrobiology [30], NASA revealed that Ceres is now a priority object to visit, as its exploration would provide beginnings of answers to 4 of the 12 priority science questions that were identified in this report. These questions, that the agency will seek to answer over the next decade, are listed bellow:

- Q3. Origin of Earth and inner solar system bodies. How and when did the terrestrial planets, their moons, and the asteroids accrete, and what processes determined their initial properties? To what extent were outer solar system materials incorporated?
- Q5. Solid body interiors and surfaces. How do the interiors of solid bodies evolve, and how is this evolution recorded in a body's physical and chemical properties? How are solid surfaces shaped by subsurface, surface, and external processes?
- Q10. Dynamic habitability. Where in the solar system do potentially habitable environments exist, what processes led to their formation, and how do planetary environments and habitable conditions co-evolve over time?
- Q11. Search for life elsewhere. Is there evidence of past or present life in the solar system beyond Earth and how do we detect it?

3.2 A proper instrument to investigate Ceres characteristics

Although the themes presented by NASA in its report are only guidelines for the future of space exploration, it gives a good idea of what kind of questions the study of Ceres could answer and how the mission should be orientated to tackle those problematics. Thus, only considering Ceres, the scope of the investigation can be narrowed down to 5 main points, some of which were highlighted in the proposal for a Ceres surface sample return mission for the New Frontier program [30]:

1. Characterize the depth and extent of the potential internal ocean of Ceres.
2. Determine if liquid water exists today at shallow depth within the crust and its extend.
3. Investigate the features of Ceres cryovolcanoes and carbonates deposits, their formation and their structure.
4. Determine the nature of salts deposits to determine the chemistry of waters and their potential habitability.
5. Explore the composition, structure and isotopic ratios of Ceres' organics.

As our mission is constrained to a 3U cubesat, we were very limited considering the weight and size of the instrument we would bring to Ceres. It was obviously not possible to find or create an instrument that would be able to answer all of these questions and we had to make a choice. In our decision process, we explored the 3 following avenues regarding the instrument we could build to answer at least one of the scientific questions.

First, the possibility to assess the presence or absence of an internal ocean using a magnetotellurism method was discussed. The idea was to use solar wind as a source of electromagnetic field and to measure its variations after propagating through Ceres [31, 32]. With such kind of instrument, it would have theoretically been possible to estimate the size and the depth of an ocean if it exists. However, the instrument would require the deployment of a big quadrupole antenna. Moreover, this kind of measure have never be tried from orbit. So it was an high risk very innovative mission but probably to difficult to fit in a cubesat. It would have required a lot of investment for development, testing and proving the feasibility of the technique. So as we didn't see any other instrument that could assess the presence of an internal ocean, this topic was left aside.

Then, we sought to select an instrument that would allow us to study the composition of salt and carbonates deposits, and/or the diversity of organic materials. The goal of this instrument would have been to focus on the chemistry happening at the surface of Ceres and to look for indication of life-bricks. As it is impossible to land the cubesat by its own, we had to look for teledetection methods but we rapidly agreed on the fact that it would not be possible to acquire better composition measurements than Dawn ones with a small 3U cubesat. We had so to move to an other idea that was to stay on the back of an other big mission during landing. As soon as the main probe would have landed, we could have jumped a few dozens of meters away to do separate measurements that would have been interesting to compare to the ones of the main mission probe. As this architecture allow us to do some good chemistry at the surface, it relies a lot on the other mission and it would have been hard to develop as long as there is not more details about oncoming mission to Ceres surface.

Last but not least, a more conventional instrument for structural geological exploration of little-known bodies was considered; a radar sounder. As this kind of instrument was not onboard Dawn spacecraft, our knowledge about Ceres subsurface and structural context of the various deposits observed are very limited. Hence putting constrains on the organisations of the different units would be a very important task to understand their evolution. The ability to reveal a few dozens of meters below the surface would also be very interesting to assess the origin, the age and the activity of cryovolcanism. In addition, fitting the dipole antenna of a ground penetrating radar in a 3U seams more feasible although this has never been attempted in such a small spacecraft. This instrument is therefore relatively innovative (in relation to the size of the cubesat) and could produce high value

scientific data. So was it certain that it was the most valuable payload that our cubesat could bring to Ceres.

The instrument being defined, the specific questions that it will allows to answer can now be assessed. What are the objects we want to observe and what is our main scientific question that will guide all the development of the spacecraft and its instrument.

3.3 Main goals of Diploma mission

The choice of the radar as the instrument for our mission to Ceres is highly related to the results of the Dawn mission as it is supposed to bring more constrains on the mechanism, process and chronology of the different main features that were discovered. Indeed, we hope that understanding the processes at the origin of the most striking features of Ceres surface will allow the scientific community to assess the main characteristics and the history of Ceres crust. Hence we can define our main scientific problem for the Diploma mission as following :

What can surface geological processes and resulting morphologies in subsurface tell us about the composition, structure and evolution of Ceres ?

From this very broad question, a lot of sub-questions can be written, especially about the different objects that we will try to highlight with our radar. Indeed, the observations will be focused on four main types of features : supposed cryovolcanic deposits or domes, impact craters, tectonic pit chains or fractures and slope processes. As cryo-features are of definite exobiological interest, craters, fractures and slope processes could give us a lot of information about rheological and lithological properties of Ceres and about the history of its evolution. Hereafter, you can read a short summary of all the types of questions which comes directly from the main problem of the mission:

1. Is there active cryovolcanism on Ceres ? If so, what kind of processes can be observed ? What does it tell us about Ceres crust structure and evolution ?
2. How the different tectonic structures that can be seen from orbit where formed ? Are they related to cryovolcanism, carbonate deposits or impacts ?
3. What are the different morphologies of slope processes (landslides) ? What can they tell us about Ceres crust rheological properties ?

It is therefore in an attempt to provide the best possible answer to these major questions that we have developed the most suitable radar sounder possible despite the size limit of the 3U cubesat.

Chapter 4

Diploma's Radar Sounder (DRS)

DRS will make use of a low frequency radar instrument to penetrate into the subsurface of Ceres. Data from this instrument will support science investigation of Ceres. The following chapter aims at giving a precise description of DRS and its performances.

4.1 DRS in a nutshell

4.1.1 Data acquired by DRS

DRS will profile the subsurface of Ceres and thus acquire fundamental information on surface and subsurface geology by mapping the vertical structures of predefined geological features on Ceres such as cryovolcanoes, landslides, craters, etc. It will thus generate a big amount of data for inferring knowledge on the structure and evolution of Ceres.

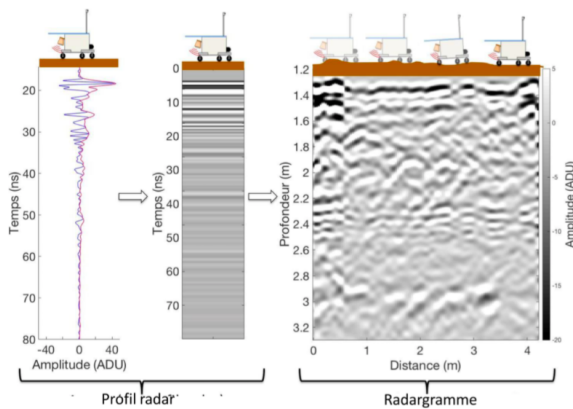


Figure 4.1: Principles of a radar sounder.

DRS is a nadir-looking radar sounder instrument. It transmits low-frequency electromagnetic waves which can penetrate the subsurface (see figure 4.1). When the radar emits an electromagnetic wave, this wave travels through the subsurface. By doing so, it will meet subsurface regions with contrasts of dielectric constants. In these regions, the signal will be reflected back to the radar, where its amplitude through time will be measured. For a given impulsion, the radar will be able to measure different amplitude contrasts, representing different impedance contrasts on the subsurface.

One measurement obtained from one electromagnetic impulsion is referred to as profile radar. Through the trajectory of the radar, this vertical profile can be stacked with other vertical profiles obtained at different locations. These data are then used to create a depth image of the subsurface referred to as radargram. This radargram gives very insightful information for the scientists to geologically study unexposed subsurface features. Figure 4.2 shows an example of a radargram obtained on Mars by the SHallow RADar (SHARAD) on board the Mars Reconnaissance Orbiter (MRO). This radargram reveals ice layered deposits overlying a basal unit.

4.1.2 Heritage

DRS benefits from rich heritage in planetary exploration of the solar system. Orbiting sounder radars have been and will keep being widely used in space exploration. Currently, two radar sounders are orbiting Mars : the SHallow RADar (SHARAD) on board NASA's MRO ([33]) consisting in a high vertical resolution with shallow penetrating depth radar, and the Mars Advanced Radar for Subsurface and Ionosphere Sounding (MARSIS) on board ESA's Mars Express

spacecraft ([34]) consisting in a deep penetration depth radar. Subsurface radar reflections acquired within the caldera of Arsian Mons by SHARAD (cf figure 4.3) has allowed the inference of volcanic past activity on Arsian Mons [10].

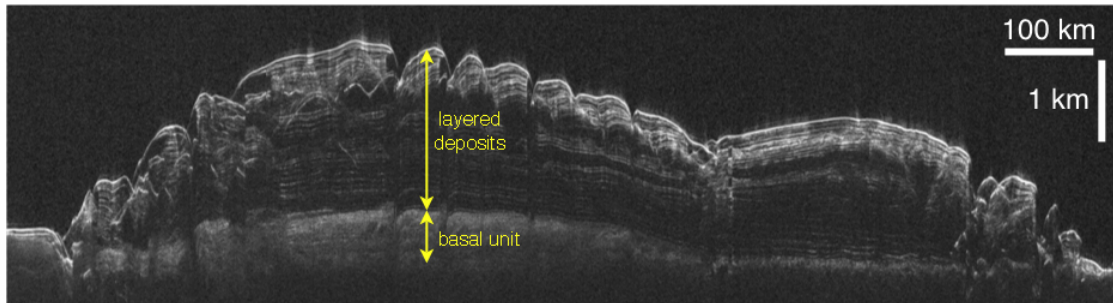


Figure 4.2: Radargram obtained on Mars from SHARAD. Credit : NASA / JPL-Caltech / University of Rome / Southwest research institute / University of Arizona.

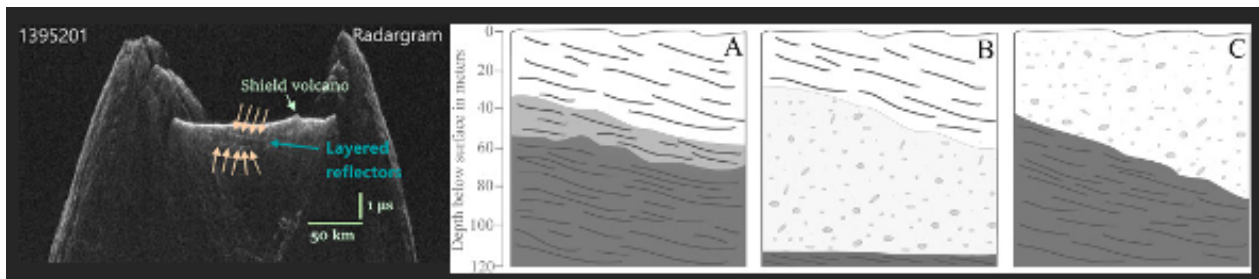


Figure 4.3: (Left) - Radargram of Arsian Mons obtained by SHARAD. (Right) - Schematic representation of the 3 potential scenarios of subsurface stratigraphy interpreted from radargram. A : Scenario 1 - Stacked lava flows with vesiculated and less dense flows overlying very dense lava. B : Scenario 2 - Less dense lava flow and a thick tephra deposit overlying denser bedrock. C : Scenario 3 - Pyroclastic or other low-density material deposited over dense lava flows in the southern part of the caldera, adjacent to the wall [10]

From a more Ceres-like perspective, the Lunar Radar Sounder (LRS) on board the SELENological and ENgineering Explorer (SELENE), Kayuga mission ([35] and [36]) is exploring the subsurface of the Moon. It has allowed for example the detection of intact lava tubes ([37]) or the mapping of the regolith layer thickness of the Moon ([38]). The Radar for Icy Moons Exploration (RIME) on board the JUpiter Icry Moons Exploration (JUICE) ([39] and [40]) aims at exploring the subsurface of Jupiter's icy moons Ganymede, Europa and Callisto. DRS will be mainly based on the heritage of RIME, with the same order of magnitudes for key parameters such as central frequency, chirp bandwidth, duration of pulse (see parts 4.2 and 4.3) etc.

4.2 Description of DRS

4.2.1 Design

Such as every other orbiting sounder radar already used in planetary exploration (SHARAD, MARSIS, LRS, RIME), DRS consists in a dipole antenna. Figure 4.4 shows the design of the dipole antennas. Dipole antennas are a practical way to send a high wavelength (low frequency) signal while being easily deployable in a small area.

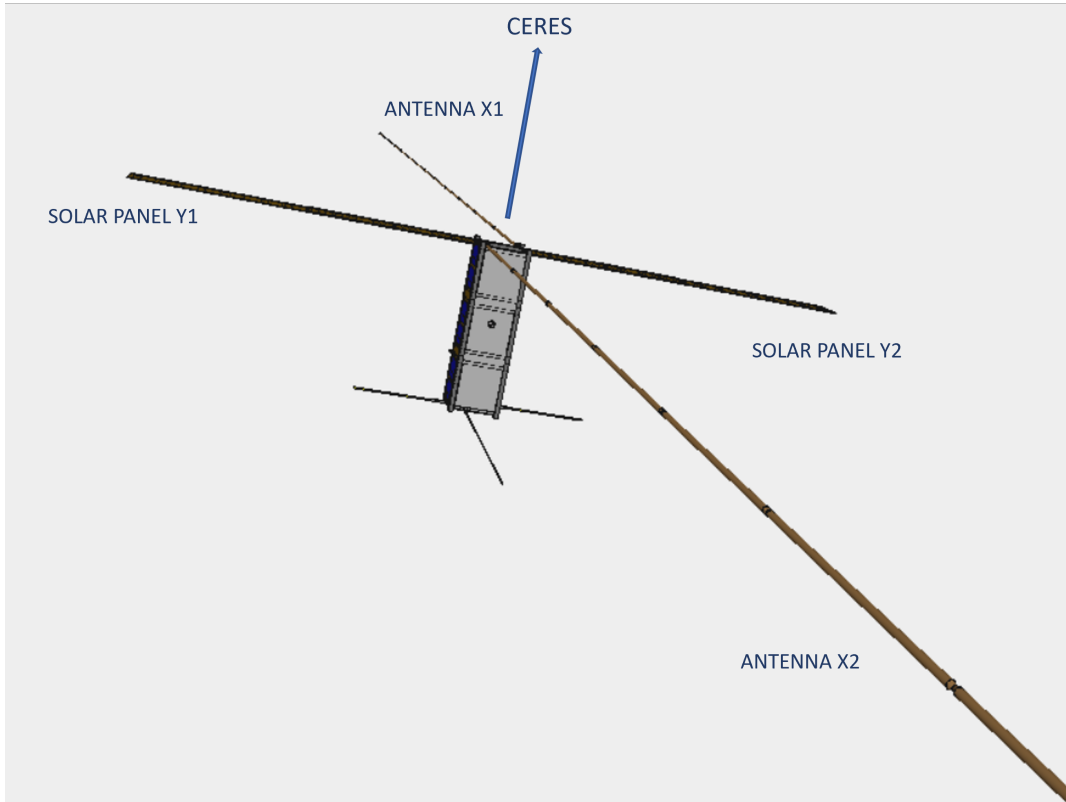


Figure 4.4: View of Diplona's orientation from our IDM-CIC model, the dipole is fully deployed and the DRS is pointing toward Ceres.

4.2.1.1 DRS composition

Diplona will be equipped with a ground-penetrating radar with a frequency range of 10 MHz to 50 MHz. The design of such a radar is quite complex, and it must include the following essential components:

Diplone antenna	The dipole antenna is one of the most important components of the GPR radar, designed to emit pulses to the target CERES
Transmitter	The transmitter produces the electromagnetic signal that the dipole antenna emits into the ground. For a low-frequency GPR radar, the transmitter should be capable of generating low-frequency signals
Receiver	The receiver is responsible for receiving the electromagnetic signals reflected by the subsurface. The receiver must be capable of operating effectively at low frequencies and detecting weak reflected signals
Analog-to-digital (ADC)	The signals received by the receiver must be converted into digital signals to be processed by the signal processing system
Signal processing system	The signal processing system must be capable of processing the received digital signals to extract useful information about the geological structure of the subsurface
Power supply	This part is directly dependent on the cubesat systems

Figure 4.5: This table is presenting all the critical elements of the payload.

4.2.1.2 Antennas design

The design of antennas has been the most critical and important element of the design phase. The length of the antenna determines the range of frequencies that can be used, which can affect the radar's ability to penetrate the ground at different depths. A longer dipole antenna allows for better spatial resolution and deeper penetration into the ground. The length of the dipole is directly related to the frequency of the signal emitted by the antenna. The lower the frequency, the larger the dipole length should be. For sounder radar, the frequencies used are typically in the range of MHz to a few GHz, depending mostly on vertical resolution target.

In the case of Diplona, the objective is to go as deep onto the subsurface as possible while keeping a good vertical resolution (see part 4.3.2.1). It is important to note that the design of a sounder radar to study morphologies on Ceres is a complex process that involves many factors such as the size and shape of the craters, the nature of Ceres' surface, the desired depth of penetration, etc. Therefore, the optimal antenna design must be made considering all these variables in conjunction with the size and weight constraints of the antenna.

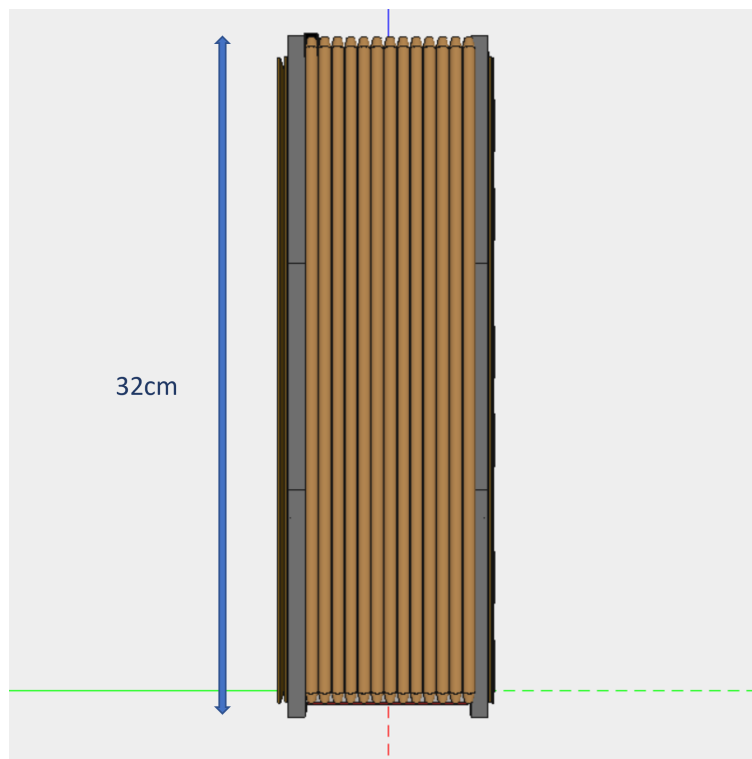


Figure 4.6: Side view of our folded antenna in our IDM-CIC model on the side of the cubesat.

Given the limited space available on a 3U satellite, it was chosen to place the antennas directly on two opposite walls. In order to maximize the space available, the antenna will be folded several times before being released after Diplona is put into orbit, as displayed on figure 4.6. Thanks to an elbow system (see figure 4.8), each branch of the dipole is actually just a single branch folded in on itself twelve times. This has allowed us to obtain an 7.3 m dipole between the two ends with a diameter of 6.5mm. With this antenna length, the operating range of frequencies can go as low as tens of MHz.

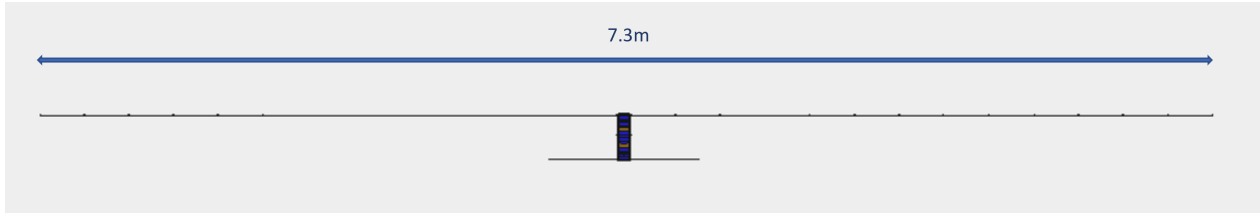


Figure 4.7: Diplona's side view still from our IDM-CIC model where we can observe the dipole's antenna completely deployed, hence measuring 7.3m.

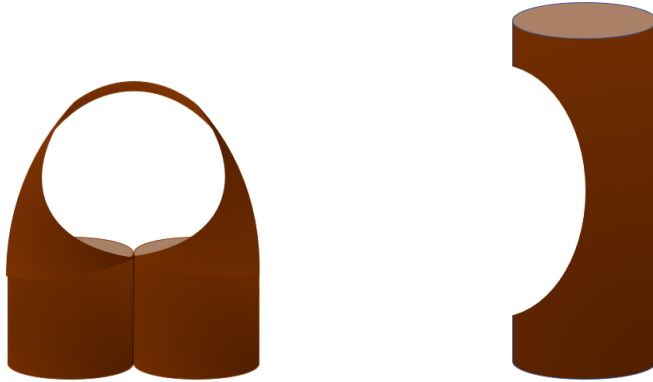


Figure 4.8: Folding system used for the dipole. On the left side, we can see the elbow when the antenna will be folded and on the right side of the image the elbow is deployed. The figure is also coming from our IDM-CIC model.

4.2.1.3 Antenna : Aluminum 7075.

For sounder antennas, the antenna dipoles can be made from various materials depending on the operating frequency and performance requirements. In the frequency range of 10-50 MHz (see part 4.3.2.1), commonly used materials are low dielectric constant dielectric materials, such as polyethylene and ceramics, because sounder radar antennas use electromagnetic waves to penetrate the ground and these materials have the ability to transmit these waves. However, it is also possible to use metals, such as stainless steel or aluminum, for higher frequency ranges, depending on specific application constraints.

The use of an aluminum 7075 alloy (4.1) for a pulsed sounder radar antenna is possible, but it is also important to consider the dielectric properties of the aluminum 7075 alloy to minimize electromagnetic wave losses. However, aluminum 7075 is used in the aerospace industry due to its light weight, high strength, and good resistance to corrosion. It can withstand extreme temperatures and vibrations, making it an ideal choice for space applications. Additionally, aluminum 7075 is relatively easy to machine and weld, allowing for efficient component fabrication for space missions. Of course, the performance of DRS antenna will be tested to ensure it meets the application specifications.

Properties	Aluminum 6061	Aluminum 7075
Density(g/cm ³)	2.7	3.0
Melting Onset (°C)	580	480
Melting Completion (°C)	650	640
Thermal Conductivity (W/m-K)	170	130
Ultimate Tensile Strength (MPa)	310	560
Yield Tensile Strength (Mpa)	270	480
Brinell Hardness	93	150
Elongation at Break (%)	10	7.9
Fatigue Strength (Mpa)	96	160
Shear Strength (Mpa)	210	330

Figure 4.9: Comparison between two commonly used alloys in space applications. The Al6061 is the alloy used for the satellite's structure. The Al7075 will be used for our DRS from ddprototype.com.

Element (%)	Alloy
	7075
Zn	5.10 - 6.10
Mg	2.10 - 2.90
Cu	1.20 - 2.00
Cr	0.18 - 0.28
Fe	0.50 (Max.)
Si	0.40 (Max.)
Mn	0.30 (Max.)
Ti	0.20 (Max.)
Others	0.05 (Max.) each 0.15 (Max.) total
Remainder	Aluminium

Table 4.1: AL7075 Composition from pa-international.com.

4.2.1.4 Energy consumption

The energy consumption and heat dissipation for a dipole radar will depend on many factors, such as the operating frequency, pulse width, operating time, output power, and system design. Generally, pulsed radars consume a significant amount of energy during the pulse emission period and very little energy during the reception period. The amount of energy consumed during the emission period depends on the pulse width and output power of the radar. The amount of energy consumed during the reception period will depend on the sensitivity and reception time of the radar.

We have every interest in minimizing energy consumption due to our low energy storage and recharging capacity (this will be studied in part 5.1.4.4). It is important to design an efficient

radar and use high-quality components to minimize energy losses. It is also important to minimize the radar emission time by using short pulses and limiting the operating frequency.

It is worth noting that for our mission, DRS would consume approximately 0.666 watt-hours for 2 minutes of use at 20 pulses per second with an instantaneous power of 1 W. Note that energy consumption can still vary greatly and this is only an estimate. It is quite possible that we need to increase the number of pulses per second and therefore improve our performance, but this would require the use of more expensive and higher-performance components.

4.2.2 Signal and data

DRS will make use of stretch processing. Stretch processing involves transmission of very long pulse along with processing of the received echo to obtain. With stretch processing, we take advantage of both the increased detection capability of a long-pulse radar system and the range resolution capability of a narrow-pulse system.

4.2.2.1 Principles of stretch processing

To illustrate the principles of stretch processing, let's take the example of the most simple impulsion a radar can emit, without stretch processing :

$$s(t) = \begin{cases} A \sin(2\pi f_0 t), & \text{if } 0 \leq t \leq \tau \\ 0, & \text{else} \end{cases}$$

After a propagation in a distance d with a velocity c , the impulsion reflected back at the radar after emission is a delayed and attenuated copy of the emitted signal, with a delay t_{target} such that $t_{target} = \frac{2d}{c}$. The received signal is $r(t) = K * s(t - t_{target}) + N(t)$ where N is a white Gaussian noise and K is an attenuation factor. To be able to detect the received signal and its associated time of arrival, we use what we call a matched filter. A matched filter allows the optimisation of the SNR when we want to detect a signal whose shape is known in advance, which is the case here. A matched filter consists in computing cross-correlation between a replica of the emitted signal and the received signal :

$$\langle s, r \rangle(t) = \int_{-\infty}^{+\infty} s^*(t')r(t+t')dt' = \int_{-\infty}^{+\infty} s^*(t')(K * s(t+t' - t_{target}) + N(t+t'))dt'$$

The integral $\int_{-\infty}^{+\infty} s^*(t)N(t+t')dt'$ refers to the cross-correlation between the emitted signal and white Gaussian noise. As emitted signal and white Gaussian noise aren't correlated, the result is still a white Gaussian noise. For simplicity here, we will only consider the non-noisy term $\int_{-\infty}^{+\infty} Ks^*(t)s(t+t' - t_{target})dt'$, but the fundamental results with the additional white noise would still hold. Figure 4.10 displays an example of an emitted signal, 2 echoes and their associated cross-correlation. The cross-correlation shows a width of correlation peak of $2*\tau$ seconds. If another echo is located less than τ seconds apart, its cross-correlation with the replica of the emitted signal will be superimposed to the cross-correlation of the first echo with the replica of the emitted signal, such that we won't be able to differentiate between both targets (see figure 4.11).

From this we can induce an expression of the vertical resolution for a simple pulse signal : 2 targets are separable if the distance between them z is such that $z > \frac{\tau}{2} * c$. The vertical resolution for the simple pulse is given by $c * \frac{\tau}{2}$. The logical conclusion is that if we want to have a better resolution we should decrease the duration of the impulsion. As a counterpart, the energy of this signal is $E = K^2 * A^4 * \tau$. Decreasing the duration of the impulsion results in decreasing the energy of the signal, thus in degrading signal to noise ratio. It can have non negligible effects on the detection of a signal.

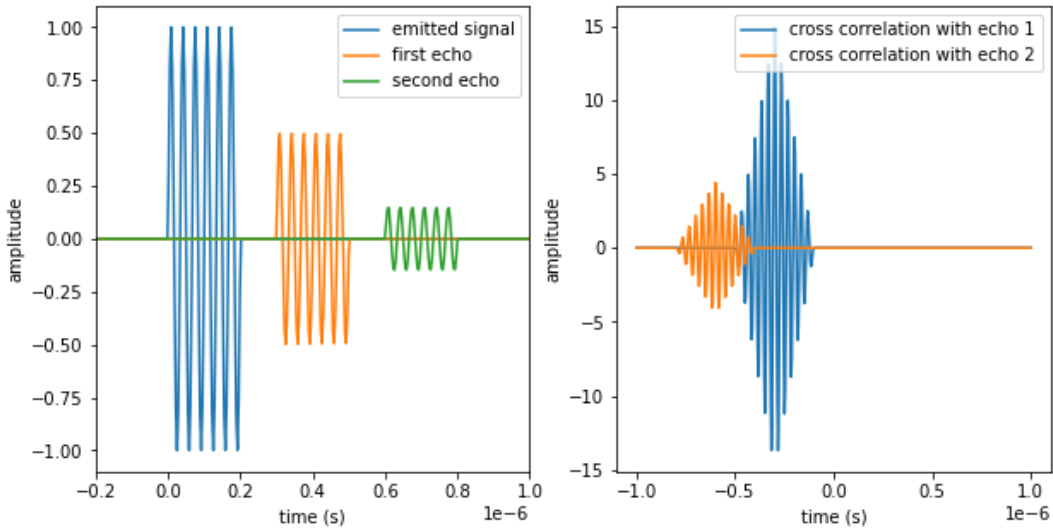


Figure 4.10: Illustration of the cross-correlation between a replica of the emitted signal and 2 far echoes. With the introduced notations, $\tau = 2 * 10^{-7}$ s, $f_0 = 40$ MHz. Distance between both targets is high enough to be able to resolve both targets.

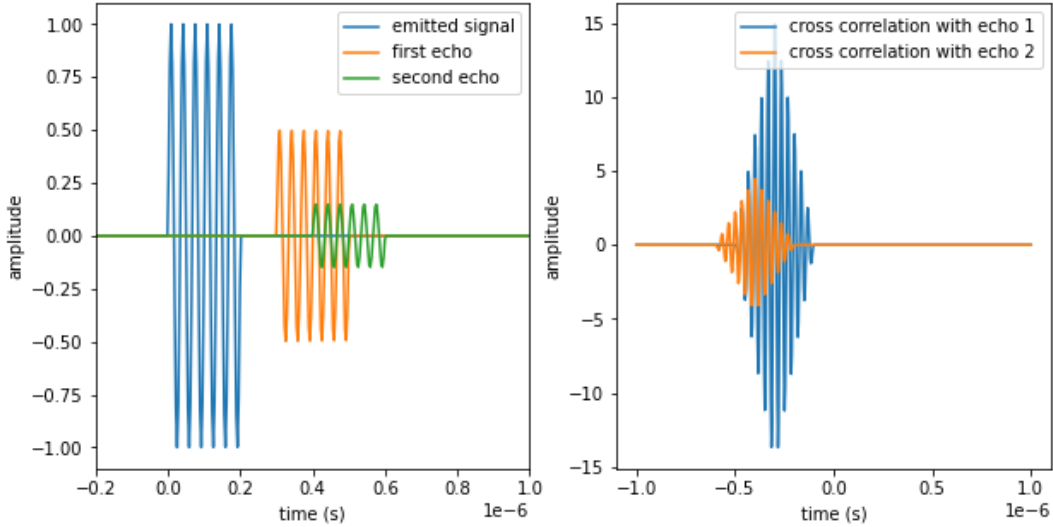


Figure 4.11: Illustration of the cross-correlation between a replica of the emitted signal and 2 close echoes. With the introduced notations, $\tau = 2 * 10^{-7}$ s, $f_0 = 40$ MHz. Distance between both targets isn't high enough to be able to resolve both targets.

To overcome this effect, we might use stretch processing with linear frequency modulation. The basics of linear frequency modulation are presented of figure 4.12. In linear frequency modulation, we make frequency linearly vary during the duration of the impulsion. The frequency can be written as :

$$f(t) = f_{min} + \frac{(f_{max} - f_{min})}{\tau} * t = f_{min} + \frac{\Delta f}{\tau} * t$$

Where Δf is referred to as the frequency bandwidth, or chirp bandwidth. The signal of the emitted pulse is then written as :

$$s(t) = \begin{cases} A \sin \left(2\pi \int_0^t \left(f_{min} + \frac{\Delta f}{\tau} * t' \right) dt' \right) = A \sin \left(2\pi \left(f_{min}t + \frac{\Delta f}{2\tau} t^2 \right) \right), & \text{if } 0 < t < \tau \\ 0, & \text{else} \end{cases}$$

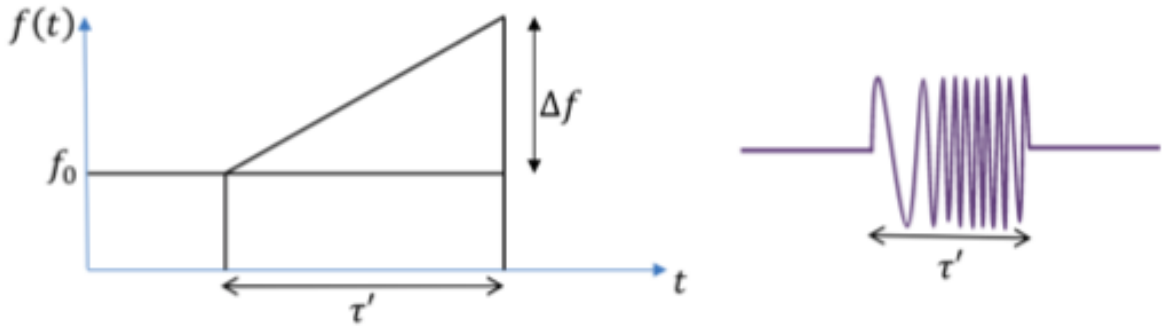


Figure 4.12: Principles of the linear frequency modulation.

On the other hand, the local oscillator generates a reference delayed signal, which can be written as :

$$s_{LO}(t) = \begin{cases} A \sin \left(2\pi \int_{t_{LO}}^t \left(f_{min} + \frac{\Delta f}{\tau} * (t' - t_{LO}) \right) dt' \right) = A \sin \left(2\pi \left(f_{min}(t - t_{LO}) + \frac{\Delta f}{2\tau} (t - t_{LO})^2 \right) \right), & \text{if } t_{LO} < t < t_{LO} + \tau_{LO} \\ 0, & \text{else} \end{cases}$$

This reference delayed signal is generated on a window length τ_{LO} . We will see later that this window length must be constrained. t_{LO} is the start time of the local signal mixing. It is constrained by the altitude of the spacecraft. If the spacecraft is orbiting at an altitude z , the time of arrival of the first echo is $2 * \frac{z}{c}$. t_{LO} is then set to around $2 * \frac{z}{c}$. Figure 4.13(a) displays an example of the emitted signal and the reference delayed signal. Taking the product between $s_{LO}(t)$ and $r(t) = K * s(t - t_{target})$ yields :

$$r(t) * s_{LO}(t) = \begin{cases} K * A^2 \sin(\Phi(t)), & \text{if } t_{target} < t < \tau + t_{target} \\ 0, & \text{else} \end{cases}$$

where

$$\Phi(t) = 2 * \pi * \left(f_{min} * (t_{target} - t_{LO}) + \frac{\Delta f}{\tau} * (t_{target} - t_{LO}) * (t - t_{LO}) - \frac{\Delta f}{2\tau} * (t_{target} - t_{LO})^2 \right)$$

The mixer makes use of a low pass filter to select the low frequency component $\frac{\Delta f}{\tau} * (t_{target} - t_{LO})$. The output of the mixer is the IF signal of frequency $f_{IF} = \frac{\Delta f}{\tau} * (t_{target} - t_{LO})$. This frequency directly depends on the time of arrival t_{target} of the echo. The Fourier transform of the IF signal is a sinus cardinal (sinc) function displaying a peak in the IF with a width of $\frac{1}{\tau}$. Taking the Fourier transform of the IF signal allows the determination of the time arrival with $t_{target} = \frac{f_{IF} * \tau}{\Delta f} + t_{LO}$, where parameters $\tau, \Delta f$ and t_{LO} are all known. The range of the echo reflector can be directly obtained with $R = \frac{v}{2} \frac{f_{IF} \tau}{\Delta f}$. For simulated targets $3 * 10^{-7}$ and $4 * 10^{-7}$ sec apart, we can simulate the IF signals we would obtain, taking $\tau = 2 * 10^{-7}$ s, $\Delta f = 60$ MHz, $f_{min} = 10$ MHz, $t_{LO} = 2.5 * 10^{-7}$ s, $\tau_{LO} = 3 * 10^{-7}$ s. Theoretically, the intermediate frequencies for the first and the second target would respectively be $f_{IF} = \frac{\Delta f}{\tau} * (t_{target} - t_{LO}) = 1.5 * 10^7$ Hz and $4.5 * 10^7$ Hz. Figure 4.13(b) displays an example of the IF signals generated for two echoes. Figure 4.13(c) shows the FFT of the simulated IF signal. The FFT displays two peaks at $1.5 * 10^7$ Hz and $4.5 * 10^7$ Hz, corresponding indeed to the intermediate frequencies. With stretch processing, we can show that vertical resolution is $\Delta R = \frac{v}{2 * \Delta f}$ where v is the velocity of the electromagnetic wave in the media. Indeed, if we consider two targets respectively located at distances R_1 and R_2 , the separation between the two associated peak frequencies f_{IF1} and f_{IF2} in the spectrum is :

$$f_{IF2} - f_{IF1} = \frac{\Delta f}{\tau} * ((t_{target2} - t_{LO}) - (t_{target1} - t_{LO})) = \frac{\Delta f}{\tau} * \left(\frac{2 * R_2}{v} - \frac{2 * R_1}{v} \right) = \frac{2 \Delta f}{v \tau} * \Delta R$$

with $\Delta R = R_2 - R_1$. Theoretically, the minimum frequency separation for two targets to be resolved is the width of the sinc function in the spectrum of the IF signal, which is $\frac{1}{\tau}$. Hence two targets are resolved if $f_{IF2} - f_{IF1} = \frac{2 \Delta f}{v \tau} * \Delta R > \frac{1}{\tau}$, which occurs when $\Delta R > \frac{1}{\tau} * \frac{v \tau}{2 * \Delta f} = \frac{v}{2 * \Delta f}$. We saw on part 4.2.2.1 that vertical resolution for a simple pulse is $\Delta R = \frac{v * \tau}{2}$. The vertical resolution for a stretch processed pulse $\frac{v}{2 * \Delta f}$ is smaller than the vertical resolution for a simple pulse $\frac{v * \tau}{2}$ if $\frac{1}{\Delta f} < \tau$ i.e. $\Delta f * \tau > 1$. For a frequency band large enough, the product $\Delta f * \tau$ will be way above 1, leading to a substantial improvement of the vertical resolution. We also see that increasing the width pulse doesn't change the value of vertical resolution obtained with stretch processing. We are hence able to send a high energy signal by sending a long pulse. Another advantage of sending a long pulse is that it produces a low frequency signal : $f_{IF} = \frac{\Delta f}{\tau} * (t_{target} - t_{LO})$. Decreasing frequency will decrease sampling frequency, relaxing requirements on the Analog to Digital (A/D) converter. This is particularly important when we are using a large frequency band such as the one used by DRS.

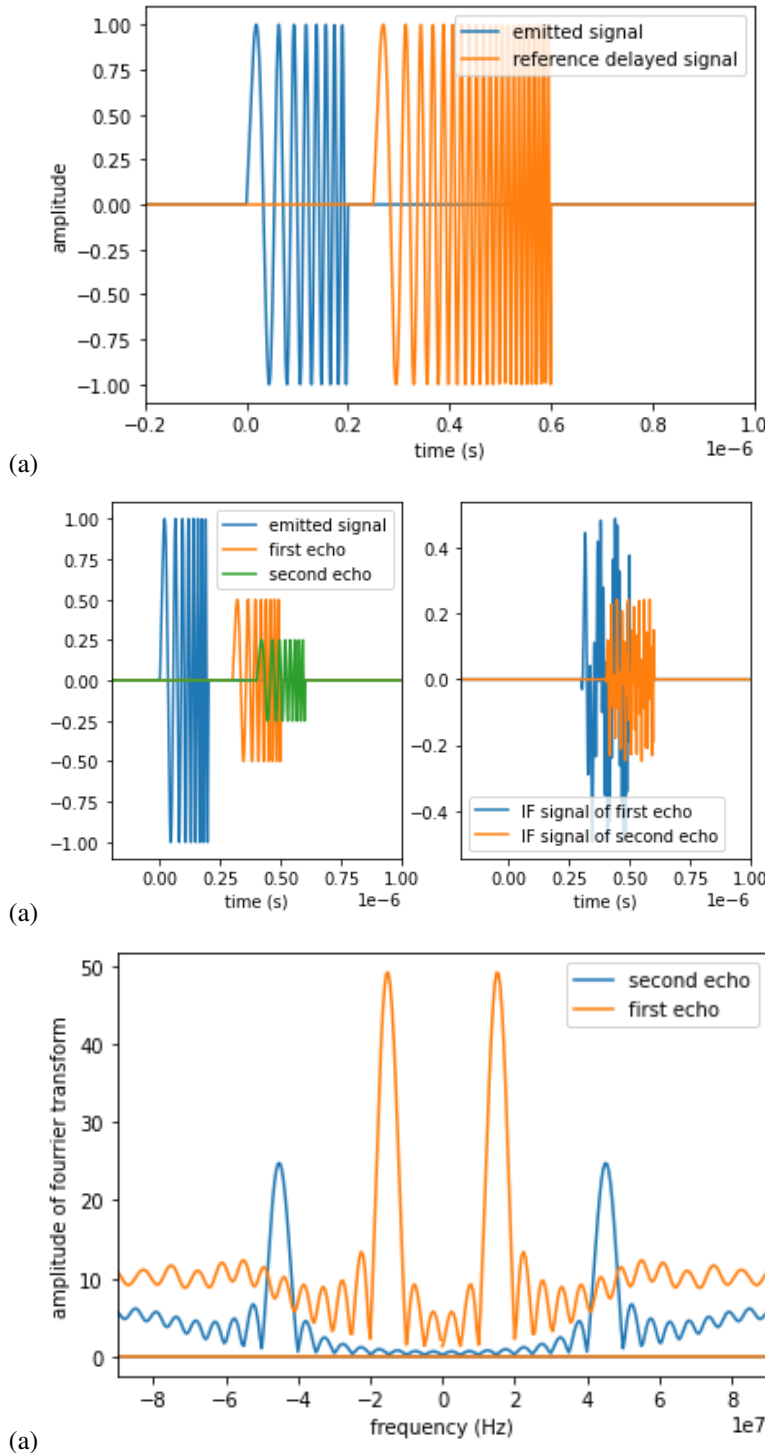


Figure 4.13: (a) Illustration of the emitted signal and the reference delayed signal. (b) Illustration of the IF signal generated for 2 close echoes. We see that the signals associated to the echoes are superimposed, which would lead to no targets resolution in the case of non linearly modulated frequency pulses. (c) FFT of the IF signals for 2 echoes 1×10^{-7} s apart. The peaks of the FFT happen for each target at a frequency called intermediate frequency and thus allow us to retrieve the time of arrival of the corresponding echoes. Even if echoes are close, we are able to resolve them. $\tau = 2 \times 10^{-7}$ s, $\Delta f = 60$ MHz, $f_{min} = 10$ MHz, $t_{LO} = 2.5 \times 10^{-7}$ s, $\tau_{LO} = 3 \times 10^{-7}$ s.

4.2.2.2 Parameters of stretch processing for DRS

Figure 4.14 displays a block diagram of stretch processing. As explained earlier, signals received by the radar are sent to the mixer together with a reference delayed signal generated by the Local Oscillator (LO). The output lowpass filtered IF signal displays different peaks in different frequencies called IF (f_{IF}), which directly depend on the arrival time of echoes (see part 4.2.2.1). The IF signal is then sampled with a certain sampling frequency, dependant on the maximum expected IF frequency. Sampled data can then be digitally processed, with sidelobe weighting and FFT.

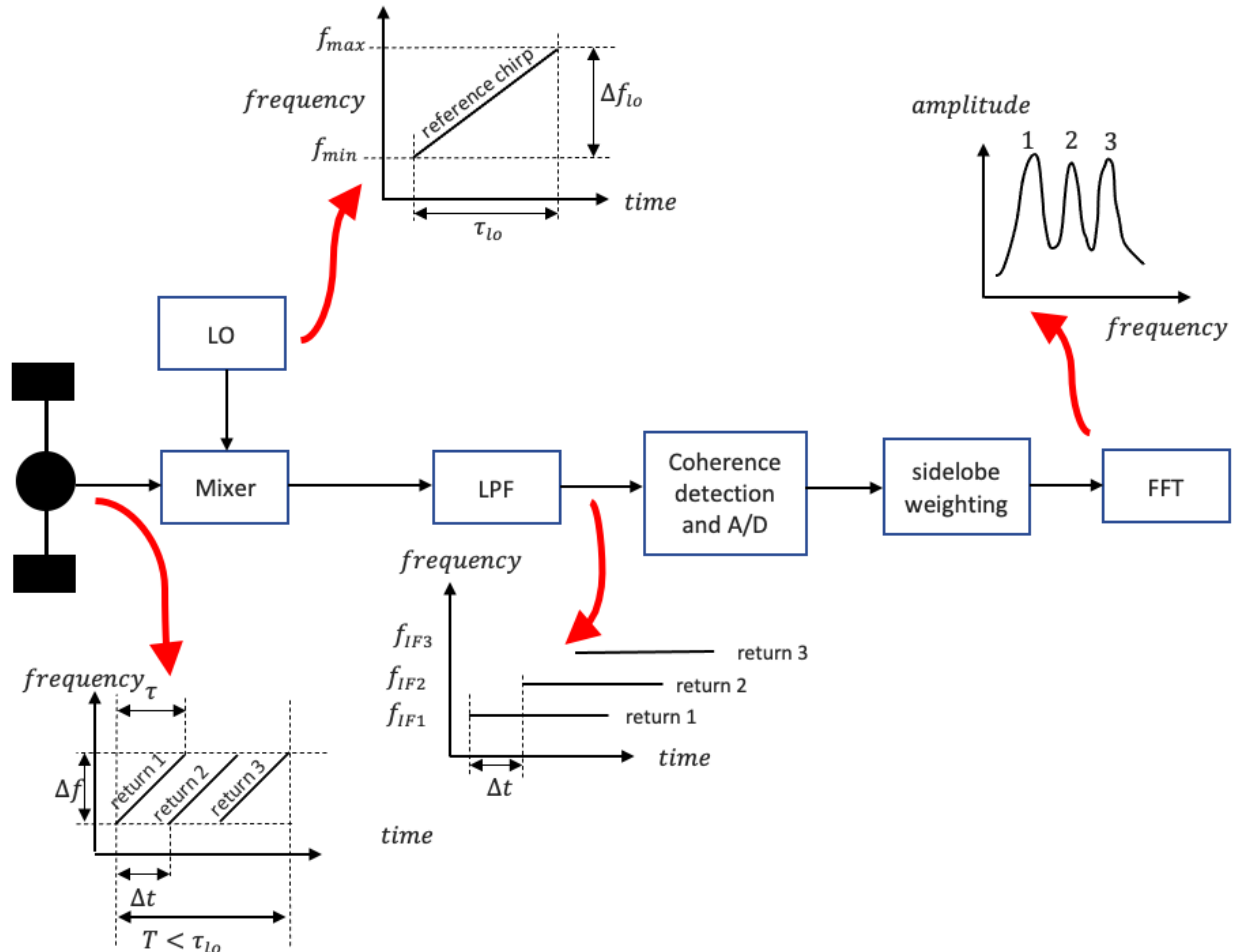


Figure 4.14: Stretch processing block diagram.

Pulse width of emitted signal (τ)	$150 \mu\text{s}$
Pulse width of reference delayed signal (τ_{LO})	$189 \mu\text{s}$
Start time of local signal mixing (t_{LO})	$186 \mu\text{s}$
Frequency band (Δf)	40 MHz
Minimum frequency (f_{min})	10 MHz
Sampling frequency of A/D converter	50 MHz
Pulse Repetition Frequency (PRF)	20 Hz

Table 4.2: Parameters used for stretch processing on DRS.

Table 4.2 shows the values adopted for the parameters used for the stretch processing on DRS. The pulse width has been taken to be a large value, accounting for the orbiting altitude of the

nanosatellite. As the nanosatellite will orbit at 28 km, τ must not exceed $\frac{2*28000}{c} \approx 186 \mu s$ to avoid the possibility of a blind zone under the surface of Ceres. Start time of the local signal mixing t_{LO} is estimated so that first echo arrival is included in the window of reference delayed signal of width τ_{LO} . Indeed, having a part of the echo not included in the window of reference delayed signal leads in degradation of SNR, highlighting the importance of defining well these parameters. Figure 4.15 displays a timing chart of the radar. Note that the starting time of local signal mixing may change depending on the altitude of the satellite (see part 4.3.1).

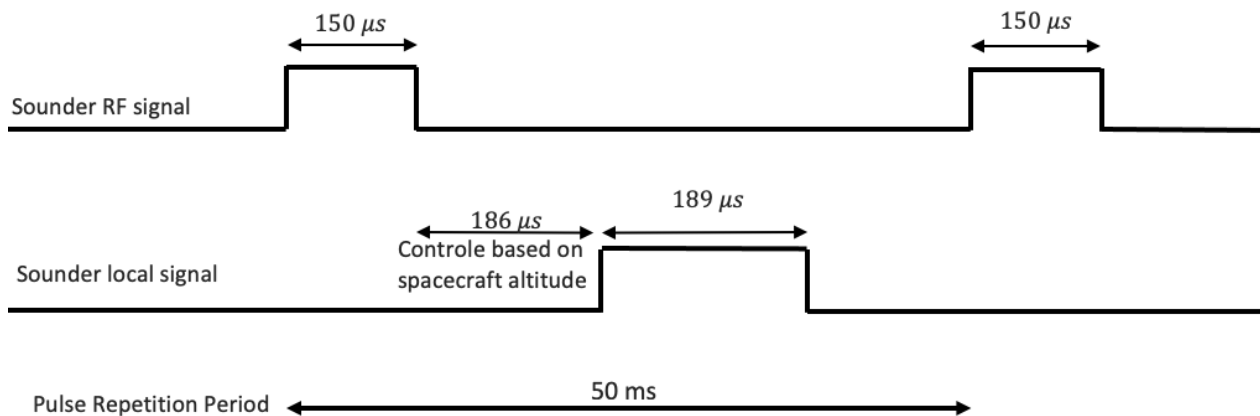


Figure 4.15: Timing chart of DRS. RF pulse width is set to 150 μs . The local signal is generated 186 μs after the RF pulse. This value may change accordingly to the altitude of the spacecraft. The local signal width if set to 189 μs , accounting for the maximum penetrating depth of DRS. This configuration is considered as the baseline configuration for DRS i.e. the configuration when there is no topography but may be slightly different depending on the altitude of the spacecraft.

In table 4.2, values of the frequency band and the minimal frequency have mostly been defined for performance purposes (cf part 4.3.2.1). Figure 4.16 shows an example of the spectrum of the IF signals obtained considering three targets. The first two targets are located 5 m apart, which is close to the vertical resolution (2.1 m) given our frequency band (see part 4.3.2.1). The second and third target are 10 m apart. We see that echoes are well resolved and that we are able to reconstruct their position.

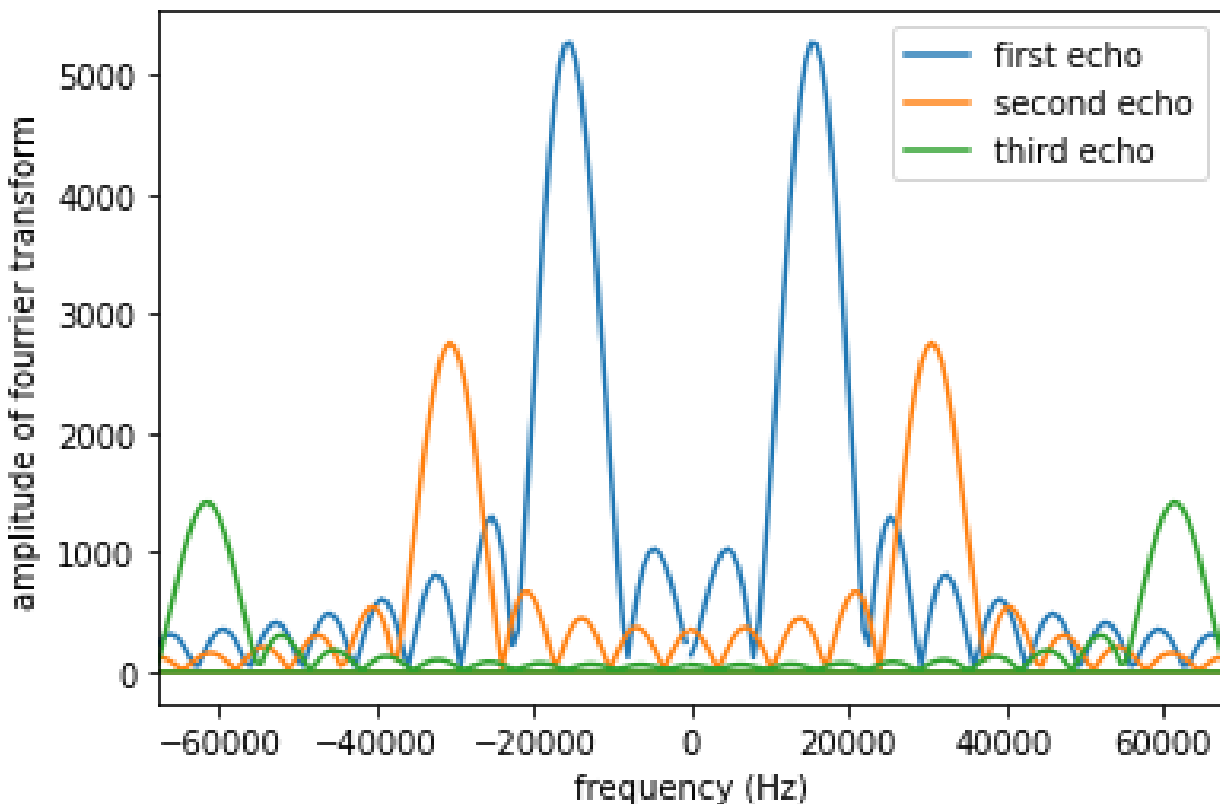


Figure 4.16: Simulation of 3 echoes. FFT of the simulated IF signals. $\tau = 150 \mu\text{s}$, $\Delta f = 40 \text{ MHz}$, $f_{min} = 10 \text{ MHz}$, $t_{LO} = 186 \mu\text{s}$, $\tau_{LO} = 189 \mu\text{s}$. Peaks in the Fourier domain happen for each target at a frequency called Intermediate Frequency.

4.3 Performances of DRS

4.3.1 Impact of topography on stretch processing parameters

The value of t_{LO} can be decreased depending on topography of the terrain along with uncertainties related to the orbit of the nanosatellite. If the nanosatellite flies over a high elevated terrain, topography will have a consequence of the absolute altitude of the nanosatellite, leading to the necessity to decrease the value of t_{LO} to account for echoes that could be returned before $186 \mu\text{s}$. As a consequence, the value of the IF frequency $f_{IF} = \frac{\Delta f}{\tau} * (t_{target} - t_{LO})$ may change. The highest elevation terrain DRS will fly over is Ahuna Mons (see part 2.6), with a maximum elevation of about 3550 m. As a consequence, the altitude of the satellite is 24550 m, hence a first return time of $\frac{2*24550}{c} = 163 \mu\text{s}$. t_{LO} must then be set to around $163 \mu\text{s}$. On the other hand, Urava crater is the target with the lowest elevation (see part 6.2.4). It has a minimum elevation of -6500 m, increasing the altitude of the spacecraft to up to 34500 m. The first return time if then $232 \mu\text{s}$. More precisely, elevation of Ahuna Mons is between -500 and 3550 m (see figure 6.6). To account for this variation, local signal mixing should start at around $t_{LO} = 163 \mu\text{s}$. The last return time possible is given by $t_{target_{max}} = 163 + 2 * \frac{3550 - (-500) + \sqrt{\epsilon'} * 150}{c} \approx 192 \mu\text{s}$. To account for this difference in elevation, local signal width should be set to at least $\tau + 2 * \frac{3550 - (-500) + \sqrt{\epsilon'} * 150}{c} \approx 179 \mu\text{s}$. As a consequence, the maximum theoretical IF obtained on Ahuna Mons is $f_{IF_{max}} = \frac{\Delta f}{\tau} * (t_{target_{max}} - t_{LO}) \approx 7.74 \text{ MHz}$.

These calculations can be made using available knowledge of topography of principal targets defined on part 6.2. Table 4.3 shows the impact of each main target defined in the mission given their topography. The topography of each target calls for a redefinition of the starting time of local signal mixing along with pulse width of local signal. In practice, parameters of stretch processing will be adjusted depending on the location of the satellite, in order to optimise processing of the emitted pulse. We see on table 4.3 that the maximum expected IF frequency of the IF signal for the whole mission will be around 10 MHz. This is way below the maximum frequency of the emitted pulse, which is 70 MHz. This allows the relaxation on constraints of the A/D converter, as a lower maximum frequency implies a lower sampling frequency. Sampling frequency of A/D converter is set to 50 MHz, which is five times above maximum expected Intermediate Frequency (10.4 MHz according to table 4.3). Note that this maximum expected Intermediate Frequency only happens at the lowest elevation of the target, when the difference $t_{target} - t_{LO}$ is the largest possible. In less elevated parts of the targets, the difference $t_{target} - t_{LO}$ is lower, making the Intermediate Frequency lower.

	Occator Crater	Ahuna Mons	Haulani Crater	Uravana Crater
Expected time of first echo arrival (μs)	157	163	181	211
Expected time of last echo arrival (μs)	196	193	210	233
Minimum necessary pulse width of reference delayed signal (μs)	189	180	179	172
Excepted maximum Intermediate Frequency (MHz)	10.4	8	7.7	5.9

Table 4.3: Impacts of topography of the 4 main targets.

This is illustrated on figure 4.17 which displays an image of the four main targets of our mission (see part 6.2 for more details). The knowledge of their topography, obtained from the mission Dawn, allows the study of the maximum expected Intermediate Frequency of the stretch processed signal, given parameters of stretch processing chosen (see part 4.2.2.2). This is illustrated on figure 4.18. For Occator crater, we are most of the time at an altitude such that the IF of the signal is around 8 MHz or between 2 and 5 MHz. The maximum frequency of 10.4 MHz is almost never reached. For Ahuna Mons, the repartition of expected maximum IF displays three peaks, amongst which the two biggest are on low frequencies ($\approx 0\text{-}1$ MHz and $\approx 4\text{-}5$ MHz). AS for Uravar and Haulani craters, the repartition of maximum expected IF is globally close to the maximum possible value (around 7 MHz for Haulani crater and 4.5 MHz for Occator crater). All these results make reasonable the choice of a sampling frequency of the signal of 50 MHz.

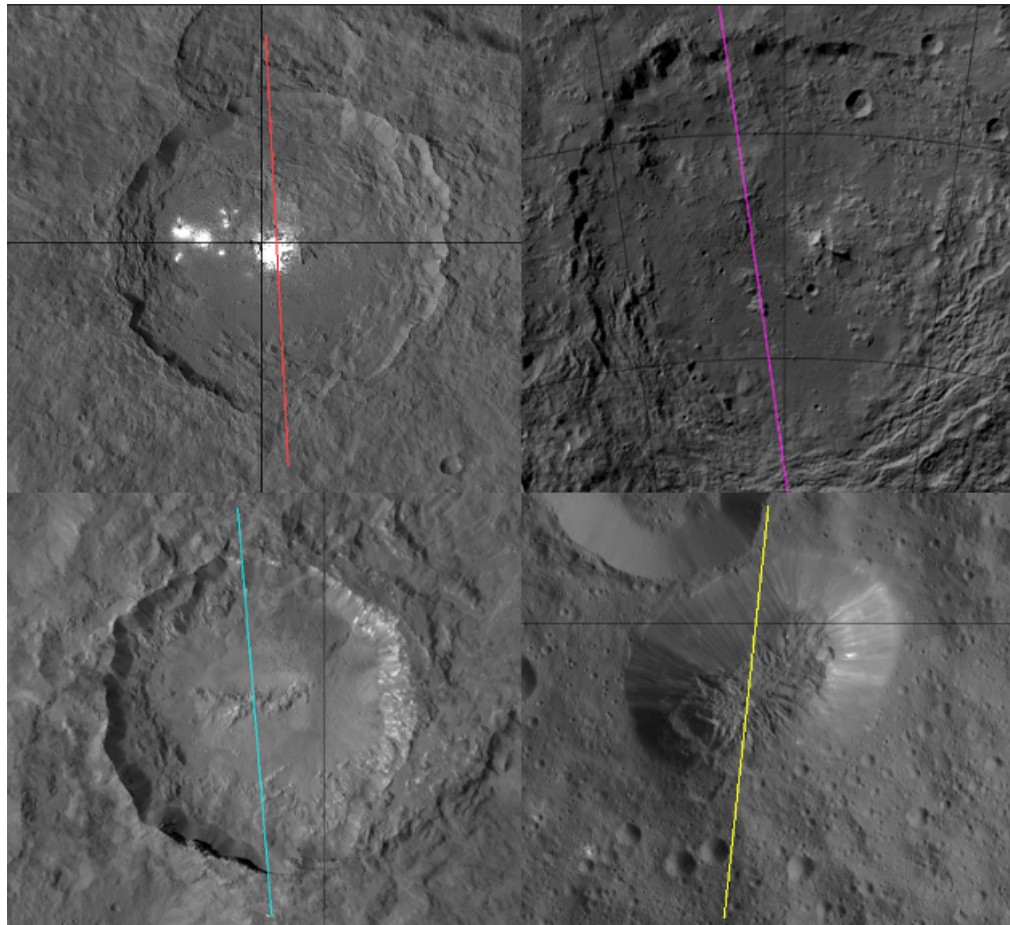


Figure 4.17: 4 main targets of the mission and associated profiles (see part 6.2 for more details). Top left : Occator crater. Top right : Urvara crater. Bottom left : Haulani crater. Bottom right : Ahuna Mons. Images from Dawn LAMO mosaics.

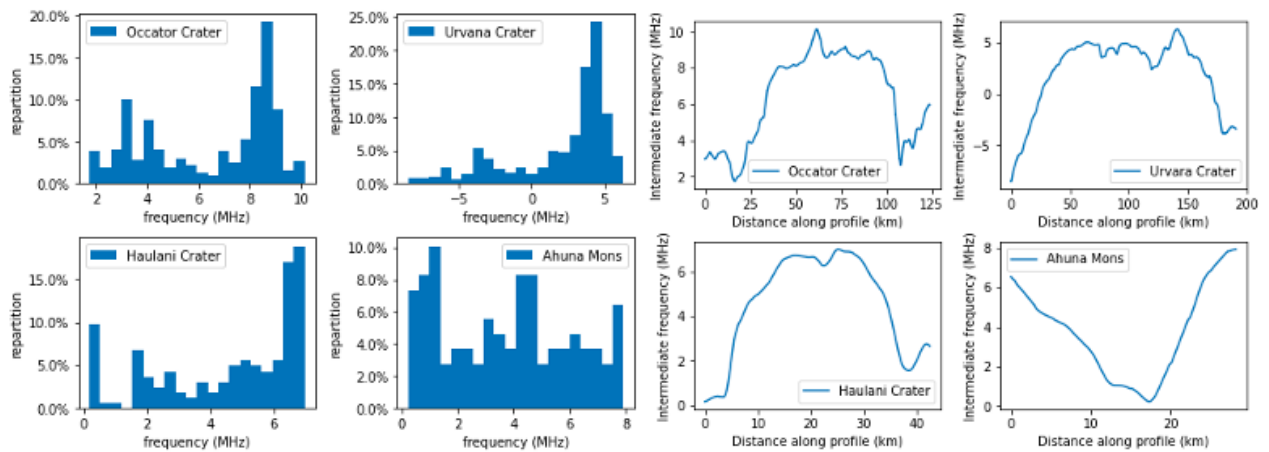


Figure 4.18: Impact of topography of the 4 main targets on maximum expected Intermediate Frequency of the stretch processed signal. Parameters of the stretch processed signal : $\Delta f = 40 \text{ MHz}$, $\tau = 150 \mu\text{s}$. $t_{LO} = 157 \mu\text{s}$ (Occator crater), $211 \mu\text{s}$ (Urvara crater), $181 \mu\text{s}$ (Haulani crater), $163 \mu\text{s}$ (Ahuna Mons). Right : Intermediate Frequency for each target along the profiles drawn on figure 4.17. Left : Histogram of the Intermediate Frequency of each target.

4.3.2 Global performances

4.3.2.1 Penetrating depth and vertical resolution

DRS is a quarter-wave dipole. This gives a constraint on the maximum wavelength which is given by $4 * L$ where L is the size of the dipole. With a size of 7.3 m, the maximum wavelength is then $4 * 7.3 = 29.2$ m. To define the performances of DRS in terms of penetrating depth and vertical resolution, we need to define its central frequency and frequency band. Penetrating depth is directly related to central frequency through skin depth. Skin depth gives a good order of magnitude of the penetrating depth of a radar sounder. Skin depth depends on geological characteristics of surface and subsurface Ceres's composition :

$$\delta_{el} = \frac{\lambda}{4\pi} \left(\frac{\epsilon'}{2} \left(\sqrt{1 + \tan^2 \delta} - 1 \right) \right)$$

with ϵ' the dielectric constant and $\tan \delta$ the loss tangent. We see that skin depth increases with decreasing central frequency. We previously saw that the minimum frequency of our system is constrained ($f_{min} = \frac{c}{4*L}$). Decreasing central frequency will decrease frequency band, defined as $\Delta f = 2 * (f_{central} - f_{min})$.

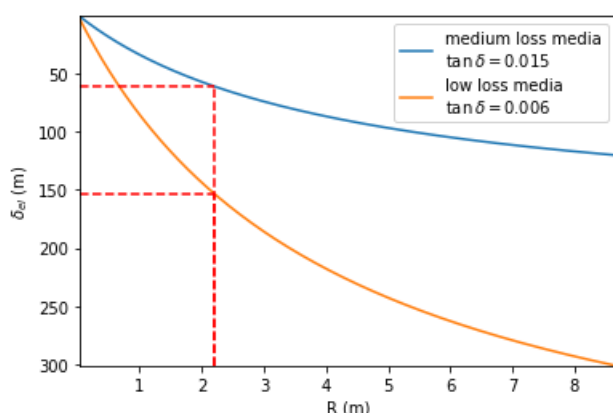


Figure 4.19: Skin depth as a function of vertical resolution on Ceres.

On part 4.2.2.1, we saw that vertical resolution is directly related to frequency band with $R = \frac{c}{2\Delta f}$. Decreasing frequency band will thus degrade vertical resolution. A trade-off between skin depth and vertical resolution has to be found, as illustrated on figure 4.19 for two cases : a low loss media and a Moon-like medium loss media. For the chosen central frequency : 30 MHz corresponding to a wavelength in vacuum of 10 meters, vertical resolution is about 2.2 meters (frequency band is 40 MHz) while skin depth is about 61 meters. In low loss medias, skin depth can reach up to 150 meters or beyond, depending on the value of loss tangents.

4.3.2.2 Power and dynamic range

Power is a very important aspect of the radar. As the signal sent undergoes different sources of attenuation, as well in free air as on the subsurface on Ceres, it is of primary importance to make sure the signal reflected back at the radar will have sufficient power to be detected. For a sounding radar orbiting a planetary surface with no atmosphere such as Ceres, attenuation of the signal is due to the travelling distance of signal in free air along with attenuation of the signal on the subsurface of Ceres. A radar equation can be derived considering all possible sources of attenuation of the signal. Figure 4.20 illustrates a situation of a radar sounder above a planetary surface. For an orbiting radar with a low penetrating depth such as for DRS, attenuation principally comes from attenuation in free air. But a more accurate description should include attenuation on a subsurface in the forms of absorption and scattering, along with transmission coefficient of the surface.

Attenuation due to absorption can be written $A_{att} = e^{-\frac{2d}{\delta_{el}}}$. Attenuation due to scattering A_{sc} is negligible if the size of heterogeneities is much smaller than the wavelength of the signal. With a few meters wavelength signal, it is reasonable to neglect this effect. We can derive the power of received signal in such a case with the following radar equation ([41]):

$$P_r = \frac{P_t * G^2 * \lambda^2 * T^2 * \sigma * g^4 * A_{att} * A_{sc}}{(4 * \pi)^3 * (h + d)^4 * n^2}$$

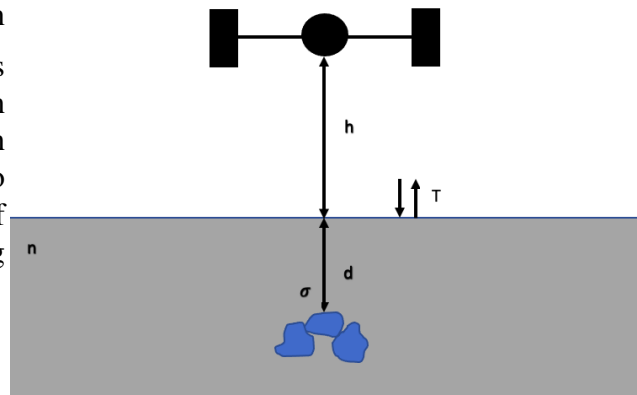


Figure 4.20: Illustration of the radar equation.

where P_r is the received power, P_t is the transmitted power, g is the refraction gain : $g = \frac{h+d}{h+\frac{n}{n}}$, n is the index of refraction, T is the transmissivity at interface between free air and subsurface, G is the gain antenna, σ is the radar cross-section, λ is the wavelength. The radar cross section can be evaluated if we consider an illuminated surface of area A_{surf} , reflectivity Γ and a roughness with Root Mean Square (RMS) slope m , as ([42]) :

$$\sigma = \frac{\Gamma A_{surf}}{2m^2}$$

The illuminated area can be calculated as ([42]):

$$A_{surf} = 2\pi(h + d) \frac{C}{2\Delta f}$$

With stretch processing, SNR can be calculated with :

$$SNR = \frac{P_r * \tau^2}{N_0 \tau_{LO}}$$

with N_0 the noise Power Spectral Density (PSD). N_0 can be theoretically estimated, as it consists in thermal noise plus internal noise :

$$N_0 = kT_0F_N$$

with k the Boltzmann constant, T_0 the equivalent noise temperature and F_N is the noise factor. F_N is a factor quantifying how much additional noise the device will contribute to the noise already from the source. Figure 4.21 displays results obtained for SNR as a function of the RMS slope. Values taken to derive SNR are displayed on table 4.4.

Symbol	Quantity	Unit	Value
P_t	Emitted power	W	1
G	Antenna gain	No unit	1.5
λ	Wavelength	m	10
T	Transmissivity coefficient	No unit	0.9
Γ	Reflectivity coefficient	No unit	0.1
h	Altitude	m	[24000, 28000, 32000]
d	Penetrating depth	m	60
A_{att}	Electrical attenuation coefficient	No unit	0.14 at d = 60 m
n	Refraction index	No unit	$\sqrt{\epsilon'} = \sqrt{3}$
k	Boltzman constant	$m^2 \cdot kg \cdot s^{-2} \cdot K^{-1}$	1.38×10^{-23}
T_0	Equivalent noise temperature	K	290
F_N	Noise factor	No unit	10

Table 4.4: Parameters used for estimation of SNR.

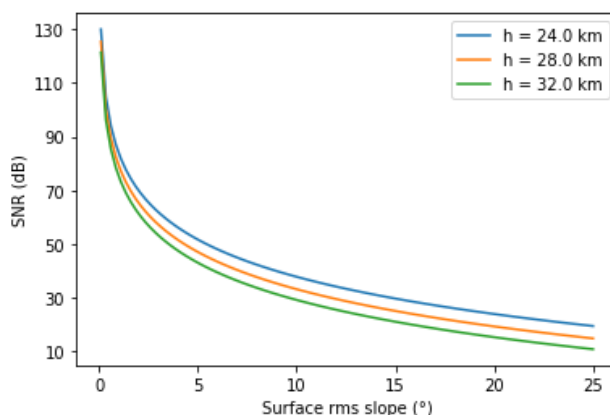


Figure 4.21: calculated SNR for different RMS slopes.

Three different altitudes have been considered to compute SNR. That is because topography of main targets will induce variation of altitude of the satellite (see part 4.3.1 for more details). For a signal to be detected, usual criteria is that SNR is above 3 dB. However, a quantitative analysis of the signal usually requires larger SNR (typically 10 dB). For low roughness, SNR is reasonably good for the full range of altitudes taken by the satellite. SNR could be an issue for very rough terrains, mostly at high altitude, but the values found are still above or around 10 dB to allow us to detect targets in the subsurface of Ceres.

Under nominal operation conditions, DRS will receive strong echoes from the surface of Ceres, followed by weaker echoes from deeper structures within the subsurface. Because the signal is quantified by A/D converter, there is a minimum and a maximum detectable amplitude

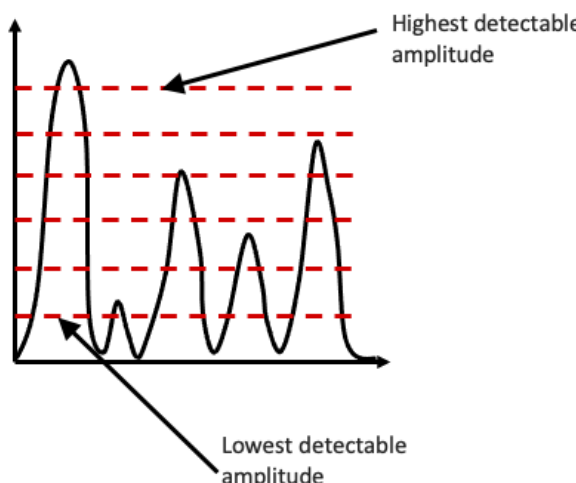


Figure 4.22: Illustration of quantization of a signal.

This is illustrated on figure 4.22. The number of levels of quantization is given by $2^{N_{ADC}}$ where N_{ADC} is the number of bits of the A/D converter. The instantaneous dynamic range is one of the most important characteristics of the instruments. It is defined by the ratio between the strongest and weakest signal that can be measured and can be computed as :

$$\text{Dynamic Range} = 20 * \log_{10} (2^{N_{ADC}})$$

The number of bits of A/D converter of DRS is set to 8 which gives a dynamic range of 48. Note that this value is theoretical.

In practice, this value is slightly reduced because errors reduce the number of effective bits. The number of bits of the A/D converter is an important parameter to take into account, as it defines both the theoretical instantaneous dynamic range and the volume of data produced (see part 7.1), which is a very important aspect of a space mission. A trade-off has to be found as a high number of bits of the A/D converter will produce a higher instantaneous dynamic range but with a more important volume of data.

4.3.2.3 Along-track resolution

Along-track resolution corresponds to resolution in the direction of motion of the satellite. A general rule for deriving along-track resolution is to consider the aperture of the radar antenna in the along-track direction, which can be computed as $\theta_{3dB} = \frac{\lambda}{D}$ where λ is the wavelength of the signal and D the size of the antenna.

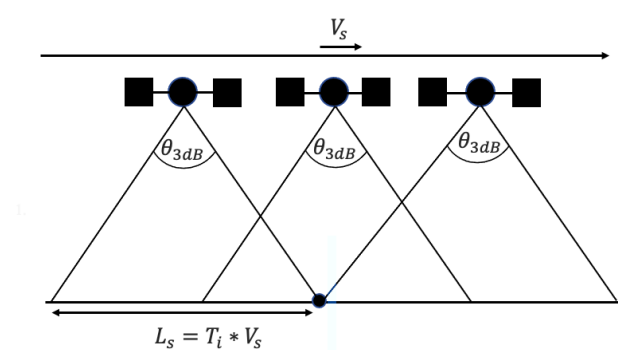


Figure 4.23: Principle of SAR.

This is illustrated in figure 4.23. As the radar is moving at a velocity V_s , a point target on the ground is illuminated by the radar in a time interval T_i called integration time. Integration time can be computed with $T_i = \frac{\theta_{3dB} H}{V_s}$ with H the altitude of the satellite. The length of the synthetic aperture L_s corresponds to the space covered by the radar during T_i . Two targets on the ground can be imaged separately if they are not both within the same radar beam at the same time. This implies that the along-track resolution is $\delta x = L_s = \frac{H\lambda}{D}$.

However, there is a means of improving this resolution. During the integration time, the target is located at different distance from the satellite. This causes a different Doppler shift through time. Therefore, although different targets are present in the same antenna footprint, their return have different Doppler shifts. This is illustrated on figure 4.24. As the radar beam passes over the point target, the distance to the target decreased to a minimum when the satellite flies right above the point target, and then increases again. This causes this hyperbolic line in the azimuth range plane displayed on figure 4.24. There are typically two methods used to use this effect to reduce along-track resolution. Focused Doppler processing makes use of full Doppler shift history of the signal. It consists in coherently summing signals coming from a point target by correcting each target point signal by its own Doppler shift. With focused processing, we can get close to an along-track resolution of $\frac{D}{2}$ with D the size of the antenna. This solution has the inconvenient that it is highly resource demanding and can be very difficult to implement on board, particularly on board a nanosatellite. In the most general case for our kind of satellite, unfocused Doppler processing is used. Unfocused Doppler processing reduces the computation effort of the onboard electronics with respect to focused Doppler processing, at the cost of higher along-track resolution. Instead of making use of the full history of Doppler shifts, unfocused processing makes use of one Doppler shift during a time window t_{window} to correct for signal phase variation during the motion of the satellite. t_{window} is such that signal phase variation during a synthetic aperture stays below a given value, generally $\frac{\pi}{4}$ [43]. Under such condition, the maximum synthetic aperture is $L_s = \sqrt{\frac{H\lambda}{2}}$, which is also the along-track resolution.

The value of the along-track resolution with unfocused Doppler processing is way below the value

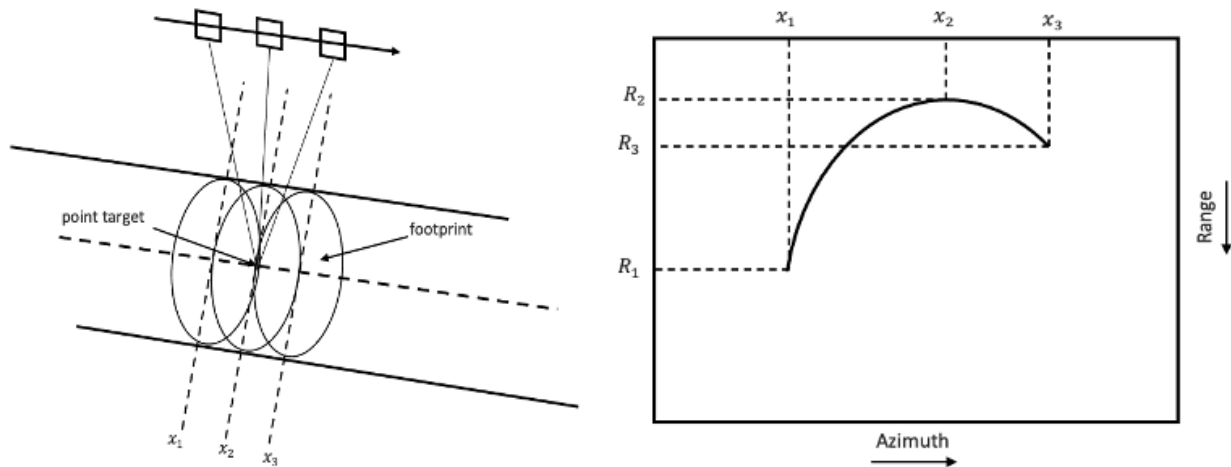


Figure 4.24: Hyperbolic curve traced by a point target in the azimuth range plane. Left : illustration of the variation of the distance between a point target and the satellite. Right : Hyperbolic curve also called range migration curve.

without unfocused Doppler processing. On DRS, with an altitude of about 28 km and a wavelength in vacuum of about 10 m, along-track resolution is about 374 m. Note that this value depends on the altitude of the satellite. As DRS will fly above more or less elevated terrain, this value will be more or less elevated. Table 4.5 sums-up values obtained for along-track resolution considering three different altitudes

Altitude (km)	24	28	34
Along-track resolution (m)	346	374	400

Table 4.5: Values of along-track resolution obtained for different altitudes.

4.4 Summary

Table 4.6 summarizes all discussed parameters for DRS.

Parameters	Symbol	Unit	Value
Radar parameters			
Type of antenna	Not applicable	Not applicable	Dipole
Size of antenna	L	m	7.3
Antenna gain	G	No unit	1.5
Emitted pulse parameters			
Pulse width	τ	μs	150
Frequency band	Δf	MHz	40
Central frequency	f_c	MHz	30
Instantaneous power	P	W	1
Pulse Repetition Frequency	PRF	Hz	20
Stretch processing parameters			
Starting time of local signal mixing	t_{LO}	μs	157-211 (depends on altitude of the satellite)
Pulse width of local signal	τ_{LO}	μs	189
Expected range of Intermediate Frequency	f_{IF}	MHz	0-10.4
Global performances			
Skin depth	δ_{el}	m	A few tens up to 150
Vertical resolution	δ_z	m	2.1
Along-track resolution	δ_x	m	346-400
Signal-to-Noise Ratio	SNR	dB	a few tens
Dynamic range	DR	dB	48
General processing			
Sampling frequency of A/D converter	f_{ech}	MHz	50
Number of bits of A/D converter	N_{ADC}	No unit	8
Method for azimuth compression	Not applicable	Not applicable	Unfocused Doppler processing

Table 4.6: Summary of DRS description.

Chapter 5

Cubesat dimensioning

The CubeSats was created in 1999 by two professors, Bob Twiggs and Jordi Puig-Suari in the United States of America. The main goal of their project was to enable the universities to have affordable access to space. Nowadays, a lot of institutions like universities, schools, commercial and government agencies all around the world develop projects with the CubeSats. Thanks to its low cost, the access to space has sharply increased these last years, leading to an improvement of this affordable spacecraft.

The designation ‘CubeSats’ means a small satellite with a weight limitation of 300 kg and with a specific criteria of shape and size, generally a cube or an assembly of several cubes. The standard CubeSat unit refers to a 1U CubeSat: a 10 cm cube with a mass of approximately 1 to 1,33 kg. Today, many larger sizes have become popular like the 1.5U, 2U, 3U, 6U and 12U.

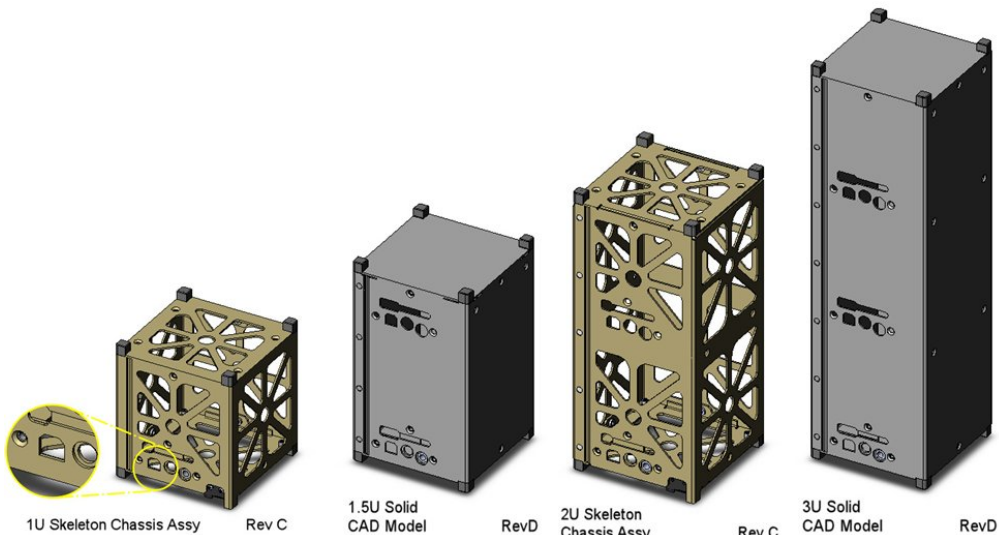


Figure 5.1: Different Cubesat sizes comparaison from AmericaSpace.com.

Thanks to these standards for CubeSats, the cost has been greatly diminished. In fact, the components are made in mass production and are standardized.

Our CubeSat is a 3U. Its main components are the essential ones : OBC, Ka antenna, thermal control, EPS, ADCS, and the payload, which is a radar. We won’t have any propulsion because we decided to make the assumption that we will directly be in our orbit to ease the conception.

As explained in 6 our mission is a piggyback on a satellite, it means that we will be transported to Ceres attached to a bigger mission. Hence, our CubeSat needs a piece to be held : the dispensers. They provide attachment to a launch vehicle, protects the CubeSat during launch and releases it into space. the CubSat is placed in off position in a closed dispenser and attached to the rocket. The release of the CubSat triggers the power-up and the start of the mission,

5.1 Components

5.1.1 OnBoard Computer

An OBC or OnBoard Computer is one of the most important component of the satellite, as the brain he is in charge of the coordination for all systems. It is divided in three categories : a micro-controller, an interface and some electronics. The micro-controller is the processing unit of the OBC dedicated to the data management from every module in the satellite. The interface is responsible for the communication with other modules, it allows them to send information and is in charge of collecting and distributing the power supplied by the solar panel and the battery. The electronics are there to protect the micro-controller and all the other parts from the radiation and magnetic fields.

It goes without saying that it exist multiple OBC available to answer some specific use. In the first part of this we are going to qualify all the specification of our OBC missions and everything that will need to be coded inside the micro-controller. We are then going to bring out our different options that match our requirements and explain our choice.

5.1.1.1 OBC's specifications

In our case, the OBC is not only going to be the system manager, it is also going to be the data transfer platform. It will be in charge to ensure the safety of all the components.

First of all, the OBC should be able to collect parameters from all the components and the payload to decide the activation of the satellite. He must collect parameters such as the temperature of all components, the power available in the battery, but also the orientation from the ADCS and the electric consumption of all systems. He must be capable of analysing this data to decide in which mode the satellite can operate at every moment after the activation. He must be able to decide at all moment if the satellite is capable of using the payload without compromising the future of the mission or the correct timing to transfer the collected data to the orbiter.

Using all those parameters the OBC will be in charge of the distribution of heat and power from the battery and the thermal control system as well. It will also be responsible for the control of the ADCS system. He will be in charge of putting the satellite at the right angle to maximise the solar panels exposition or the radar placement.

As the data transfer platform, the OBC is gonna be in charge of stocking all the data coming out of the radar and transmitting this data to the NASA's orbiter around Ceres. We do need to include enough storage to stock the data for all the main and second target. If the data need to be process to be correctly received by the orbiter, the micro-controller should be prepare to handle it.

The OBC will also be able to receive information from the orbiter, those information can be new commands such as new targets but those commands also should be able to modify the internal code to correct a potential flaw. A reset command for example must be accepted by the computer.

With all those specifications, we can make a list of the necessary specification for the computer. Firstly, the OBC must have all the basic bus such as Inter-Integrated Circuit (I2C), Controller Area Network (CAN), Serial Peripheral Interface (SPI). As the orbit of the NASA mission isn't known, we must choose a OBC with high storage. This could allow us to perform a multitude of flyby to secondary objectives before transmitting the data. For an approximate maximum of 200MB of data that each target could produce, we can ask a minimum of 6GB of data from our OBC.

5.1.1.2 OBC's choice

To this day, many companies are starting to sell flight-proven OBC at reasonable price. After careful consideration, the best choice were the NanoMind from the company GOMSPACE and the ISISPACE OnBoard Computer.

The GOMSMPACE Nano Mind line is a flight proven product. On the new Z7000 the micro-controller is a Zinq-7000 which should offer the software programmability of an ARM-based processor with the hardware programmability of an Field-Programmable Gate Array (FPGA).

It contains a hard drive storage of 32 GB. It is equipped with the obvious I2C and CAN buses. It can endure temperature in a range from -40° to $+85^{\circ}$. The NanoMind z7000 can be plug on the widely used GOMESPACE NanoDock SDR which makes it really easy to integrate in the satellite.

Nevertheless, as we will gain information about the NASA mission, the 2GB of storage of the NanoMind a712d could reveal themselves as sufficient. If the orbits allow us to emit data more frequently this choice should reduce the max power consumption. The NanoMind a712d has been chosen by the future NASA 6U Cubesat Dellingr and is using an flight proven ARM7.

On the other side the OBC from ISISPACE is also a flight proven OBC that offer us a ARM9 micro-controller, possibly 32GB for a temperature range from -25° to $+65^{\circ}$.

The three options are in the same price range and all three are relatively easy to buy and test.

5.1.2 Communication

The communication system is critical to transmit our data to Earth. Since our satellite doesn't have the capacities, in term of configuration management and in terms of power, to communicate directly with Earth, the easiest solution would be to communicate with the NASA orbiter, which will then communicate with ground control.

It exists many frequencies to communicate but one in particular is broadly used in modern space and military communication, the Ka-Band. The Ka-band consists of frequencies in the range 27 GHz to 40 GHz and a wavelength between 1.1 to 0.75 centimeters. The benefits from choosing the Ka frequencies are multiple. It allows us to use much smaller antennas that don't even need to be deployed. The Ka-band in satellite communication also provide high data transmission rates and high bandwidth. This part is extremely valuable in case the window for the data transmission with the NASA orbiter is really rare.

It exists some consumer available option for cubesat such as the Ka-Band Microchip Patch from Printech that you can see on 5.2. This Patch weighs only 9g and operate frequency between 30.5 and 32.5 GHz. It also does survive in temperature between -40°C to $+85^{\circ}\text{C}$, this solution with a precise pointing from the ADCS should be extremely efficient.

5.1.3 Thermal control

5.1.3.1 Introduction

The objective of this section is to study the thermal environment of the satellite. To do this, we must determine the internal and external heat flows brought by the electronic components (dissipating heat), by the sun, and by the albedo of Ceres. It is noted that the satellite's orbit will impact

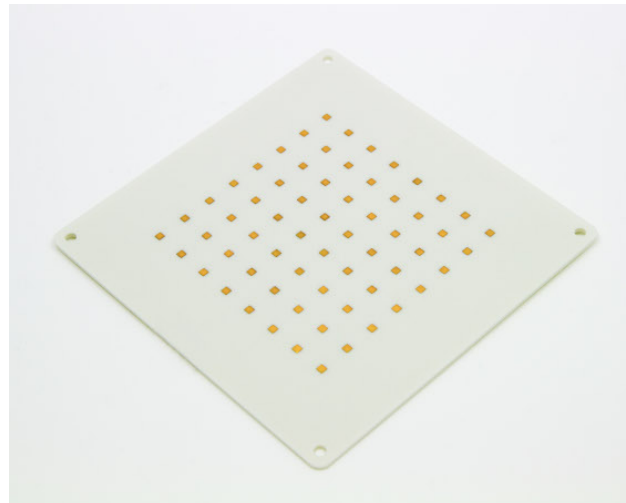


Figure 5.2: A picture of the Ka-Band Microchip Patch from Printech as an example of a Ka-band antenna for cubesat from satsearch.com.

these flows, particularly the one emanating from the Sun. Hence, it is important to distinguish several case studies to tackle all critical situations.

- The case where the satellite is in the Sun.
- The case where the satellite is in the shadow of Ceres.

It can already be predicted that the satellite will be colder in the shadow than in the Sun. The important thing is to maintain operating temperatures consistent with all components of the nanosat.

Bellow is a table presenting the operating temperature ranges of all components:

Components	Operating temp limit °C
ADCS	-40 to 85
DRS	-60 to + 80
OBC	-40 to +60
Structure	-40 to +85
Solar cells	-40 to +85
Battery	-20 to 60

Table 5.1: Operating temperature ranges of all components.

Hence, it can be concluded that it will be necessary to maintain the satellite between -20°C and +60°C to ensure the proper functioning of all its components.

Finally, in our calculation, we will need to consider the solar radiative flux, the planet's reflection related to its albedo, the internal heat dissipation, and the external temperature of space, which is estimated to be 2.7 K. All of this is in order to maintain the satellite within the necessary temperature range for its operation.

5.1.3.2 Solar radiation on Ceres

The solar radiation flux varies depending on the distance from the star to the Sun. Hence, Ceres' orbit eccentricity expresses this flux variation between apogee and perigee. In our case, the eccen-

tricity is $e = 0.0758$. The beam irradiance, in W/m^2 , is given by:

$$I = \frac{S}{r^2} \quad (5.1)$$

where S is the solar constant at the mean Sun-Earth distance of 1 AU, i.e $S = 1371 \text{ W/m}^2$; r is the instantaneous Sun-Ceres distance in AU. According to the table on Ceres' orbit elements, it is known that:

Position	Distance (UA)	I (W/m^2)
Perigee	2,55	210,84
Apogee	2,98	154,38
Mean	2,7650	179,32

Table 5.2: Beam irradiance function of distance.

To make the model easier, the effect of the planet's albedo on the satellite's temperature will not be taken into account. The albedo value is 0.09, which means the contribution of reflected radiation to the total energy received by satellite is relatively small, at 15 W/m^2 . As a result, it will be considered insignificant. This value is obtained by dividing the amount of reflected radiation by the amount of incident radiation.

5.1.3.3 Steady calculation

We will now perform preliminary calculations to get an idea of the satellite's temperature during its orbit. Initially, we will conduct a steady-state analysis to simplify the calculation using the basic energy balance requirement.

$$m \cdot c \cdot \frac{dT}{dt} = \dot{Q}_{in} - \dot{Q}_{out} \quad (5.2)$$

The thermal balance for steady-state is achieved when the heat input into the spacecraft is equal to the heat output from the spacecraft. The heat that enters the spacecraft comes mainly from solar radiation from the space environment. The heat that leaves the spacecraft is mainly lost through radiation, primarily to deep space. In this case $\frac{dT}{dt} = 0$ and that's why we have the following equation:

$$\dot{Q}_{in} = \dot{Q}_{out} \quad (5.3)$$

$$\dot{Q}_{sun} + \underbrace{\dot{Q}_{Albedo}}_0 + \dot{Q}_p = \dot{Q}_{sat \rightarrow ceres} + \dot{Q}_{sat \rightarrow space} \quad (5.4)$$

where:

$$\dot{Q}_{sun} = \alpha_s (4 * A_r + A_s) I_{sun}$$

$$\dot{Q}_{sat \rightarrow ceres} = \epsilon_{IRA} F_{sat \rightarrow ceres} \sigma (T_{sat}^4 - T_{ceres}^4) \approx 0 \text{ considered } T_{sat} \approx T_{ceres}$$

$$\dot{Q}_{sat \rightarrow space} = \epsilon_{IRA} F_{sat \rightarrow space} \sigma (T_{sat}^4 - T_{space}^4)$$

$$A_{sat} F_{sat \rightarrow ceres} = A_s$$

$$A_{sat} F_{sat \rightarrow space} = 4 \cdot A_r + 2 \cdot A_s - A_{sat} F_{sat \rightarrow ceres} = 4 \cdot A_r + A_s$$

- \dot{Q}_p = Electrical power dissipation
 α_s = Absorptivity
 ε_{IR} = Emissivity
 σ = Stefan-Boltzman constant
 A_s = Projected surface area of one square
 A_r = Projected surface area of one rectangular face
 A_{sat} = Total projected surface

5.1.3.4 Properties of materials

The external surfaces of a spacecraft radiatively couple the spacecraft to space. Therefore, it is important to have knowledge of the materials' properties to perform the study.

	Structure	Solar cells
Conductivity [W/(m*K)]	167	200
Specific Heat [J/(kg*K)]	896	1600
Emissivity (thermal)	0,039	0,85
Absorptivity (solar)	0,31	0,92

Table 5.3: Material properties of Diplona.

For the Diplona spacecraft, the surface is composed of approximately 60% aluminum alloy and 40% solar cells. Therefore, it is important to determine an average material property for thermal analysis.

$$\dot{Q}_{Ap} = \dot{Q}_{Al} + \dot{Q}_{sc} \quad (5.5)$$

where :

$$\dot{Q}_{sc} = \varepsilon_{sc} \cdot A_{sc} \cdot \sigma \cdot T_{sc}^4$$

$$\begin{aligned}\dot{Q}_{Al} &= \varepsilon_{Al} \cdot A_{Al} \cdot \sigma \cdot T_{Al}^4 \\ T_{sc} &= T_{Al}\end{aligned}$$

using the equation (5.5)

$$\begin{aligned}\varepsilon_{Al-Sc} \cdot A_p \cdot \sigma T^4 &= \sigma \cdot T^4 \cdot (\varepsilon_{sc} \cdot A_{sc} + \varepsilon_{Al} \cdot A_{Al}) \\ \varepsilon_{Al-Sc} &= \varepsilon_{sc} \cdot \frac{A_{sc}}{A_p} + \varepsilon_{Al} \cdot \frac{A_{Al}}{A_p}\end{aligned}$$

For the sides 2,6 (covered with 78% solar cells and 22% aluminium) it follows:

$$\varepsilon_{Al-Sc} = 0.85 \cdot 0.78 + 0.039 \cdot 0.22 = 0,672$$

$$\alpha_{Al-Sc} = 0.92 \cdot 0.78 + 0.31 \cdot 0.22 = 0.786$$

For the sides 5 (covered with 74% solar cells and 26% aluminium) it follows:

$$\epsilon_{Al-Sc} = 0.85 \cdot 0.74 + 0.039 \cdot 0.26 = 0,639$$

$$\alpha_{Al-Sc} = 0.92 \cdot 0.74 + 0.31 \cdot 0.26 = 0,7614$$

Finally, we have this table with all of the emissivity and absorptivity needed.

Nanosat surface	ϵ	α	Coverage
1	0.039	0.31	100% St
2	0,672	0.786	22% St and 78% Sc
3	0.039	0.31	100% St
4	0.039	0.31	100% St
5	0,639	0,7614	26% St and 74% Sc
6	0,672	0.786	22% St and 78% Sc

Table 5.4: Average of optical surface properties for partially covered surfaces.

The structure is given by 5.3 :

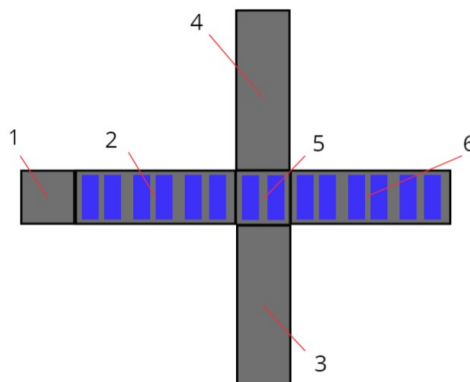


Figure 5.3: Structure of Diploma, 1 is front side 5 is rear side.

Having determined the important values for simulating the temperature of our satellite, we will now conduct the thermal study to obtain the temperatures. We will be able to verify if the temperatures are consistent with the operating temperature ranges of the components.

5.1.3.5 Temperature equilibrium with electrical power dissipation on board

In this chapter, we will do the calculations for the equilibrium temperature, including the dissipated power, which is present inside the satellite.

The calculation of the steady-state temperatures uses a basic energy balance. The equilibrium temperature is obtained from condition $\dot{Q}_{in} = \dot{Q}_{out}$. The effects included in the calculation are solar radiation and radiation from the body to space.

$$\alpha_s(4 \cdot A_r + A_s)I_{sun} + \dot{Q}_p = (4 \cdot A_r + A_s) \cdot \varepsilon_{IR}^* \cdot \sigma (T_{sat}^4 - T_{space}^4) \quad (5.6)$$

$$T = \sqrt[4]{\underbrace{\frac{\alpha_s(4 \cdot A_r + A_s)I_{sun}}{(4 \cdot A_r + A_s) \cdot \varepsilon_{IR}^* \cdot \sigma}}_{Sun} + \underbrace{\frac{\dot{Q}_p}{(4 \cdot A_r + A_s) \cdot \varepsilon_{IR}^* \cdot \sigma}}_{Electrical} + T_{space}^4} \quad (5.7)$$

α_s = Solar absorptivity

ε_{IR}^* = Average emissivity value, for the sum of areas that interacts with deep space

$$\varepsilon_{IR}^* = \frac{2 \cdot \varepsilon_{Al-Sc} + 2 \cdot \varepsilon_{Al} + 1 \cdot \varepsilon_{Al-Sc}}{5}$$

We will now distinguish between the case where the satellite is exposed to the Sun and the case where it is in the shadow. The temperature is obtained using:

$$T = \sqrt[4]{\underbrace{\frac{\dot{Q}_p}{(4 \cdot A_r + A_s) \cdot \varepsilon_{IR}^* \cdot \sigma}}_{Electrical} + T_{space}^4} \quad (5.8)$$

Results are given by 5.5:

Case	Temperature °C
Worst hot case	5
Worst cold case eclipse	-78

Table 5.5: Temperature of side oriented to Ceres.

The results shown in 5.5 only express the temperature of one face. Given the size of the satellite, we will consider these values to be constant throughout the satellite.

We see that the satellite is far too cold in the worst cold case to ensure the proper functioning of the internal components. Therefore, we will have to implement solutions to increase the temperature of the satellite.

In reality, during its orbit, the satellite will transition from being in the Sun to being in the shadow of the planet. The temperature will begin to decrease when it is behind the planet, but if it does not remain there for a sufficient amount of time, perhaps the temperature will not reach the minimum value of -78°C. It will therefore be necessary to perform a study on an unsteady state to have more information on the evolution of temperature over time, which we will do in the following section.

5.1.3.6 Instationary calculation

To perform the unsteady state study, we start with the basic equation:

$$m \cdot c \cdot \frac{dT}{dt} = \dot{Q}_{in} - \dot{Q}_{out}$$

In this case $\frac{dT}{dt}$ is no longer equal to 0. However $\dot{Q_{in}}$ and $\dot{Q_{out}}$ are the same as before. Then we must solve the differential equation. We performed the resolution using Matlab, the curve expressing the results are shown in 5.4 and 5.5:

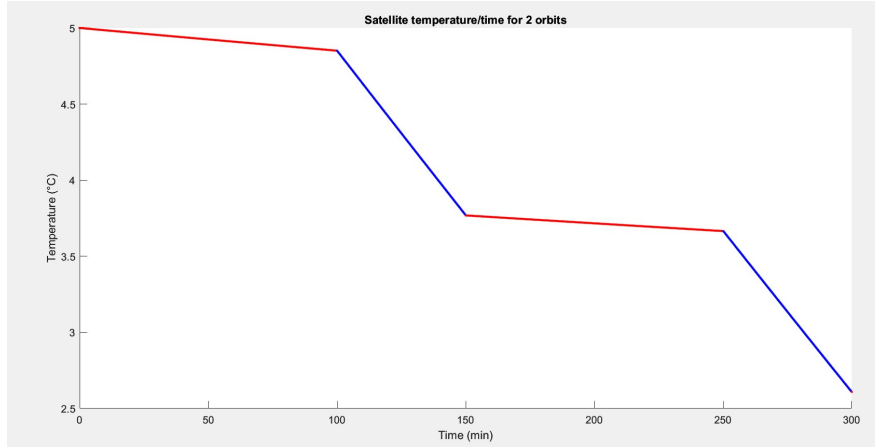


Figure 5.4: Satellite temperature/time for 2 orbits. The red curve corresponds to the moment when the satellite passes into the Sun and the blue curve when it is in the shadow of Ceres.

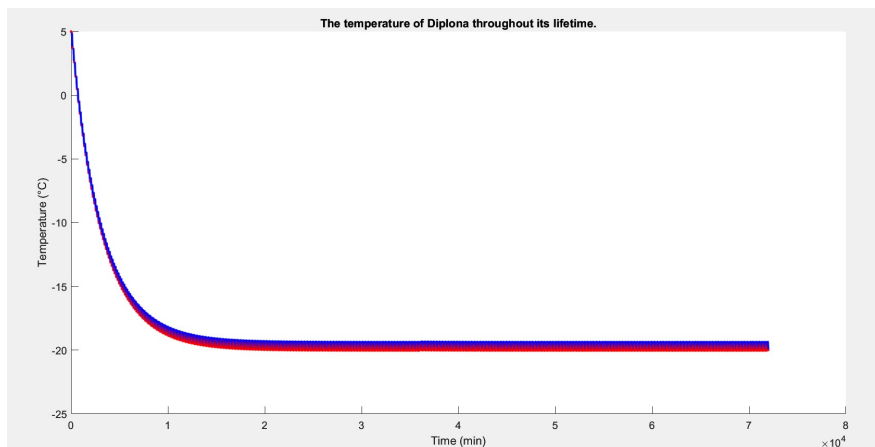


Figure 5.5: Satellite temperature/time for its entire life. We notice that the temperature decreases until it stabilizes at around -19.5 degrees Celsius.

5.1.3.7 Comparison with SimScale

We compared our results with the thermal modeling software: SimScale. The results are shown in 5.6:

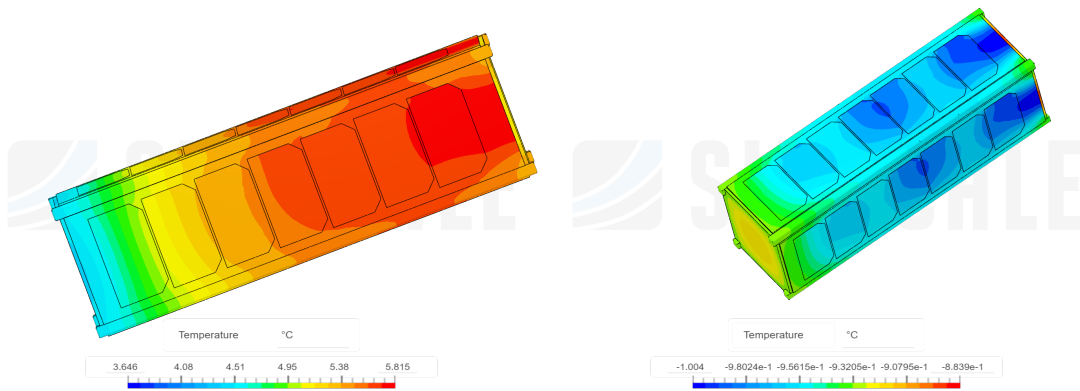


Figure 5.6: SimScale simulation, hot case / simulation, cold case. The sunny side is warmer and the temperature decreases along the satellite.

It can be seen that the order of magnitude is respected for the sunlit phase of the satellite, however, when the solar flux is removed, the satellite does not reach the minimum values obtained during the steady-state study. This clearly proves the hypothesis we made before on the importance of knowing the eclipse time of the satellite's orbit to have a consistent temperature. We also notice that the temperature is -1°C for the cold phase. We have such a value because the software study does not take into account the time in the shade but only the incoming and outgoing flows. The initial conditions would have to be changed to refine and obtain the results of the unsteady study in 5.7:

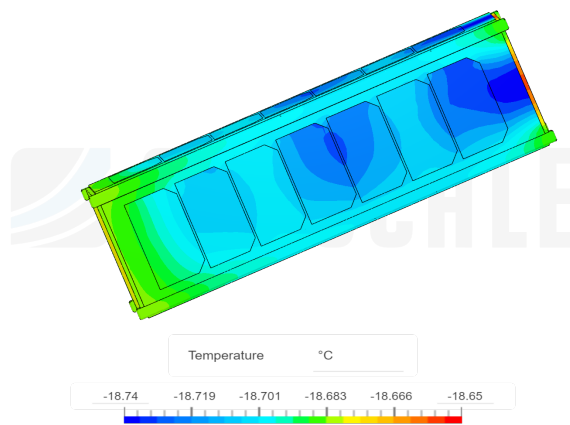


Figure 5.7: SimScale simulation, cold case with initial condition at infinity.

The fact is that the temperature lost by radiation is low and that one must remain in the shadow for a long time to cool down the satellite.

5.1.3.8 Thermal management solution

The main function of thermal control is to maintain satellite equipment within the required temperature limits, through the identification of appropriate thermal control techniques and hardware, according to the complexity and the category of the satellite.

Following the temperatures we obtained during the part 5.1.3.6, it is important to implement a system to allow for a margin of operation. Indeed, we want to be in -20 °C and +60 °C. In order to have a reasonable margin, it would be necessary to warm up the satellite a bit, especially before it starts to reach the limit values of its temperature.

Simplicity and flexibility are the key drivers for the choice of the most appropriate thermal control techniques. In case thermal requirements are not fully met and problems arise at the system level, the following actions may be implemented:

- Change of materials. Moreover, it is also limited by the availability of materials that may be either already in-house or anyway easily accessible on the market.
- Selection of components with the appropriate temperature range.
- Installation of heaters on components that need to be warmed up.

5.1.4 Electric Power System

5.1.4.1 Introduction

The Electric Power System EPS is a critical component of any CubeSat mission as it provides power to all the subsystems. The EPS is responsible for generating, storing, and distributing electrical power throughout the spacecraft.

The EPS typically consists of solar panels, a power management unit (PMU), and a battery. The solar panels are used to generate power from sunlight and convert it to electrical energy. The PMU regulates the voltage and current of the solar panels, charges the battery, and manages the distribution of power to the various subsystems. The battery is used to store excess power generated by the solar panels and provides power to the spacecraft during periods of low or no sunlight.

The EPS must be designed to operate within the constraints of the CubeSat form factor, which imposes limitations on the size and weight of the system. The solar panels must be compact and efficient enough to provide sufficient power to the spacecraft, while the battery must be lightweight and able to withstand the harsh conditions of space.

5.1.4.2 PMU

We have decided to use the NanoPower P31u from GomSpace for Diploma for several reasons.

Firstly, it is compact and lightweight, making it ideal for small spacecraft. Secondly, it integrates several functions into a single unit, including a solar power harvester, Max Pointing Power Tracking (MPPT), battery charger, battery protection circuit, and power distribution system.

This can save space and reduce complexity in the overall design of the CubeSat. Thirdly, it is highly efficient, with an MPPT that ensures the solar panels operate at their maximum efficiency,

and a battery protection circuit that helps extend the lifespan of the onboard battery. Fourthly, it is radiation tolerant, making it suitable for missions that require this feature. Finally, it has a proven track record of reliability, which can provide peace of mind for mission operators. Overall, the NanoPower P31u is a versatile and reliable PMU that can help ensure the success of our CubeSat mission.

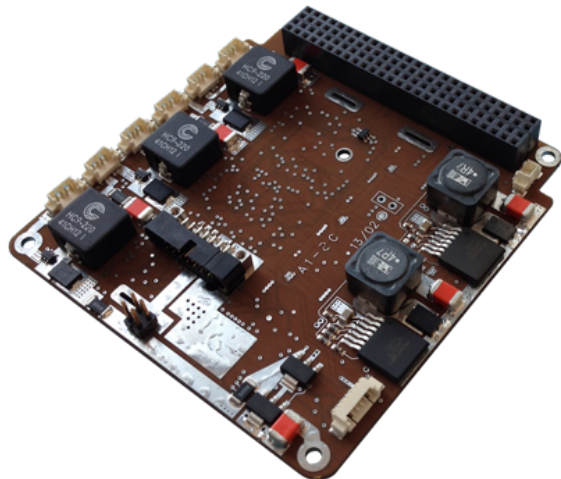


Figure 5.8: PMU: This is a picture of the GomSpace NanoPower P31u that will be used in the satellite from Gomspace.com.

5.1.4.3 Battery

As the PMU, our battery is from Gomspace. It's The NanoPower BPX. Known as a high-efficiency battery pack, it will suit perfectly to our satellite.

The BPX is a lightweight and compact battery pack that offers high energy density and reliable performance. It is designed to work in conjunction with the NanoPower P31u PMU, providing a reliable power source for the satellite. The BPX uses Lithium-polymer cells that have a high cycle life and can be recharged quickly. The cells are protected by an integrated battery management system that monitors the cells' voltage, temperature, and current, ensuring that the battery operates within safe limits. As we are looking for a reliable and high-performance battery pack for Diplona, it seems like the best choice to make.



Figure 5.9: PMU : A picture of the GomSpace NanoPower BPX from Gomspace.com.

5.1.4.4 Solar panels and power obtained

In this section, we are going to determine the power we can pretend to gain with our solar panels. The solar panels will be very important to ensure the lifetime of the satellite. Indeed, during the flight phases exposed to the Sun, we can expect to regain energy to maximize the power available throughout the orbits. It is therefore important to determine how much electrical power we can regain with all our solar panels. In this way, we can check that the satellite has the energy capacity to keep the components alive. Diplona is a nanosatellite that has two lateral 3U panels and four deployable 3U panels. In total there are six 3U panels and one 1U panel. Each 3U panel is composed of seven solar cells and the 1U panel of two solar cells. Each of these solar cells has a size of 30,18 cm².

The total area can be calculated as follows:

$$\text{Area} = 6 * A_{3U} + 1 * A_{1U} = 0.1328 \text{m}^2$$

with:

$$A_{3U} = 211.26 * 10^{-4} \text{m}^2$$

$$A_{1U} = 60.36 * 10^{-4} \text{m}^2$$

It is important to note that the panels we have chosen have an efficiency of about 30%. Thus on the total incident solar flux, they will only convert one-third of the power.

We have seen in the previous section that the average incident solar flux is 180W/m². This is relatively low compared to the flux that the earth would receive. The energy that could be extracted from all the panels is described by the following calculation:

$$P_{sp} = \underbrace{0.30}_{\text{Efficiency}} * \underbrace{I}_{\text{Beamirradiance}} * \text{Area} \approx 7 \text{W}$$

We can see that we can expect to gain 7W in total per hour on the sunlit phases. This is relatively low, but we will check if it is sufficient.

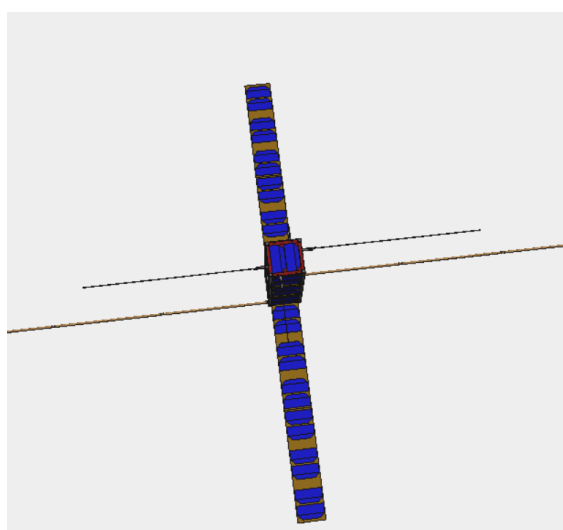


Figure 5.10: View of Diplona's Solar Panels. We have four 3U solar panels deployed, two 3U solar panels on the side and one 1U solar panel on top of Diplona.

5.1.5 Attitude and Determination Control System

5.1.5.1 Introduction

The Attitude Determination and Control System, ADCS, provides pointing accuracy and stability of the payload and antennas.

The ADCS is divided into 4 modules: the sensors, the actuators (Actuator (ACT)), the ADCS Controller and the Interface. 5.11 5.12

- The sensors harvests data in order to get information about the CubeSat position. There are two types of sensors : the absolute sensors to get constant access to the attitude relative to an external frame. And relative sensors to get access to the current attitude relative to the previous one.
- The ACT goal is to adapt the CubeSat's attitude according to the mission needs, by rotating it around three axes : yaw, pitch and roll. The actuator system is placed to have control on the three axes (x,y,z).
- The ADCS controller objectives are to collect data from sensors and to process it to get reliable positioning information. Then the ADCS sends orders to ACT in order to determine the rotations to accomplish for each axis and to correct the CubeSat's attitude.
- The Interface module is the hardware part of ADCS. It has the objective to ensure good connection with other systems of the satellite and to send data to the other systems. The INT transmits the signal received from sensors to the micro-controller and it also distributes power supply coming from the EPS subsystem to the actuators.

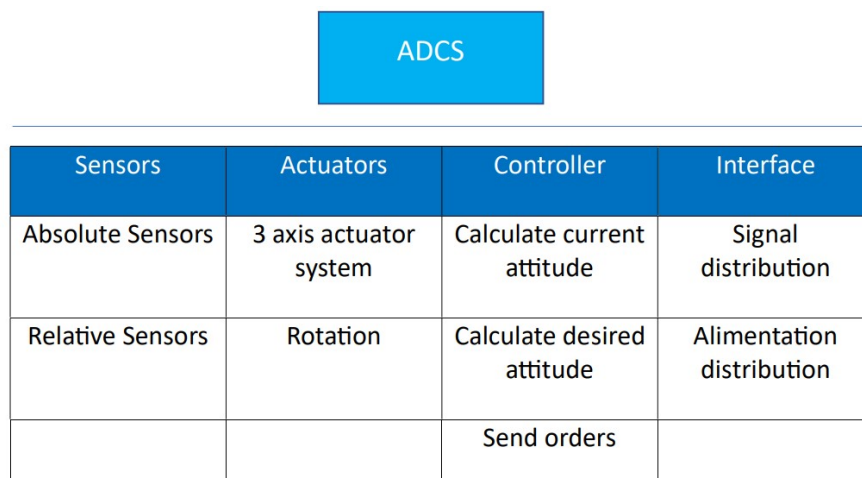


Figure 5.11: ADCS subsystems. Description of the roles during an ADCS action.

5.1.5.2 Our ADCS

By the characteristics of Ceres, we have been restricted by the choice of ADCS we have.

Indeed, magnetorquers are magnetic coils that generate a magnetic field to interact with the Earth's magnetic field and control the attitude of a spacecraft. However, using magnetorquers to control

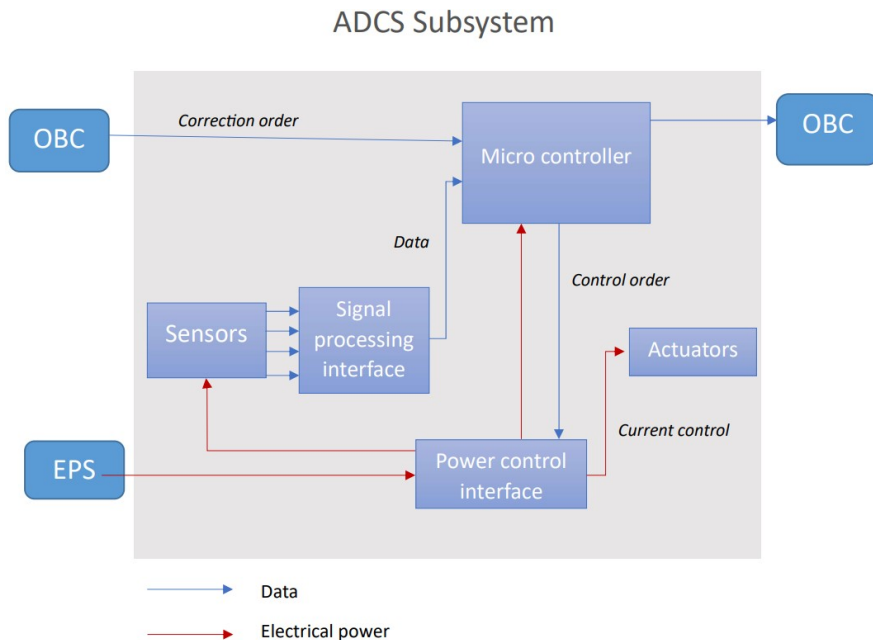


Figure 5.12: ADCS subsystems. This graph gives us the link between the OBC, EPS and the ADCS system.

the attitude of a spacecraft around Ceres is not possible due to the absence of a significant magnetic field on the dwarf planet. Unlike Earth, which has a strong magnetic field generated by its core, Ceres does not have a significant magnetic field. Therefore, magnetorquers cannot be used to control the attitude of a spacecraft around Ceres. Other attitude control methods, such as reaction wheels or thrusters, would need to be used instead.

And as we said we won't use neither thrusters because of the lack of space and mass limit. So our last method is the reaction wheels. In Diplona we have four.

Having four reaction wheels is preferred over having only three because it provides redundancy and improves the spacecraft's overall performance. A spacecraft's attitude can be controlled by changing the momentum of the reaction wheels. With four reaction wheels, the spacecraft has more flexibility in controlling its attitude and can perform more complex maneuvers, such as slewing or pointing the spacecraft in a different direction. In addition, having four reaction wheels increases the spacecraft's stability, which is critical for many missions, especially for those that require high pointing accuracy as Diplona.

If one reaction wheel fails, having three remaining wheels may not be sufficient to maintain the spacecraft's stability and pointing accuracy. With four reaction wheels, the remaining wheels can compensate for the failed one, ensuring the spacecraft remains stable and on course.

5.1.6 Structure

5.1.6.1 Diplona 3U

The choice of a 3U CubeSat was driven by our mission, launch opportunities, and cost. 3U CubeSats are a popular choice because they offer a good balance between performance and cost. They have a larger volume than 1U or 2U CubeSats, which provides more space for payloads and allows for more complex missions. However, they are still small enough to be deployed from a

range of launch vehicles, which increases the chances of finding a suitable launch opportunity. In addition, the cost of building and launching a 3U CubeSat is often lower than that of a larger spacecraft, making it a more accessible option for many organizations. The 3U CubeSat form factor has also become more standardized, which means that there are a variety of off-the-shelf components and subsystems available, which can further reduce development time and cost. And that is exactly what we are looking for.

And like a large majority, our structure is made of Aluminum 6061 (5.13); it is one of the most used materials in Aeronautics, armament, and space thanks to its properties such as its behavior in the atmosphere, its machining, its resistivity and its density.



Figure 5.13: ISIS 3U, Diploma's Structure made in AL6061. www.isispace.nl.

5.1.6.2 Dispenser

Diploma will be attached to another satellite via a dispenser for cruising to Ceres. The technical solution for the transport of the CubeSat with the main satellite is an interface named dispenser. The dispensers are used to attach several micro and nanosatellites on a satellite. They permit the launch of more satellites. There are mainly two types of dispensers : the first system uses a rail design whereas the second system uses a tab design and employs a constraint mechanism with a flange that clamps onto these tabs. To ensure the safety and success of the mission, and since it is a three units, the CubeSats will be compatible with the rail system by meeting the applicable requirements. (5.14)

5.2 Payload

Our Payload is the DRS. It's presented in the part 4.2.



Figure 5.14: Example of a dispenser: the ISISPOD 3U.

5.2.1 IDM-CIC

5.2.1.1 Introduction

IDM-CIC, is a powerful software tool developed by Centre National d'Etude Spatiale (CNES) for processing, analyzing, and modeling altimetry data. Altimetry data refers to measurements of height or altitude above a reference surface, such as the Earth's surface or the surface of a planet or moon. IDM-CIC allows for data processing, quality control, and validation, as well as the generation of scientific products and visualizations. It also includes a range of advanced features, such as the ability to handle large datasets and to perform complex calculations and modeling tasks.

In addition to its data processing capabilities, IDM-CIC can also be used for satellite design. The software allows for the pre-design and simulation of satellite altimetry instruments, which can help to optimize the scientific objectives of a mission and reduce the risk of costly design errors during the actual mission. IDM-CIC can model the altimeter instrument and its interaction with the environment to determine the expected performance of the instrument, including its accuracy and precision. The software also allows for the generation of simulated data, which can be used to develop and validate data processing algorithms before the actual mission. And we have used it especially to pre-design our little satellite: Diploma.

5.2.1.2 Diploma

The assembly of Diploma (5.15) is important because it determines the physical structure of the satellite and affects its performance and functionality in space. The assembly process involves integrating various subsystems, such as power, communication, payload and ensuring they work together as a cohesive unit. A well-designed and properly assembled CubeSat can withstand the harsh environment of space and carry out its intended mission effectively, while a poorly assembled CubeSat may fail or underperform.

5.2.1.3 Mass Budget

Diploma is a 3U Nanosat, and we have to respect a maximum weight of 6kg. That is not a lot and that's why we had to choose carefully our components. And as you can see in the image 5.16, we put a 20% maring as we are only in the pre-design. We conclude by its weight that it should be

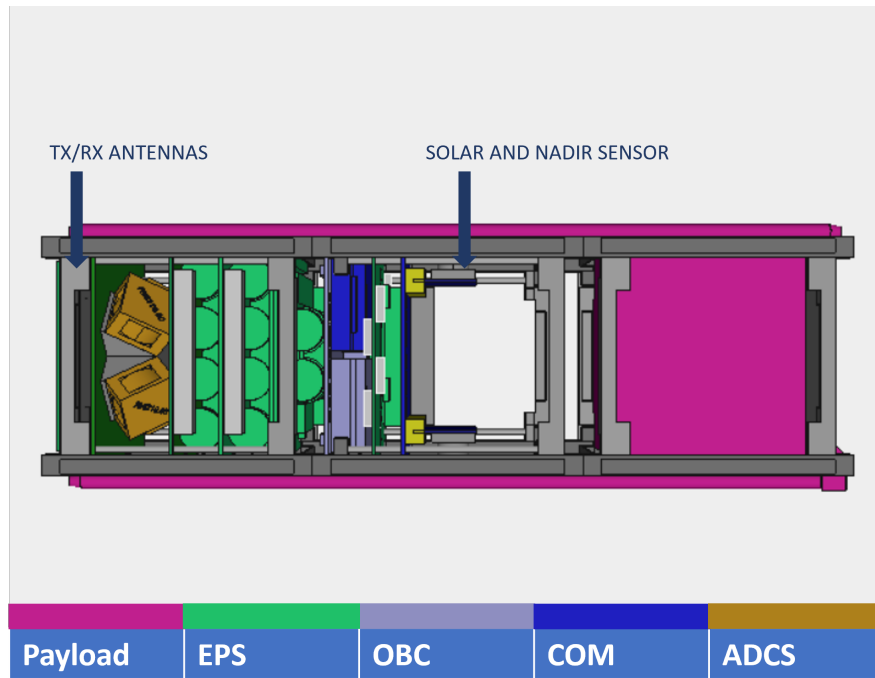


Figure 5.15: Assembly of Diplona. We have in pink, our payload composed of the DRS and the antennas on the side. In green, it's all the electric power system. In gray, the OBC is used to control the satellite. In blue, the communication system is combined with our TX/RX antennas. And finally, in brown we have the ADCS, used to control the position of the satellite. The solar and nadir sensor is used to know the geographic position of Diplona.

fine.

5.2.1.4 Power Budget

While the power budget provides important information on how much power each mode will consume, it can be difficult to understand the significance of the numbers without putting them into the context of a real mission application (you can see it here 5.17). That's where flight management comes in. By analyzing the power budget in conjunction with other key mission parameters such as mission duration, orbit characteristics, and payload requirements, flight management can create a realistic scenario for the power consumption of the satellite during its operational lifetime. This information is critical for making informed decisions about the design of the satellite and the selection of components, and can ultimately ensure the success of the mission. You can see our in the section 6.5.2.

5.2.1.5 Configuration Modes

We have three configuration mode: launch (5.18), deployment (5.19), orbit (5.20).

Configuration :				Reference											
Diplona				Target wet mass [Kg]		0									
Subsystem		Unit		Forced values		Without margin [Kg]		Margin [%]		Margin [Kg]		Including margin [Kg]		% of total	
+	-	Name	Quantity	Mass [Kg]	Margin [%]	Mass [Kg]	Margin [%]	Without margin [Kg]	Margin [%]	Margin [Kg]	Including margin [Kg]				
Subsystem STR		ISIS 3U	1	0,57	20,00%			0,64	18,25%	0,12	0,76			14,54%	
		Generic PCB	1	0,08	5,00%			0,08	5,00%	0,00	0,08				
Subsystem COM		Gomspace TR-600	1	0,03	15,00%			0,13	7,31%	0,01	0,14			2,66%	
		ISIS VHF UHF Antenna Dip	1	0,10	5,00%			0,10	5,00%	0,01	0,11				
Subsystem PWR		Gomspace P110 C Solar Panel	1	0,03	5,00%			0,03	5,00%	0,00	0,03			40,08%	
		▀ 3U Generic Deployable Sol.	4	0,28	10,00%			1,12	10,00%	0,11	1,23				
Subsystem OBC		1 3U Generic Solar Panel	2	0,14	10,00%			0,28	10,00%	0,03	0,31				
		Gomspace - NanoDock DMC	1	0,05	20,00%			0,05	20,00%	0,01	0,06				
Subsystem ADCS		Gomspace - NanoPower BP4	2	0,27	5,00%			0,54	5,00%	0,03	0,57				
		Gomspace - NanoPower P31	1	0,20	5,00%			0,20	5,00%	0,01	0,21				
Subsystem PAY								0,10	18,62%	0,02	0,12			2,32%	
		Gomspace - NanoMind 2700	1	0,03	15,00%			0,03	15,00%	0,00	0,03				
System		Gomspace - NanoDock SDR	1	0,07	20,00%			0,07	20,00%	0,01	0,09				
		Total dry mass without system margin				4,62	13,55%	0,63	5,24						
System margin							15,00%	0,79	6,03						
Total wet mass including all margins									6,03						
Total dry mass without system margins							Without margin [Kg]	Margin [%]	Margin [Kg]	Including margin [Kg]					
Total dry mass including system margins							4,62	13,55%	0,63	5,24					
Total propellant mass							0,00	0,00%	0,00	0,00					
Total propellant mass including system margin								20,00%	0,00	0,00					
Total wet mass including all margins									6,03						

Figure 5.16: Diplona's Budget Mass from our IDM-CIC. As we see, we are practically at 6kg with 20% of margin which allows us more possibilities for the next phases.

Diplona		*		*		*		*		*		*		*	
+ Subsystem	-	Unit	Instance	Element Modes >	IDLE	ACQUISITION	DETUMBLING	POINTING	SURVIVAL	RECEPTION	TRANSMISSION				
Configuration :					Cons. [W]	Diss. [W]	Cons. [W]	Diss. [W]	Cons. [W]	Diss. [W]	Cons. [W]	Diss. [W]	Cons. [W]	Diss. [W]	
Power without margin					0,115	0,115	23,352	5,312	34,532	34,532	32,672	32,642	2,692	16,352	
Power including margin					0,1285	0,1285	23,6855	5,6415	37,8835	37,8835	35,8375	35,8045	2,9595	17,5855	
System power margin				20,00%	0,03036	0,03036	5,68452	1,35396	9,09204	9,09204	8,601	8,93308	0,71028	4,22052	
Total power including system margin					0,1518	0,1518	28,4226	6,7698	45,4602	45,4602	43,005	42,9654	3,5514	21,1026	

Figure 5.17: Diplona's Power Budget from IDM-CIC. It shows us the power we have during all the modes we will face during the mission.

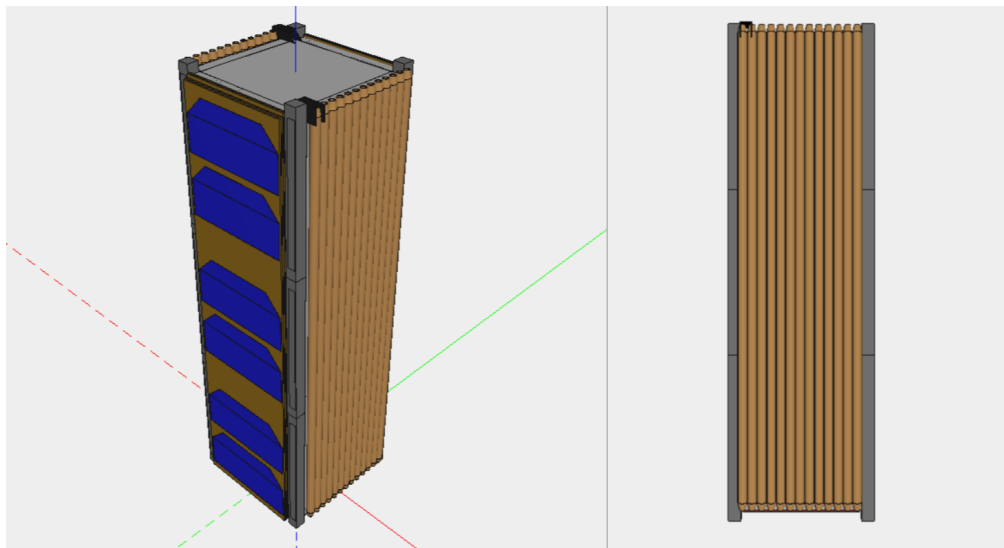


Figure 5.18: Launch Mode. Everything is OFF, the dipole's antenna and the solar panels are folded onto the satellite sides. This model is coming from the IDM-CIC model.

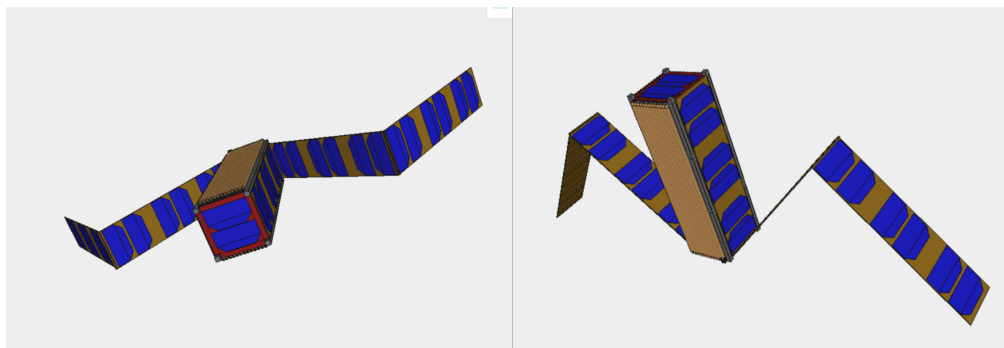


Figure 5.19: Deployment mode. The solar panels and the radar are being deployed. This is what the first detumbling mode will look like. This model is coming from the IDM-CIC model.

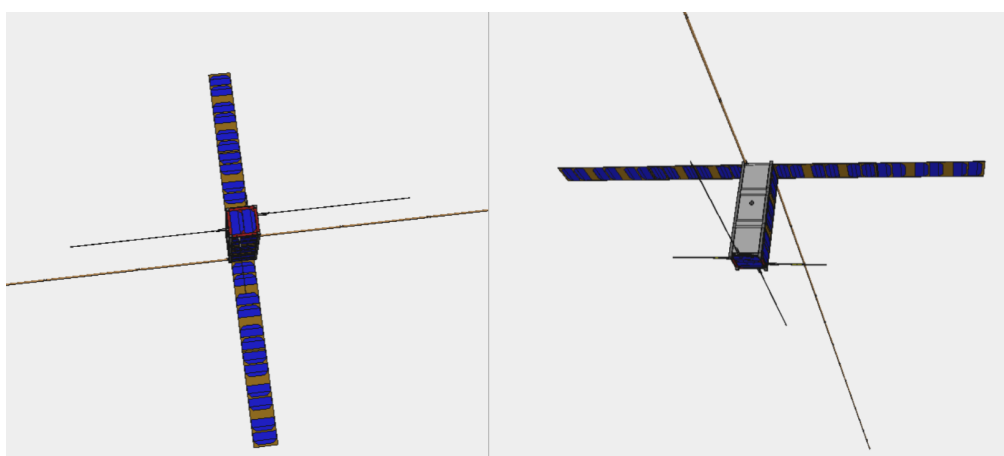


Figure 5.20: Orbital mode. Everything is deployed and Diploma is in active mode this is how it will look after the first detumbling mode. This model is coming from the IDM-CIC model.

Chapter 6

Mission Plan and Operations

The following section is dedicated to the organisation of the mission and in particular to the description of the orbit and trajectories chosen to ensure smooth running of scientific activities.

6.1 Journey to Ceres

Considering the fact that Ceres is located in the main asteroid belt between the orbits of Mars and Jupiter and so stand at about 2.768 au (length of its semi-major axis), it is realistically impossible to build a 3U spacecraft that would be capable to flight there on its own. Thus we have to rely on a bigger probe from a more complex and expensive mission to reach our destination. Fortunately, the small size and by extension the limited weight of our cubesat allows it to be easily set as piggyback on bigger spacecraft as it does not require a lot of hardware to do so.

	Ceres Sample Return (CSR) [2]	GAUSS [1]	Calathus [3]
Agency	NASA	ESA ESA + CNSA	ESA
Mission class	New Frontier class	M-class L-class	L-class
Mission design	Sample return (all in one)	Orbiter + Lander Sample Return	Sample Return (Orbiter + Lander)
Launch date	December 2030	April 2037	2031
Mars gravity assist	July 2031	May 2039	10 years mission
Arrival at Ceres	December 2036	August 2040	
Departure from Ceres	September 2038	July 2042	
Earth re-entry	June 2044	December 2023	

Table 6.1: Summary of the 2 ESA and 1 NASA missions to Ceres proposed for the next decade. As the NASA Ceres Sample Return mission seems to be very advanced, keep in mind the two ESA missions seems to be only proposal and have not be investigated deeper for now.

As Ceres has been identified as an intriguing icy world to explore following discoveries made by Dawn (see part 2.2), both NASA and ESA are now developing plans for potential sample return missions in the upcoming decade [2, 3, 1]. Surprisingly, all missions (one NASA mission [2] and two ESA missions [3, 1]) have a similar design and objectives, as they are planned to be launched between 2030 and 2040, and aim to land in areas where carbonates were detected by Dawn in order to collect samples and bring them back to Earth. The main characteristics of each mission can be found in Table 6.1. Considering their sizes, it would be feasible to piggyback on one or the other, without adding additional constraints to our mission design, apart from the launch date. However, NASA's Ceres Sample Return (CSR) mission appears to be more advanced, as it is already among the top candidates for the New Frontiers program for the next few years. On the other hand, the

status of the ESA's GAUSS mission and its selection is currently unclear. For this reason, in the next sections, we will focus on the information available for the NASA mission, while keeping in mind that the same considerations apply to the ESA mission, if it proceeds as planned.

The NASA Ceres Sample Return mission [2] is one of the eight missions proposed under the New Frontier 6 program. It is a medium-class mission that consists of a single element, as showed Figure 6.1, that will land in its entirety on the surface of Ceres to collect samples before re-launching and performing a direct transfer back to earth.

As this mission has been developed to Concept Maturity Level (CML) 4, we have access to the detailed trajectory analyses [2]. Furthermore, as our cubesat weighs only a few kilograms, relative to the nearly 4.7 tonnes of the CSR mission, it is reasonable to assume that the addition of our small spacecraft at the back of the NASA mission should not dramatically affect its boosting capabilities and the total amount of propellant needed.

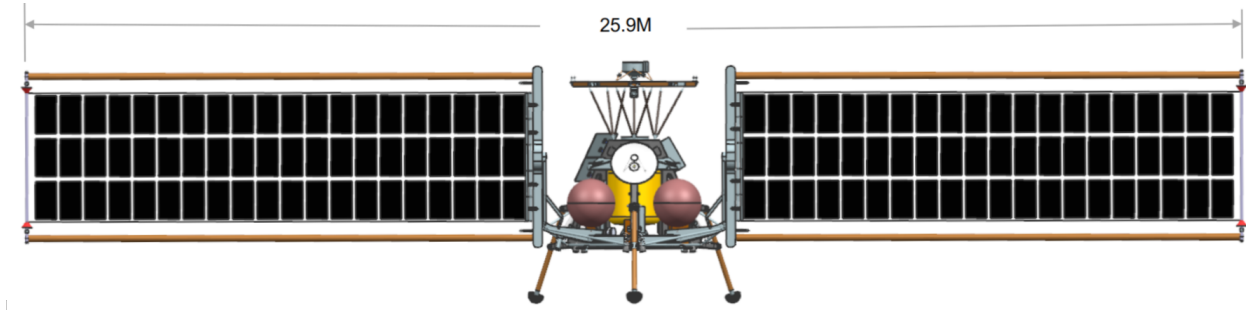


Figure 6.1: The Ceres Sample Return (CSR) SEP-lander spacecraft in cruise configuration from [2]. The total ΔV for the trip to Ceres will be achieved through solar electric propulsion (SEP) powered by solar panels nearly 25 metres long with 68.5 m^2 of active cell area.

The following trajectory analyses are extracted from the Mission Concept Study of an "Exploration of Ceres' Habitability" proposed by J. Castillo-Rogez et al. in 2020 as a planning discussion for the Planetary Science Decadal Survey [2]. The mission would begin in 2030 with the launch of the main probe with our little DIPLONA cubesat attached to it, on a high-performance launch vehicle with a fairing capable of hosting the NASA CSR spacecraft. According to the size of the CSR SEP-lander spacecraft, all analysis were done considering the performance of the Falcon Heavy recoverable launch vehicle which have a 5 meter fairing with an high performance range.

The total ΔV of the CSR mission has been estimated to be around 14 km/s for a sample return round-trip to Ceres. As a monopropellant hydrazine propulsion system is required to land on and take off the spacecraft from the surface of Ceres, a solar propulsion system (SEP) is more adequate as main propulsion solution for the cruise. The electric thruster type and the total solar array size have been determined using low-thrust trajectory analyses. In that respect, the CSR spacecraft is equipped with solar arrays with a total surface area of 68.5 m^2 and two xenon ion thrusters of 600 kg throughput each. This configuration would enable a launch from any year from 2030 through 2037 with very little change in flight time and propellant mass. Overall, the cruise would be about 6 years using the gravity assist around Mars. An example of trajectory for the journey to Ceres for a 2030 launch is presented in Figure 6.2. A shift in the launch date between 2030 and 2037 would not have any impact on the mission trajectory. It would only change the timing of the gravitational assistance around Mars by a few weeks and the total cruise time could be a little bit longer or quicker, but nothing that outcomes the performance of the spacecraft thanks to its SEP propulsion

system.

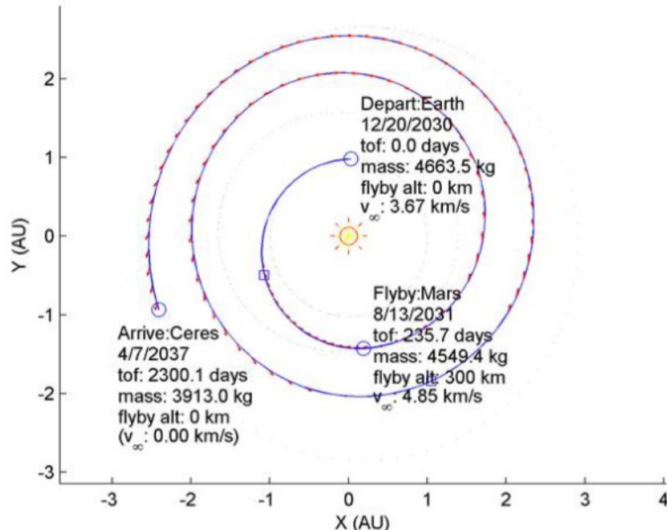


Figure 6.2: Example trajectory of the cruise to Ceres piggybacking on the CSR mission for a launch in December 2030. The gravity assist around Mars would happen 8 month later in August 2031 and the arrival at Ceres' orbit would be in July 2037.

Obviously, as the Diplona spacecraft we are presenting in this report would travel as piggyback on the CSR mission (or maybe the ESA ones if they really happens), the trajectory would be exactly the same. Diplona would remain on standby throughout the journey until entering Ceres' orbit and activate once the CSR spacecraft releases it. Here begins finally its own epic journey.

Once detached from the main probe and after establishing a reasonable safety distance between the two satellites, Diplona set off for a series of tests and checks, in particular concerning the good state of charge of the batteries and all the control system on board.

And then here comes one of the most critical steps of the mission; the deployment of the solar arrays. The four arrays should deploy at a 90° angle to be able to receive as much energy as possible in order to recharge the batteries during the mission. The non-deployment or partial deployment of one of the panels could compromise part of the observations planned during the mission due to lack of energy. In this order, some time will be taken to ensure all panels are well deployed and locked before going further.

Just after that, it's time for its antennas to be deployed too. One pair for the communication with the CSR spacecraft and another one for its payload. The capacity of the spacecraft to exchange properly with the main CSR probe will be extremely important as it's the only way to transfer our data back to Earth. This checkout period has not been clearly assessed as it will also depend on the activities of the CSR vessel but it is assumed that it will not exceed a maximum of a few days. It let the opportunity to take all the time needed for the checkout and to solve any problem their could be.

Now that all systems are ensured to be working and that the spacecraft has its own energy source, it will be time for Diplona to stabilize on its orbit and to start its main task : studying Ceres.

6.2 Orbit constraints: four main targets

In order to determine which orbit would be most suitable for radar profiling of the surface of Ceres, we had to determine which areas were most interesting to study. Indeed, it is technically impossible to carry out profiles of the entire surface of Ceres, as small it may be. Also, even if the surface of Ceres is full of points of interest, whether for their morphology, their chemical composition or their mineralogy, it is important to restrict the number of main targets of the mission in order to privilege the quality over the quantity of observations and to facilitate the calculation of the ideal trajectory.

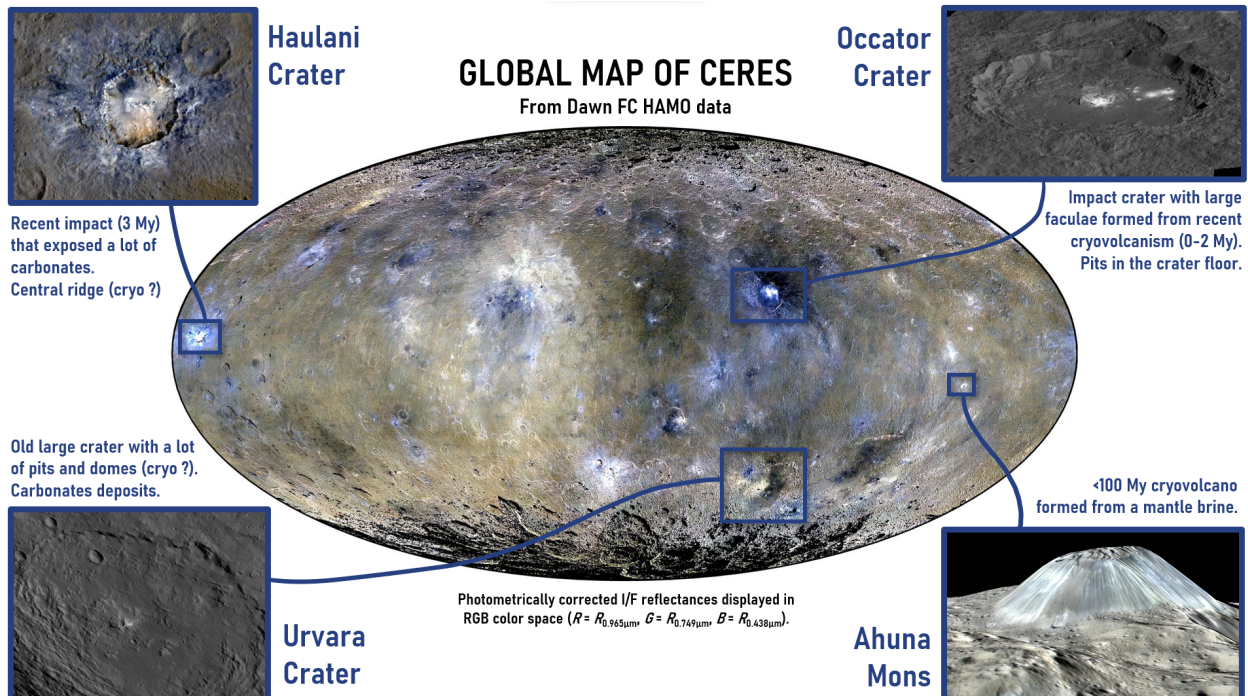


Figure 6.3: The four regions of high scientific interest considered as main targets in this report. The global map of Ceres is based on Dawn FC HAMO data in equal-area “Mollweide” projection. The photometrically corrected I/F reflectances are displayed in RGB color space ($R = R_{0.965\mu\text{m}}$, $G = R_{0.749\mu\text{m}}$, $B = R_{0.438\mu\text{m}}$), showing differences in absolute reflectance and relative differences between color filters. The 4 side images of the targets are from NASA/JPL-Caltech/UCLA/MPS/DLR/IDA.

This is why we have restricted ourselves to four main targets, chosen for their amazing characteristics highlighted by the Dawn mission. A summary of these four specific areas is showed in Figure 6.3, but we will come to the details of each location in the following parts. Among this places, we have three craters: Occator, Haulani and Urvara, and one mountain: Ahuna Mons. All of those places have a interest in the search for extraterrestrial life as they all show traces of cryovolcanism, carbonates, or organic matter [4].

It is also interesting to notice that three of these four locations are also part of the proposed landing and sample collection areas for the CSR mission (Occator crater, Haulani crater and Ahuna mons). The Diploma radar sounder results could therefore be used by the scientific teams of the CSR mission to give structural, and therefore chronological, constraints to the landing site chosen for the sample return in relation to the surrounding units.

6.2.1 Occator Crater

Centered at 19.82°N, 239.33°E within Hanami Planum, Occator crater is a 92 km wide young crater with an age of about 22 My. It features a large number of complex geological structures, the most striking of which are undoubtedly the two faculae (bright spots) at its centre [21, 44], that can be seen Figure 6.4. Those are obviously not the only interesting features at Occator as in addition to the faculae, the floor of the crater shows a lot of domes, different types of lobate structures and 6 different sets of fractures.

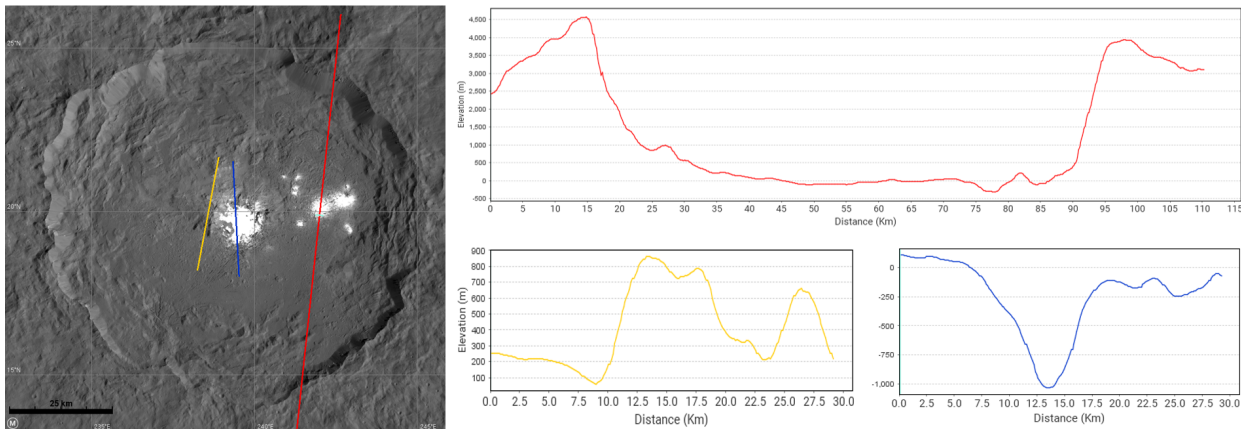


Figure 6.4: Left: Occator crater and its bright faculae, from a high-resolution mosaic from LAMO images. Right: Elevation profiles (from N to S) corresponding to the lines on the mosaic. The red one cross all the eastern side of the crater, and shows that no elevation change is associated to the bright spots of Vinalia Facula. The yellow profile is going through a topographic high ground (tholus) in the direct vicinity of the facula supposed to be made of massif material. The blue profile is going through the Cerealia Facula, showing that it is located in a depression. Radar profiles along those profiles would allow to understand the configuration of the contacts between all these geomorphological units.

The most prominent faculae, located at the center of the crater is called "Cerealia Facula" and the more scattered one, located on the eastern side, is called "Vinalia Faculae" [4]. Those places are well identified in the geologic map presented Figure 6.5. Both areas have an albedo 5 to 10 times higher than the average surface of Ceres. However, Cerealia Faculae shows the highest albedo, in particular at the center of the 10 km wide and 0.9 km deep central depression (see profiles on Figure 6.4). In the center of the pit, Dawn 3.3 m/pixel resolution images revealed a dome that rises 0.4 km above the surrounding terrain. It has been called Cerealia tholus and is assumed to be part of the cryovolcanism features. The smaller size bright spots of Vinalia Facula also shows some domes at their center, but of a much lower altitude.

Spectral analyses indicate that the bright material of the faculae is dominated by sodium carbonate and ammonium chloride [44]. That is consistent with remnants of brines sourced in the subsurface that lost their liquid water component on Ceres' surface. Hydrous sodium chloride (hydrohalite) has also been observed on top of Cerealia Tholus. As it is very unstable when exposed to space (dehydration timescales of a tens of years at Ceres' surface conditions), it suggests recent deposition and thus a recent cryovolcanic activity. This would imply that at least some brines may still be present in the subsurface.

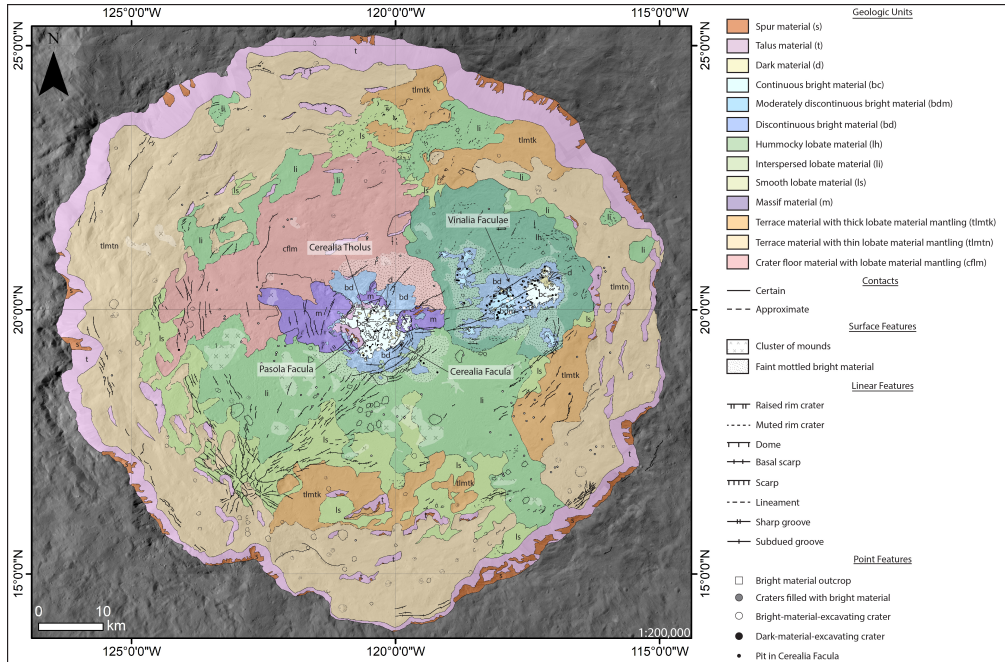


Figure 6.5: Occator Crater geologic map from [11] on the LAMO mosaic (25 m/px) basemap at a scale of 1:200,000 and with a simple cylindrical projection. It is interesting to notice the bluish areas which correspond to the bright faculae, the black lines corresponding to fractures, pits and grooves, and the brighter crossed areas showing clusters of mounts and domes.

Apart from the bright materials of the faculae, and as mapped on the geological map in Figure 6.5, the floor of the crater is mostly covered by different types of lobate and mantling materials [44]. The thicker of those materials are thought to represent melt sheet deposited directly after the impact 22 My ago, as the origin and age of the thinner mantling ones is more complicated to assess.

We expect that the resolution of the Diplona radar sounder will be good enough to identify the base of the biggest landslides. So we should be able to understand the chronology of all those deposits and reconstruct the history of the crater materials. Understanding their geometries and their dispositions underground would also put a lot of constraints on the rheology of the materials composing Occator Crater, such as their porosity and ice content.

Moreover, a lot of fractures, pits and grooves can be observed around the faculae and in different other locations in Occator crater [45, 46]. Considering their location and direction, they can be classified in six different sets. Three of these fracture systems: concentric features outside the crater, at the terrace and at the western floor, have been interpreted to be formed during the cratering process. Nevertheless, the other three sets of fractures are supposed to be linked to the cryovolcanic activity and the formation of the faculae. It is thus really important to understand the geological history behind these fractures as it could tell us a lot about cryovolcanism processes that happens at Occator crater.

To put it all in a nutshell, the various features of Occator crater, relating to the active geological history of this area, are making it a really interesting place to investigate with Diplona' radar sounder. The origin of the recent cryovolcanism in Occator crater are still in debate and the chronology for the deposition of all the different units is still very unclear. The diversity of the features observed is the reason why Occator crater is our first main target. Using DRS, we expect to add a

new dimension to Dawn images by adding a vertical component to the structures discussed above. As our spacecraft will be able to fly many times above Occator with slightly different directions, we expect the profiles to be good enough to allow a 3D interpretation of the geological structures. How thick are the faculae? What kind of underground structures are there under the domes? Are we able to identify the number and size of the brines? These are all the questions we expect to answer in Occator crater, keeping in mind that those kind of processes are expected to happen on many icy-bodies in the solar system.

6.2.2 Ahuna Mons

Consisting in an isolated mountain centered at 10.3°S , 316.2°E as shown in Figure 6.6, Ahuna Mons rises nearly 4km above the surroundings. As topographic rises broader than Ahuna Mons are common on Ceres' surface, it is the only mountain with such distinct shape, size and morphology [12].

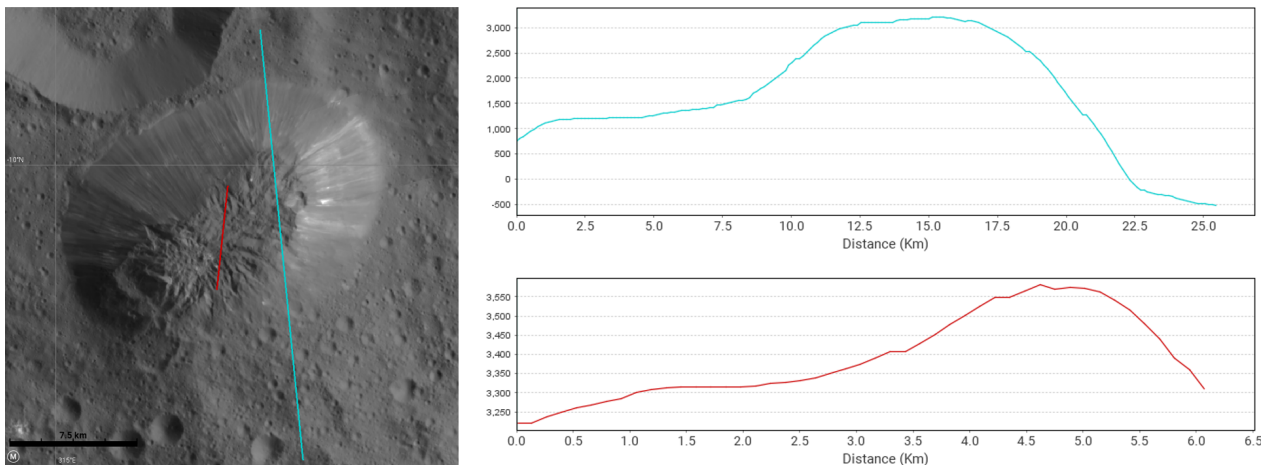


Figure 6.6: Left: Ahuna Mons, a possible cryovolcanic dome, from a high-resolution mosaic from LAMO images. **Right:** Elevation profiles corresponding to the lines on the mosaic.

Indeed, Ahuna Mons is made of steep flanks (30 to 40°) of slope debris material and a rough summit unit slightly depressed, as it can be seen on the profiles Figure 6.6. The base of the talus leaves a very sharp contact between the slope and the surrounding smooth unit, which is very unusual. This means that very little debris has accumulated at the bottom of the slope, despite the fact that downslope lineations are visible on all the flanks likely caused by gravitational processes such as rock falls.

The summit of Ahuna Mons does not show debris evidence but displays a large variety of geomorphological structures [12]. Pits, hills and ridges are present all over the summit as shown on the geologic map Figure 6.7. Hence, the summit material have probably been affected by extensional forces, explosion or sublimation events, tilting or extrusion of a new material.

Spectroscopic analysis of reflectance spectra have been made on Ahuna Mons region using Dawn/VIR data [12, 47]. With respect to a series of spectral features (absorption band centers and depth, and spectral slopes), Ahuna Mons has been described as a spectrally clearly distinct unit from the surrounding regions.

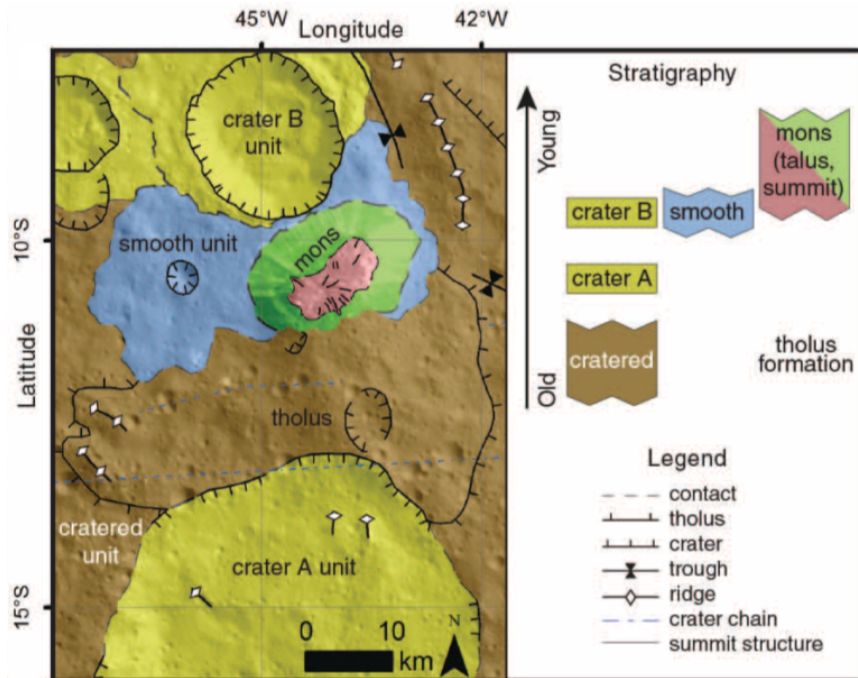


Figure 6.7: Geological map of the Ahuna Mons region derived from Dawn data, with colors corresponding to units shown in the stratigraphic column, from [12]. Note the younger smooth unit surrounding Ahuna Mons and the ridges on summit unit.

The overall composition of Ahuna is not too different of the global composition of Ceres' surface (see part 2.2.1) with the detection of hydrous minerals, NH₄-phyllosilicates and carbonates [47]. However, at its local scale, Ahuna Mons appears to show a lower abundance of hydrous mineral phases and a greater abundance of Na-carbonates than the surroundings areas observed at the same spatial resolution. As it can be seen on Figure 2.6, the composition of Ahuna is not uniform as its flanks seems to be brighter. Moreover, spectral analysis shows that northern flanks appears to be richer in carbonates.

By comparing with the faculae in Occator Crater, and using a spectral unmixing model, it has been demonstrated that Ahuna Mons is a really a peculiar structure with respect to its composition. The brightest regions, associated with coarser grain size suggest a recent hydrothermal activity which would locally expose fresh subsurface material richer in carbonates.

The stratigraphic relations of Ahuna Mons region morphological units, the aspect ratio, and the geological features points to a dome formed mostly through extrusion. As the summit unit shows nonsystematic orientated ridges and pits, it suggests a dome formation in multiple phases of fracturing and small-scale extrusion. This is similar to high-viscosity volcanic domes on Earth which also shows such type of features related to a multi-phase evolution of the summit [12]. Moreover, it is supposed that the summit unit represents a brittle dome carapace, formed by cooling of the outermost layers of a ductile dome. When fracturing, this carapace disintegrates and products boulders and smaller debris that may have formed the lineations on the flanks.

To resume, aspect ratio and summit morphologies indicates that Ahuna Mons is an extrusive cryo-volcanic dome with a ductile core that as a relatively high viscosity. Furthermore, the uniqueness of this feature at the surface of Ceres' is probably due to the young age of Ahuna Mons, that as been

estimated at between 210 and 70 Ma [12] by counting the craters. Indeed, using numerical models [47], it has been showed that flowing rates shall lead to an extensive relaxation of cryovolcanic structures over $10^8 - 10^9$ years, but gradual enough for Ahuna Mons to remain identifiable today. That is why most cryovolcanic features at Ceres' surface are more ambiguous to identify, but it is reasonable to suggest that many tholus, as the one observed around Ahuna, may represent older relaxed cryovolcanic structures today mostly unrecognizable.

Even if Ahuna Mons is a small area, its very young age, its uniqueness on the surface of Ceres, and its great geomorphological complexity, make this object a major enigma that should be explored with DRS to uncover the mysteries of Ceres' vanished cryovolcanoes. We expect to add a new dimension to the data we already have on Ahuna by adding a depth component in our observations. We hope to obtain subsurface profiles of the summit unit that would maybe be good enough to identify different cryovolcanic events and that would thus allows a reconstruction of the building history of this edifice. Moreover, by observing the contact at the base between the slope and the surrounding unit, we expect to be able to identify if the dome continue in depth and what is the nature of the contact with the surrounding unit (that has been supposed to be a relaxed older cryodome). Therefore, Diplona's Radar sounder promises to give interesting results in this region which, it is hoped, will make it possible to bring constraints on the processes of cryovolcanism on the surface of Ceres.

6.2.3 Haulani Crater

Centered at 5.8°N , 10.8°E , Haulani Crater is one of the youngest features on Ceres. Moreover, it is also one of the brightest points at Ceres surface and thus was already identified in Hubble Space Telescope (HST) images in 2006 [48]. As all other features on Ceres, it has then been studied by Dawn spacecraft with a much higher resolution. Those new images allowed the mapping of Haulani morphology using the correlation between visible and IR data [13]. The resulting geomorphological map is available Figure 6.9 and will be discussed hereafter.

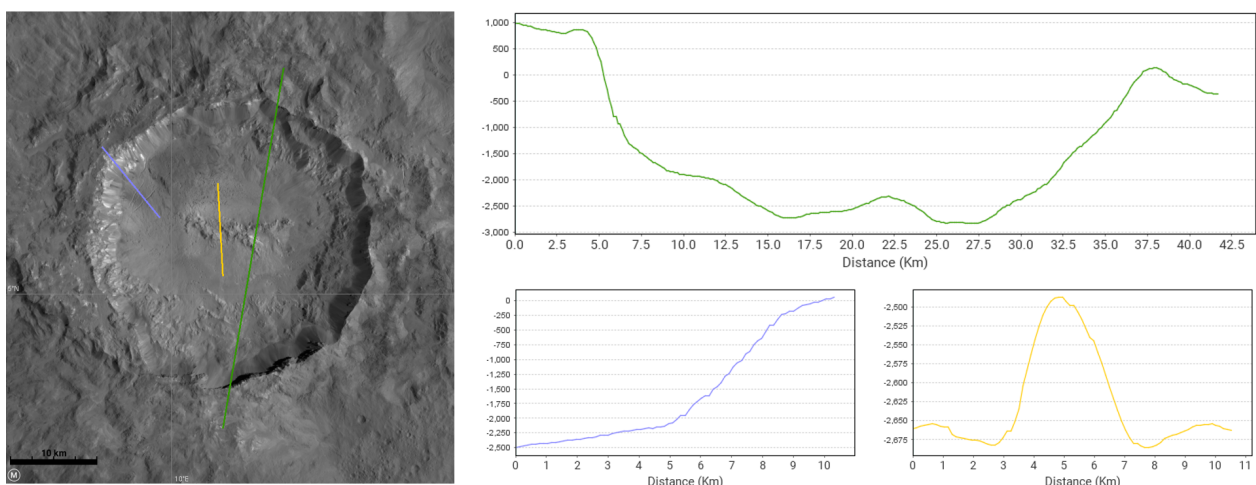


Figure 6.8: Left: Haulani crater, with possible cryo-domes in the center and a few pits around it in the carbonates deposits, from a high-resolution mosaic from LAMO images. **Right:** Elevation profiles corresponding to the lines on the mosaic.

Haulani is a small impact crater compared to Occator or Urvara (that will be described in the next part) as its diameter is only around 34 km. However, its bright extensive ejecta is widespread over the cerean surface with far-ranging crater rays of about 160 km to 490 km, preferentially to the west, as it can be seen on the LAMO mosaic on Figure 6.8.

The crater was formed on the transition between a cratered plateau in the east and a topographic low in the west. As visible in Figure 6.8, it displays a sharp rim in almost all directions except at the southeastern outer crater rim where a steep slope resulting in a depression within the flank of Haulani indicates a failure of the rim. Furthermore, the western rim appears to be mostly collapsed showing a lot of scarps and fractures, also due to the failure of the rim material.

The floor of Haulani crater is mostly made of an overall smooth bright material showing flow features, and some cracks and fractures in northeastern part, parallel to the crater rim. As showed by the blue profile on Figure 6.8, those cracks are currently too small to be visible on the topography but we expect them to be large enough to see them with Diplona' Radar Sounder. In the mid-northern part of the crater floor and extending to the west and the mid-southwestern and mid-southeastern part (see the geological map on Figure 6.9), a pitted terrain has been observed. The pits have no raised rims and appears to concentrate in clusters. One hypothesis for their formation could be the degassing of volatile-bearing material heated by the impact.

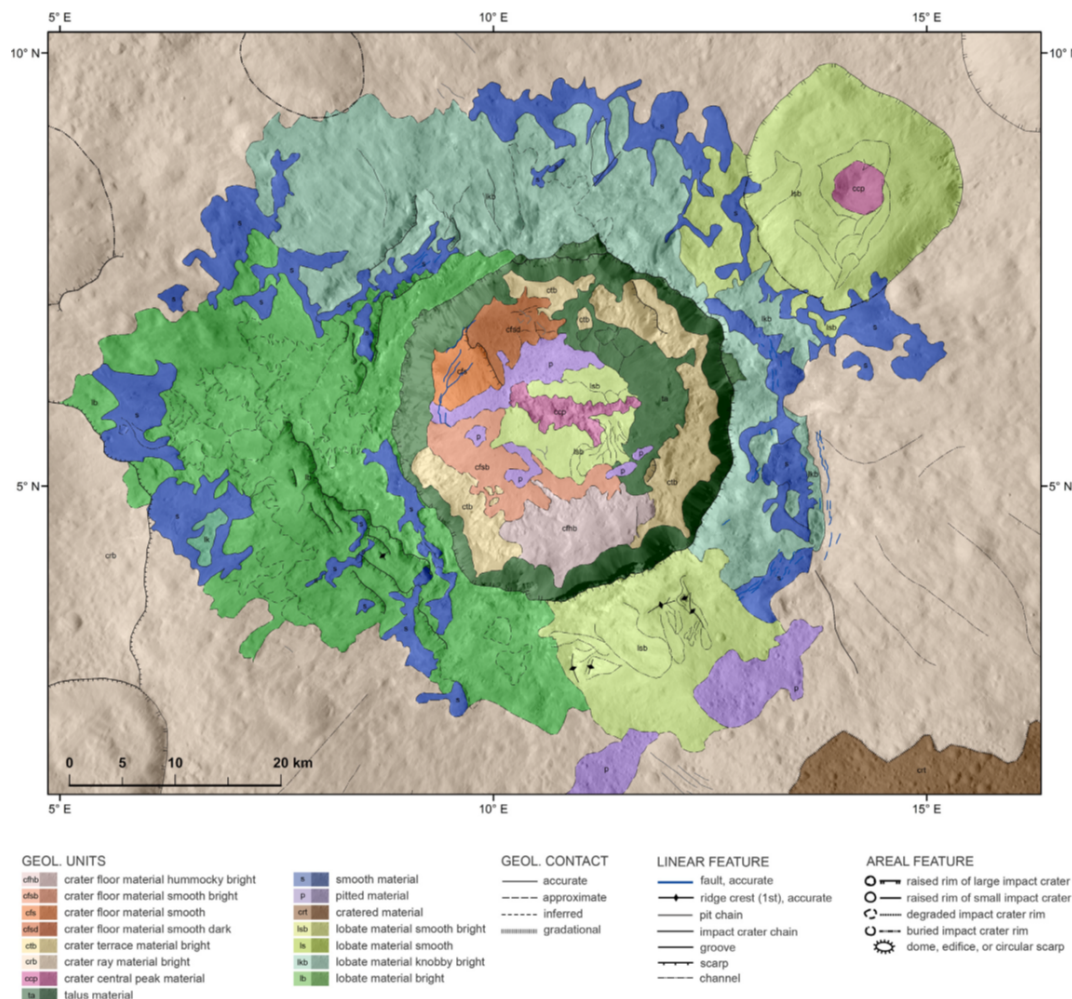


Figure 6.9: Detailed geologic map of Haulani crater and surroundings illustrating the tectonic and geological history from [13].

On the other hand, the center of the crater is occupied by a hummocky elongated mountainous ridge of a maximum length of around 22 km and rising up to 300 m above the crater floor, as showed by the yellow profile on Figure 6.9. This type of central ridge is not unique and has been observed in most of the craters punctuating Ceres' surface, but the ridge of Haulani crater is one of the most erosion- and infill-preserved, due to its very recent age.

The flanks of Haulani crater are also interesting as they exhibit three different type of lobate material. Multiples bright lobate flows can mostly be seen on the western side, flowing around blocks to the lower elevation area. These smooth flows are interpreted as a mixture of impact melt and cryovolcanism flows and may be really interesting to study with DRS to put more constrains on their thickness and rheology.

Haulani's high albedo, blue spectral slope and well preserved morphological features all appear to be indicators of youth. Measurements made in the proximity of crater Haulani by counting smaller craters superimposed on Haulani ejecta blanket have shown that Haulani formation age should be comprised between 1.7 and 5.9 Myr [49]. This very young age is a great opportunity to study the composition of the ejecta because they may not have had time to be altered.

Thus, the region of crater Haulani has been investigated with an emphasis on mineralogy using Dawn VIR data using many spectral indices (as for Ahuna) and a surface temperature map [49] to obtain an in-depth description of the chemico-physical state of Haulani surface. As previously mentioned, crater Haulani and its ejecta exhibit a peculiar "blue" visible to near-infrared spectral slope. This unique feature support its young age as it is not observed elsewhere on Ceres. This could be the result of the rapid desiccation of a slurry mixture of water, phyllosilicates, and carbonates, forming a smooth material. It has also been showed that Haulani's floor and ejecta are depleted in magnesium- and ammonium-bearing phyllosilicates but shows localized patch of sodium- or calcium-bearing carbonates. Those carbonates are quite rare on Ceres and may be indicative of hydrothermal processes triggered by the impact. Moreover, the small amount of hydrous natrite detected indicates that the deshydratation process following the impact is still at work, again supporting the young age of Haulani. And last but not least, it is supposed that the actual composition of Haulani is mostly driven by the preimpact composition of the target in its shallow subsurface (in particular, the abundance of hydrated or icy compounds and carbonates).

To conclude with Haulani, it is clear that this target represent a major interest in understanding the processes following an impact crater. The very young age of Haulani allows to access the early history of the materials and structures short after the impact. With Diplona, we expect to understand the set up of the different mineralogical units, and maybe to deduce their organisation in Ceres' crust before the impact. Moreover, the characteristics of the different units in the radargrams could also tell us a lot about their physical properties.

6.2.4 Urvara Crater

While the choice of the previous primary targets was fairly obvious due to their unique characteristics on cerean surface, the selection of our the fourth objective was more ambiguous as many candidates were possible. Yet Urvara was considered as the most interesting one, being one of the largest impact structure on Ceres and thus showing a very high diversity of morphologies.

Urvara basin is as around 170 km wide and is centered at 65.66°S, 249.24°E, at an average altitude

of -6100m below the reference ellipsoid, thus being one of the lowest-lying surface area on Ceres [50]. The morphology of Urvara, as presented on Figure 6.10, is consistent with a medium-aged complex impact crater, indicated by well defined continuous crater wall with terraces caused by post-impact faulting and slumping inward the basin, and by a mountainous ridge at the center.

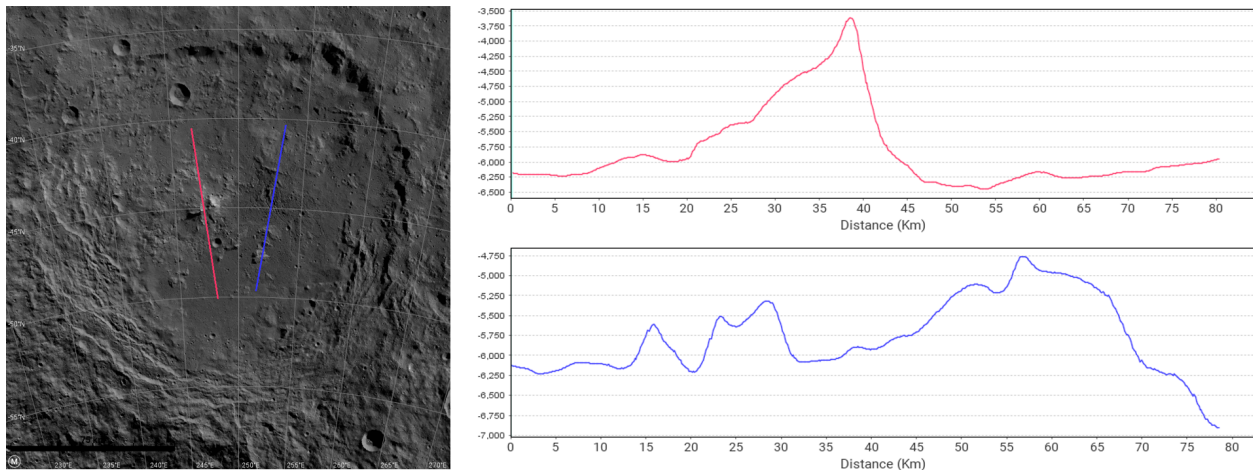


Figure 6.10: Left: Urvara crater, with a very irregular floor with the presence of carbonates deposits , ammoniated phyllosilicates and salts and a possible cryo-dome in the center, from a high-resolution mosaic from LAMO images. Right: Elevation profiles corresponding to the lines on the mosaic.

The rims of Urvara basin show two different morphologies [14]: a steep single scarp in the north and eastern side, and a terraced wall on the southern and western side, as shown on the geological map Figure 6.11. They also show a noticeable height variation being higher in the north-east and declining gradually towards the east. This is consistent with the fact that Urvara formed at the transition between a smoother zone in the north and a rougher area, due to higher latitudes, in the south.

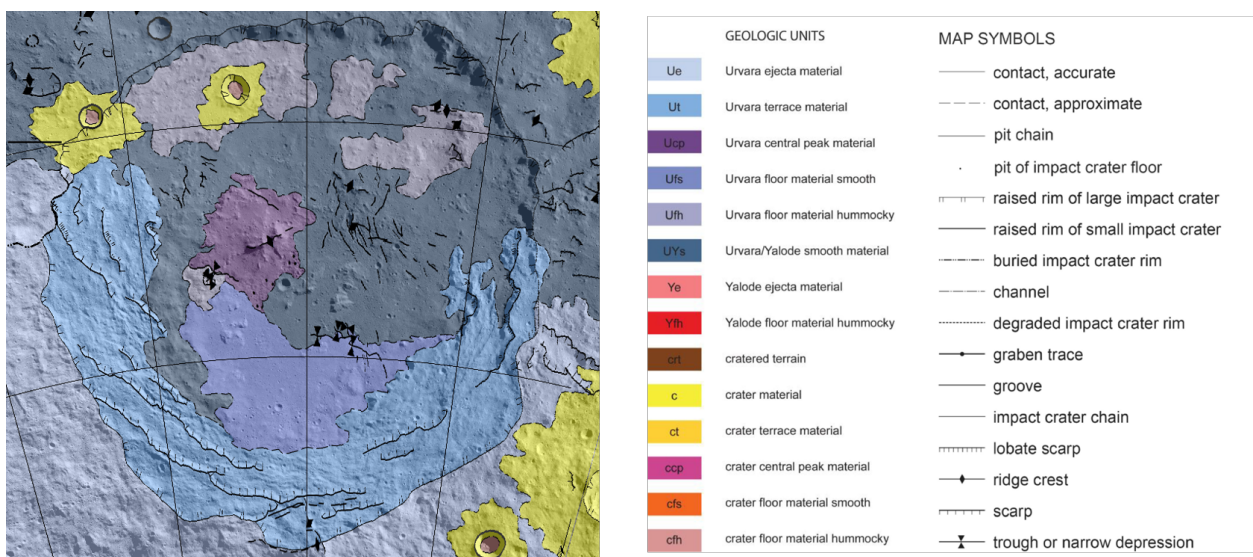


Figure 6.11: Urvara Bassin geologic map on the LAMO mosaic (25 m/px) basemap, from [14]. It is interesting to notice the smooth material unit blanketing the older crater floor and terrace units. See also the central ridge and the grooves and pits in the basin floor.

As mentioned before, a central ridge rising up to 3 km above the crater floor stand a little bit off-center in the basin, located at the limit between the southern and northern floor of the basin, which is marked by a topographic step. The profile of the ridge can be seen on Figure 6.10. The ridge is characterized by a very steep southern flank with average slopes up to 75%, exposing cliffs of bedrock and talus with numerous boulders tumbled down the talus slope. The presence of an alternation of cliffs, boulders and slopes indicates an heterogeneous composition.

Moreover, eastward of the central ridge, a central pit around 20km wide and 0.6 km deep as been observed [14]. Central pits are pretty rare on Ceres and are formed in a volatile-rich crust via the collapse of the central peak due to the gradual release of impact-induced volatiles or the drainage of impact melt. Thus, it is consistent with the presence of water ice and the potential presence of brines in the subsurface. More pitted terrain has also been observed south to the central ridge.

When not occupied by the terraces, most of the crater floor is recover by a younger unit of smooth material (see on Figure 6.11 in grey). The origin of this unit it yet not well understood, but it is important since this is one of the major geologic units on Ceres. When looking at the stratigraphy, it is clear that the smooth unit appears to blanket older floor units and terraces. Furthermore, a lot of chaotic elevations can be found in Urvara basin, as shown on the lower profile 6.10, but their origin is also not clear. Some are thinking it could be related to buried crater formed by flow fronts of solidifying impact slurries, and other are proposing that it could be related to cryovolcanism. Any-way, whatever their origin, it is interesting to note that the areas of smooth material or even of older crater floor are strewn with fractures and grooves. It could be due to post-impact horizontal and vertical movements and thus could suggest late floor activity, possibly caused by cryovolcanism, late outgassing or/and severe mass wasting [14].

Although the geomorphology of Urvara is complex, the composition of the basin is no less interesting. Indeed, Urvara is showing a distinctive spectral diversity, much greater than the neighbouring region, and several colour units can be distinguished [50, 51].

Bright material, associated with salts, has been detected at the central ridge of Urvara. It shows high reflectance, with the brightest point being located on a cliff at the north-east central ridge. As their colour spectral is similar to the average cerean surface, and despite having a comparable reflectance of Occator spectra, they differ from those of the faculae, thus indicating a different salt composition. Also, more exposures of this material, of a smaller size, are located in the crater rims, exposed by slumping.

Furthermore, a small site of around 0.25 km² located on the western floor displays a more overall red-slopped spectrum, being highly different from all other bright materials in Urvara. It shows a colour spectrum similar to those of organic-rich material as found around Ernutet crater, and its IR spectrum deviate significantly from that of Cerealia Tholus thus indicating a different composition. Other points of reddish material have been discovered, all showing the same signatures that can be associated with organic matter. Thus it may be possible that the distribution of organics on Urvara scarps would be wider.

Lastly, it is also important to notice that the western side of Urvara basin is one of the only places over Ceres showing strong carbonate absorptions that have band centers at 3.95 μm , consistent with Mg-carbonates [51, 4]. This observation does not correlate with the morphology so it is unclear how the carbonates were formed in Urvara. Moreover, the central ridge appears to be enriched in ammoniated phyllosilicates, which is consistent with the hypothesis of the impact excavating material from a depth of around 50 km that would then form the central ridge.

To conclude about Urvara, we see that a lot of questions are still unanswered and that a lot of morphological and mineralogical features are still unclear. What is the origin of the bright materials? Are they related to the exacted material due to the impact and have been preserved until now? Are they due to recent cryovolcanism? What is the origin of the smooth material? Inferring a part or all of those questions would tell us a lot about Ceres crust structure, as Urvara impact allows us to access materials that were deeply buried in the crust before. It would also allow us to learn a lot about the processes happening on Ceres surfaces and how the landscapes evolves. Using Diploma' radar, we hope to understand how each unit is organised, to locate brines if they are shallow enough, and to assess if chaotic landforms and grooves are due to cryovolcanism of other processes.

6.3 Orbit determination

To be able to explore the four main targets presented previously (see Figure 6.3 for the resume), we had to choose the proper orbital trajectory. As the four places of interest are really dispersed over the entire surface of Ceres, with high differences in their latitudes (from 19.82°N for Occator Crater to 65.66°S for Urvara Crater), a near-polar orbit was retained as the most adequate option by its particularity to be able to scan almost all the surface.

The goal of our mission is to be able to analyze the craters as much as possible to have reliable data. Each area will be flown over at least ten times by the satellite but for power concerns, some passages will not be welded by the radar. The near-polar orbit was chosen for this purpose. Moreover, a circular orbit will be largely desirable for the mission in order to have similar conditions of measurement that's why the eccentricity is equal to zero. You will have below a model of our orbit compared to the orbit of the main satellite of the mission. We observe that ours will have a much lower altitude in order to be as close as possible to Ceres. Nevertheless, this poses some concerns, especially for the longevity of the mission and the time hidden behind Ceres compared to the time of sunshine. For a mission like ours, this data is extremely important, especially because of the distance of Ceres from the Sun and the limited size of our satellite. This will lead to a study of the flight phases which will be importance at the risk of running out of battery. Which is not desirable. This study will be treated after.

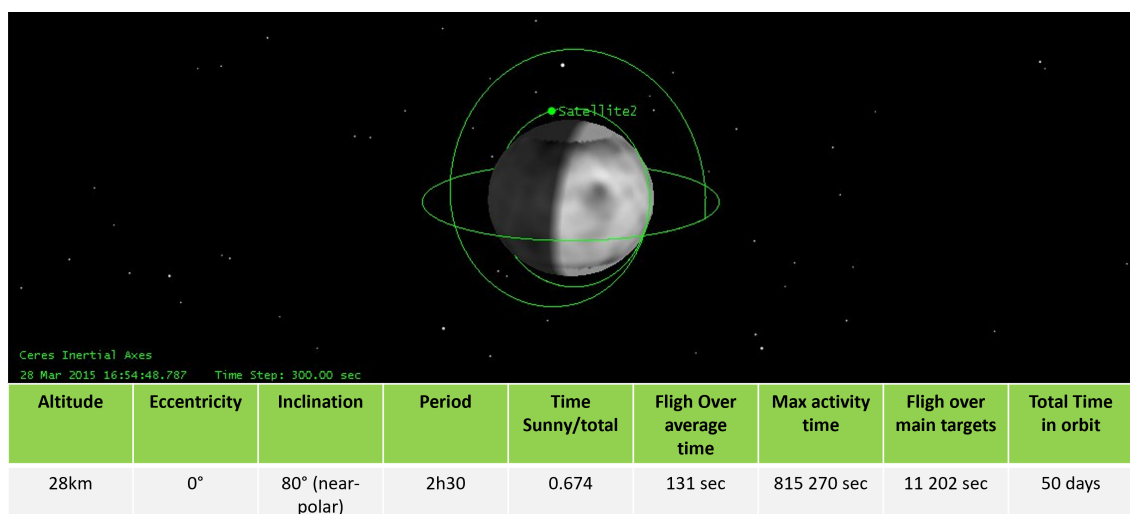


Figure 6.12: STK Orbit Simulation, main specificities.

Coming back to our orbit, given the small size of Ceres and our low altitude, the period is quite fast: 2h30 to make a complete orbit. This will allow us to be able to efficiently cover all our targets in a short amount of time. But this also means that we will have a very short time of action, only 131 seconds on average over a target. This will important preparation for the satellite to be ready in time. (see 6.12)

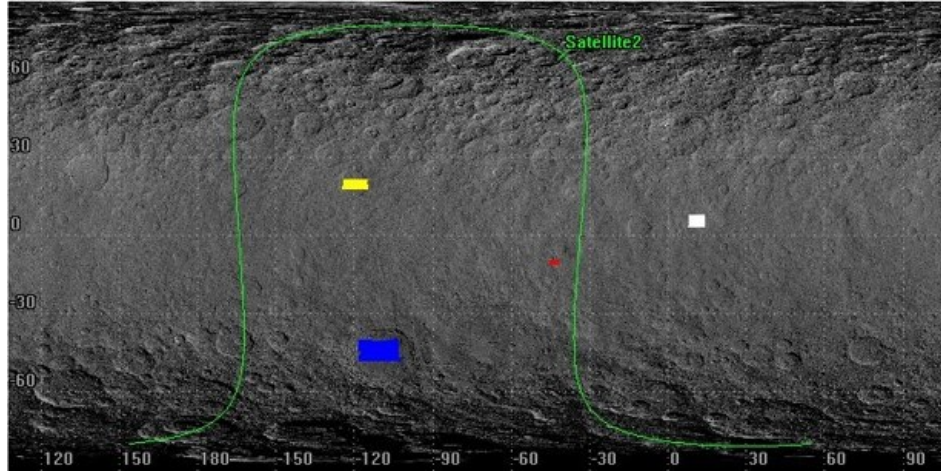


Figure 6.13: STK, one example of satellite's ground track with our near-polar orbit. Each colored rectangle correspond to a main target. Yellow for Occator, red of Ahuna, blue for Urvara and white for Haulani.

Finally, the total target mission time is 50 days. This time was calculated as the time necessary to probe effectively all our target craters giving a time of overflight of our main targets of 11 202 sec (187min). Without forgetting that during these 50 days, the transmission of the data will also have to be carried out. The success of the mission will thus be strongly related to our control of action and recharge phases. And for that, we must take into account the frequency of overflights over each crater. You can have an example of one orbit in the figure 6.13.

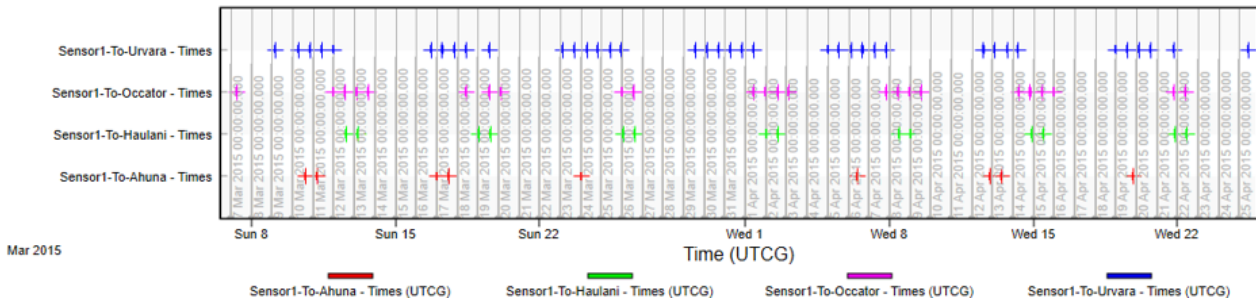


Figure 6.14: STK, flight over frequency for each of the four main targets. Every cross correspond to one fight over. The bigger is the target, the more flight over they are.

We observe that we won't have so much flight over Ahuna and Haulani. This is due to their proximity to Ceres's equator. They will therefore be our priority targets for the planning of the radar probe. We will be able to allow a greater flexibility for Occator and Urvara with flybys without data taking to save energy. You will find below the totality of the ground traces of the overflights of our satellite above the targets. These overflights will be more than enough to have data covering the whole surface of the craters.

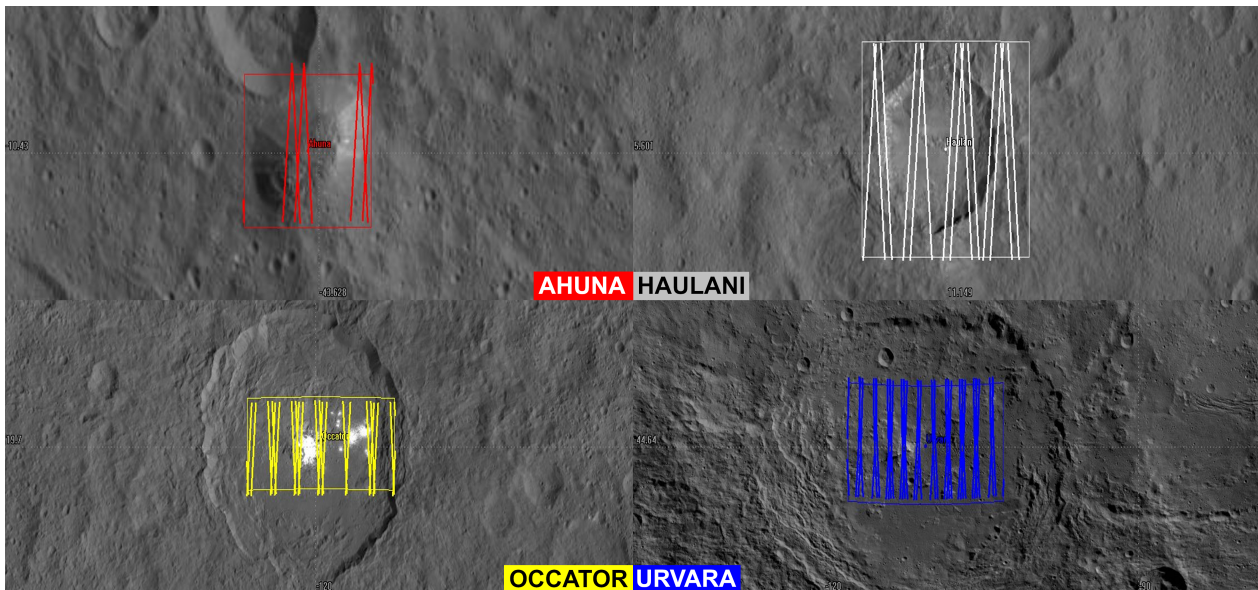


Figure 6.15: STK, Ground Tracks on each target for a 50 days orbit simulation.

6.4 More than 60 possible secondary targets

The trajectory of the spacecraft, discussed herebefore, was calculated by aiming only at the four main targets, but neglecting the possibility of observing other objects on the surface of Ceres would be a mistake. To use our Diplona spacecraft at its maximum capacity, so taking advantage of all the time available in orbit for our observations and maximize the scientific yield of our instrument, we had to prepare other possible targets to observe.

Those places will be considered as secondary targets, as they will only be observed during the mission if the spacecraft has enough power, storage (or any other limited parameter) to ensure the right observation of our four main targets: Occator, Ahuna, Haulani and Urvara. However, it is good to already have a bank of potential secondary targets to explore if the status of the spacecraft allows it.

Hereafter we propose a first non-exhaustive list of secondary targets that may be interesting to explore, on Table 6.2. For each area we report where the feature is centered, what type of object it is, and how big it is. The most important objects may probably be the ones related to cryo-volcanism like tholus or cryodomes, but that would be to ignore structures too often forgotten on the surface of Ceres that are related to tectonic activities: fossae, fractures and catenae [52]. Also most of the objects proposed in this list are landslides and were taken from the list presented in [9]. They are considered as so important because understanding their morphology and their distribution could tell us a lot about physical properties of the material constituting Ceres' crust. Please remember that this list is not definitive and that many other spots may be interesting to study with DRS. That is why scientists from all over the world will have the opportunity to propose secondary targets to explore, thus enriching the possibilities of discovery of Diplona mission. This proposing phase could probably happen during the cruise, or may also be necessary if the mission is extended in phase F.

Area name	Position of the center	Type	Characteristic size
Oxo Crater	41.281°N, 356.656°E	Bright material exposure	10km
Ernutet 1	55.676°N, 39.927°E	Carbonate Deposits	50km
Ernutet 2	50.535°N, 39.924°E	Carbonate Deposits	20km
Nawish Crater	17.95°N, 193.298°E	Central pit	80km
Liberalia Mons	6.379°N, 311.074°E	Cryo-Dome	20km
Nabanna Fossa 1	5.717°N, 290.014°E	Fossa	250km
Nabanna Fossa 2	2.438°N, 283.625°E	Fossa	200km
Nar Sulcus	-42.289°N, 280.485°E	Fractures	70km
Makahiki Labyrinthus	18.913°N, 237.642°E	Fractures	40km
Samhain Catenae 1	-10.454°N, 263.12°E	Pit Chain / Catenae	250km
Samhain Catenae 2	0.446°N, 246.444°E	Pit Chain / Catenae	80km
Samhain Catenae 3	-5.912°N, 267.904°E	Pit Chain / Catenae	300km
Samhan Catena	-23.553°N, 222.411°E	Pit Chain / Catenae	200km
No Known Name	-17.541°N, 51.435°E	Pit Chain / Fractures	65km
Azacca Pits	-6.239°N, 218.864°E	Pits / Fractures	300km
Dantu Pits	23.348°N, 137.532°E	Pits / Fractures	100km
Ikapati Pits	33.093°N, 45.697°E	Pits / Fractures	20km
IM008	61.779°N, 51.902°E	T1 Landslide	10km
IM015	32.266°N, 47.785°E	T1 Landslide	10km
IM016	-6.489°N, 116.226°E	T1 Landslide	15km
IM023	-35.243°N, 168.164°E	T1 Landslide	10km
IM041	62.584°N, 249.703°E	T1 Landslide	20km
IM053	-0.114°N, 252.428°E	T1 Landslide	<10km
IM071	29.77°N, 0.3°E	T1 Landslide	20km
IM086	-23.267°N, 57.584°E	T1 Landslide	10km
IM090	23.8°N, 18.989°E	T1 Landslide	25km
IM098	31.326°N, 290.01°E	T1 Landslide	<10km
IM113	-7.525°N, 220.798°E	T1 Landslide	10km
IM009	58.232°N, 56.553°E	T1/T2 Landslide	15km
IM032	45.643°N, 284.027°E	T1/T2 Landslide	10km
IM035	51.154°N, 315.752°E	T1/T2 Landslide	10km
IM036	35.174°N, 304.717°E	T1/T2 Landslide	15km
IM052	29.971°N, 269.092°E	T1/T2 Landslide	20km
IM072	-47.713°N, 359.803°E	T1/T2 Landslide	<10km
IM085	7.149°N, 149.598°E	T1/T2 Landslide	25km
IM108	-34.163°N, 91.136°E	T1/T2 Landslide	10km
IM109	54.551°N, 94.224°E	T1/T2 Landslide	20km
IM043	18.601°N, 234.206°E	T1/T3 Landslide	15km
IM061	4.99°N, 238.108°E	T1/T3 Landslide	<10km
IM062	3.588°N, 236.021°E	T1/T3 Landslide	<10km
IM002	34.497°N, 37.679°E	T2 Landslide	10km
IM013	27.068°N, 14.975°E	T2 Landslide	15km
IM014	35.14°N, 48.349°E	T2 Landslide	15km
IM021	-38.092°N, 172.509°E	T2 Landslide	15km
IM033	12.773°N, 335.451°E	T2 Landslide	15km
IM038	26.901°N, 299.448°E	T2 Landslide	<10km
IM055	64.894°N, 280.721°E	T2 Landslide	25km

IM059	5.168°N, 241.146°E	T2 Landslide	10km
IM087	-43.003°N, 45.928°E	T2 Landslide	10km
IM092	-38.838°N, 265.738°E	T2 Landslide	<10km
IM095	-40.611°N, 264.402°E	T2 Landslide	15km
IM103	-44.256°N, 152.718°E	T2 Landslide	20km
IM115	58.449°N, 262.526°E	T2 Landslide	40km
IM058	12.662°N, 243.781°E	T2/T3 Landslide	20km
IM099	-37.263°N, 177.473°E	T2/T3 Landslide	20km
IM100	-38.489°N, 177.437°E	T2/T3 Landslide	20km
IM114	-35.139°N, 265.281°E	T2/T3 Landslide	35km
IM112	-54.853°N, 274.79°E	T3 Landslide	35km
Kwanzaa Mons	32.848°N, 326.666°E	Tholus / Cryo-Dome	40km
Hosil Tholus	43.467°N, 320.54°E	Tholus / Cryo-Dome	35km
Mikeli Tholus	38.429°N, 293.386°E	Tholus / Cryo-Dome	45km
Cosecha Tholus	43.01°N, 9.874°E	Tholus / Cryo-Dome	30km
Dalien Tholus	3.775°N, 5.152°E	Tholus / Cryo-Dome	25km
Wangala Tholus	-22.156°N, 5.617°E	Tholus / Cryo-Dome	60km

Table 6.2: Non-exhaustive list of possible secondary targets, classified by the feature type. IMxx landslides are taken from the list of [9]. Type 1 landslides are exhibit lobate, tongue-shaped morphology, with a well-defined toe. Type 2 landslides have a thin, sheet-like structure, distinctive toe, and long run-out length. Type 3 landslides are cuspat and sheeted, characteristic of fluidized appearing ejecta.

6.5 Final instrument phases

During the life of our satellite, it will be put through multiple different modes, each one with its specificity's, some modes will be used to save power, to analyse every parameters on board or to use the radar. Each one of this modes uses specific components of the satellite at certain point of the mission. The OBC and the battery are the only components that will be ON from the minute the satellite is being ejected from the piggyback. The OBC is the brain that will command and decide which mode will be activated to serve the mission, he will be able to receive instruction that will transit by the NASA orbiter.

In the first place, we will explain in detail which component is going to be used by each mode and every information will be resumed on 6.16. We will then present you the relation in between modes and present the flight program on a the diagram 6.17.

6.5.1 Flight modes

6.5.1.1 Mode OFF

This mode should and will only be used during the transportation phase. During the time where the satellite will be piggybacking every component including the OBC and the battery will turned off. During this time, the components will be protected by the ejection pod.

6.5.1.2 Idle mode

During the ejection, the satellite should automatically switch to an idle mode. This mode allows the OBC and the battery to be on. The goal is to slowly start checking that every piece of equipment is undamaged from the launch, the transport or the ejection. The ADCS system is off and the satellite isn't controlling its movement. The idle mode is the most energy economic mode.

6.5.1.3 De-tumbling Mode

The de-tumbling mode is the mode responsible for the satellite positioning. The goal is to stabilize the rotation and the trajectory. During the first detumbling mode, the solar panels, the communication antennas and the radar dipoles are gonna deploy themselves. The battery should be sufficiently charged to survive those first steps. This mode can also be used as a diagnostic mode, if the issues can be corrected, the satellite can move on to the survival mode.

6.5.1.4 Survival mode

The survival mode consist in turning off the radar and the communication system as well as keeping the ADCS and OBC functions to the minimum. This configuration fits the best to charge the battery, the ADCS is still on and keeps correcting the satellite's angle to maximize the solar panels efficiency.

6.5.1.5 Pointing

This short mode take place right before the acquisition mode, the goal is to correctly and precisely direct the radar towards the targets. During this short period of time the ADCS is consuming a lot.

6.5.1.6 Acquisition mode

This is one of the two modes where the radar will be ON, as well as every component excepting the communication antennas. The mode will be activated when the battery will be ready and every parameters will allow optimum measurements. This critical phases is used to emits waves that will be later detected during the reception phases

6.5.1.7 Transmission mode

When the satellite will be at a reasonable distance from the NASA orbiter, it will have to communicate. To realize this, the ADCS will position the antennas correctly and the communication system will be activated. In this configuration, the satellite is also going to be receiving information from the orbiter such as new targets or code correction.

	OFF	IDLE	DETUMBLE	SURVIVAL	ACQUISITION	RECEPTION	POINTING	TRANSMISSION
OBC	Red	Green	Yellow	Yellow	Green	Green	Red	Green
BATTERY	Red	Green	Yellow	Yellow	Green	Green	Yellow	Yellow
ADCS	Red	Red	Yellow	Yellow	Yellow	Red	Red	Yellow
COM	Red	Red	Red	Red	Red	Red	Red	Green
RADAR	Red	Red	Red	Red	Green	Red	Red	Red

Figure 6.16: Synthesis of all components use in the different modes, you can find the detail and the explanation of each mode at 6.5.1. The color green represent a component completely activated, the orange represent a passive or limited state and the red means a component fully off.

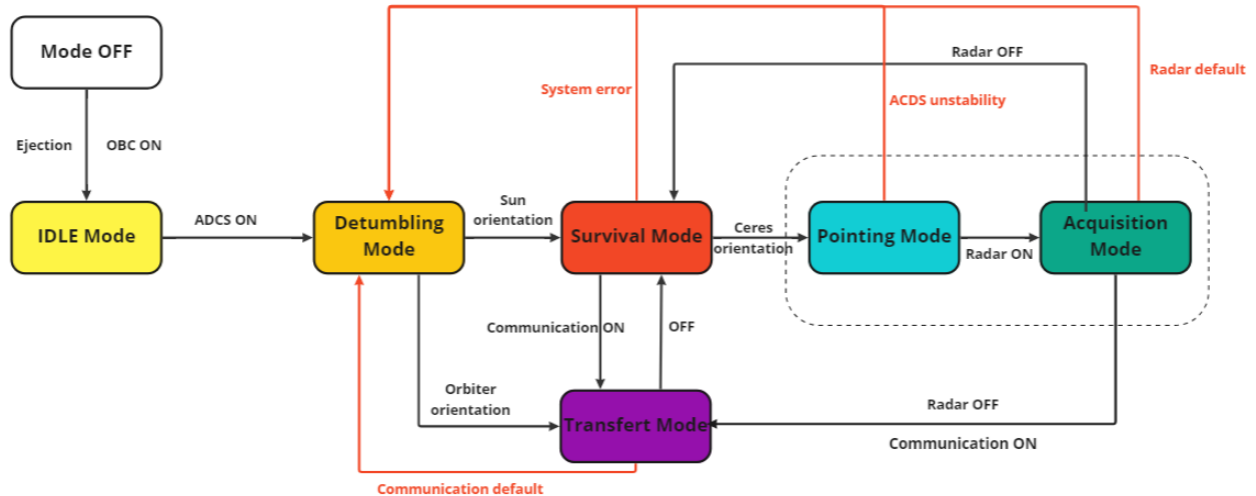


Figure 6.17: Flights modes. We can clearly see how every mode presented is interacting with each other. The red arrows represent the errors that the OBC can detect, it will then automatically in detumbling mode to diagnostic any issues. In this representation, the acquisition mode include the reception of the waves.

6.5.2 Flight management

6.5.2.1 Example of power consumption in a typical orbit

We have modeled a typical orbit with all the different phases: survival, pointing, acquisition, and transmission. We assumed that the battery had 75% power available to keep a margin. This cycle is one of the most critical as it involves a series of energy-intensive phases.

We notice that the available power decreases during the eclipse phase and it will be necessary to consider recharging on several orbits after a certain time. On average one orbit makes us lose 3W. Per day we make a bit more than 9 orbits. In total, we lose 27W per day. An orbit in survival mode allows us to recover about 3 W, so it would take about 9 orbits to recover the energy lost on a day when we made a measurement.

6.6 Planetary Protection Plan

According to the Committee on Space Research (COSPAR) Policy of Planetary Protection, [53], Diploma would be a class II mission. Indeed it will target a body “where there is significant interest relative to the process of chemical evolution and the origin of life, but where there is only a remote chance that contamination carried by spacecraft could compromise future investigations” [53].

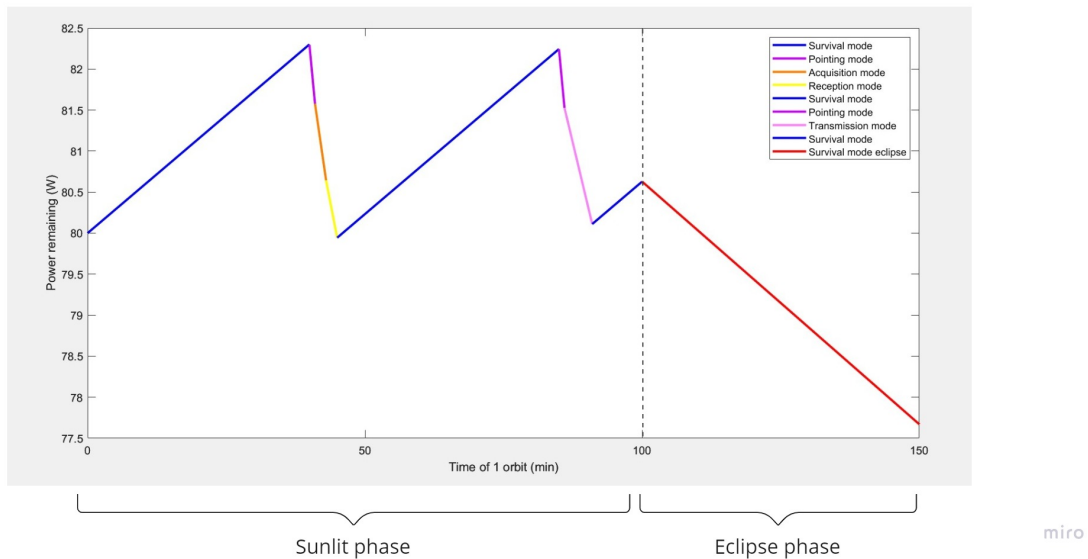


Figure 6.18: Power consumption during all flight modes during one critical orbit, during this exceptionally power consuming orbit the cubesat is using the DRS to perform measurements before transferring data. Hence combining two extremely power consuming modes.

As described before, there is a real interest in Ceres because there may be liquid water under the surface, organics have been detected on the surface, energy sources could be present in the shape of cryovolcanism and this energy would be metabolically useful: the astrobiology interest of Ceres is then extremely high, and we have to ensure that there will be no contaminations provided by our mission. Because our mission is only an orbiter that will execute flybys, there should not be direct contact with the surface so the risk of contamination is low; that is why it is only a class II mission, while the NASA sample returns mission from which we will be piggybacked on will be a class V mission, as it assessed to the questions for the Categorization of Sample Return Missions from Small Solar System Bodies based on the COSPAR Planetary Protection Policy, as a recap in Figure 6.19 reproduced from [15].

The requirements for such a class II mission are not too restrictive; they are for simple documentation only, with a short planetary protection plan, brief Pre- and Post-launch analyses detailing impact strategies, and a Post-encounter and End-of-Mission Report which will provide the location of impact if such an event occurs [53].

However, because we are relying on the NASA mission sample return that will take advantage of a gravity assist of Mars, this could impose more stringent requirements, reclassifying it as a class III mission. Then the documentation should take into account contamination control during the construction of the spacecraft, and an organics inventory of all bulk organic materials and masses used in launched hardware. Implementing procedures such as trajectory biasing, cleanroom, and bioburden reduction could also be set up. Analysis should be done to estimate the probability of impact on Mars; it shall not exceed 10^{-4} for 50 years following launch, and the probability of entry into the Martian atmosphere and impact on the surface shall not exceed 10^{-2} for the first 20 years from the date of launch and 5×10^{-2} from 20 to 50 years from the date to launch [53].

Questions	State of knowledge / Gaps
1 - Does the preponderance of scientific evidence indicate that there was never liquid water in or on the target body?	NO – Ceres has likely had liquid water throughout its history
2 - Does the preponderance of scientific evidence indicate that metabolically useful energy sources were never present?	NO – Ammonium, carbonate, and (likely) organic compounds are found throughout the surface, and there is organic material concentrated locally
3 - Does the preponderance of scientific evidence indicate that there was never sufficient organic matter (or CO ₂ or carbonates and an appropriate source of reducing equivalents) in or on the target body to support life?	NO – There is pervasive evidence for carbonates, high carbon abundance in the regolith, and mineralogy formed under high partial pressure of hydrogen
4 - Does the preponderance of scientific evidence indicate that subsequent to the disappearance of liquid water, the target body has been subjected to extreme temperatures (i.e., >160°C)?	No – There is no such evidence, and Ceres still contains liquid water (below ~40 km thick icy crust)
5 - Does the preponderance of scientific evidence indicate that there is or was sufficient radiation for biological sterilization of terrestrial life forms?	Yes – 99% of the surface has been exposed to sterilizing levels of radiation for >> 100 My No for Occator faculae, which have been exposed for <20 My, some areas <2 My ago
6 - Does the preponderance of scientific evidence indicate that there has been a natural influx to Earth, e.g., via meteorites, of material equivalent to a sample returned from the target body?	Unknown – No confirmed meteorite from Ceres has been found, which may be due to its icy surface (Rivkin et al. 2014). Dust influx cannot be ruled out.

Figure 6.19: Assessment of the questions for the Categorization of Sample Return Missions from Small Solar System Bodies based on the COSPAR Planetary Protection Policy. Reproduced from [15].

Chapter 7

Scientific data management

7.1 Size and shape of data

The scientific data acquired by the radar consist in IF waveform described in section 4.2.2.2. After stretch processing, data are converted by the A/D converter. This process is illustrated by figure 7.1. The data are stored in the form of binary files. We can evaluate the size of these data considering the sampling frequency of 50 MHz, the pulse width of emitted signal of 150 μ s, the pulse repetition frequency which is 20 (values from Table 4.2) and the number of bits of the A/D converter. Data rate (bit/s) = Sampling Frequency (Hz) * Pulse width (s) * Pulse repetition

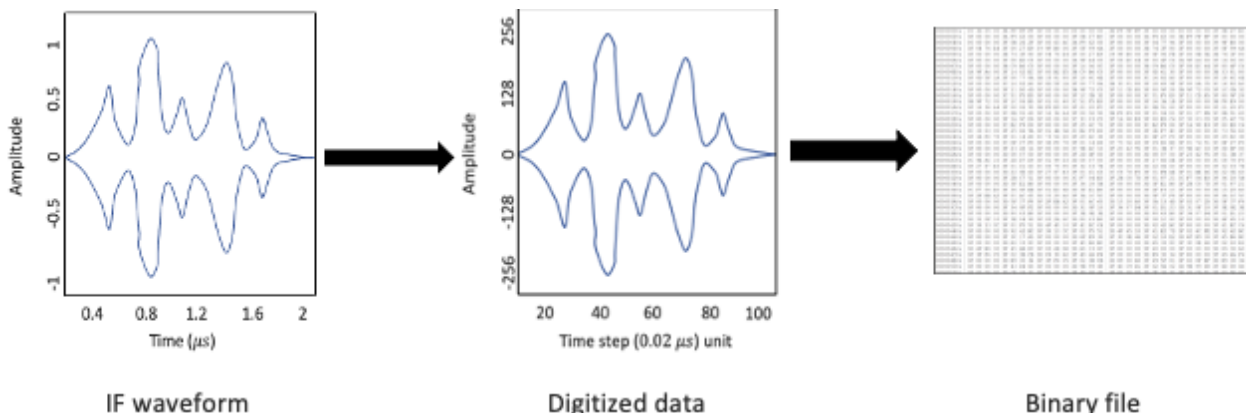


Figure 7.1: Analog to Digital conversion of data.

$$\text{frequency (Hz)} * 8 = 50 * 10^6 * 150 * 10^{-6} * 20 * 8 = 1\ 200\ 000 \text{ bits/s} = 1.2 \text{ Mbits/s}$$

With this estimation, we found a data rate in the range a Mbits/s, while typical values of data rate for other spatial radar during previous missions are in the range of 75 kbit/s for the MARSIS instrument onboard Mars Express spacecraft [54] to 0.5-1 Mbit/s for the SHARAD instrument onboard Mars Reconnaissance Orbiter [55]. The estimation for DRS seems reasonable even if slightly high.

We now that we will spend a maximum of two min for each target. This gives an estimate of the scientific data volume per target that will be produce during our mission :

$$\text{Data volume (bit)} = \text{Data rate (bit/s)} * \text{Acquisition duration (s)} = 1\ 200\ 000 * 120 = 144\ 000\ 000 \text{ bits} = 144 \text{ Mbits.}$$

Note that this value has been obtained considered the largest target above which the satellite will fly over during two minutes. The data volume produced these large targets will be in about 144 Mbits. The total volume of data for the mission will depend on the number of targets and their size. To these scientific data will be added all the data from telemetry, tracking and command interface with the spacecraft, so the total data volume for all the mission will certainly be close to a few Gbits.

7.2 Data chain details

The data obtained with the radar sounder will be stored temporally in the Diplona's spacecraft. Frequently, maybe once a week depending on the energy and on the communication windows, the data collected will be sent to the main satellite of the mission, from which we depend to communicate with the earth. The communication between the two spacecrafts will be made using the Ka-band frequency, between 26.5 and 40 GHz, which will enable us to have a high bandwidth communication [56]. There will be a close collaboration with the mission from whom we will be piggy backing. The data will then be stored in the main spacecraft, where they will wait for a communication window with the Earth to be transmitted. This satellite will use the Deep Space Network (Deep Space Network (DSN)) [57] to downlink the scientific data on Earth. Indeed the DSN is one of the only network able to communicate with interplanetary spacecraft missions, thanks to three antenna spaced about 120° apart in longitude around the world. They are placed near Barstow in California, Madrid in Spain and Canberra in Australia. The communication between the satellite and Earth will be made using the X- (8 to 12 GHz) and Ka-band frequencies. The all data process chain is illustrated on Figure 7.2.

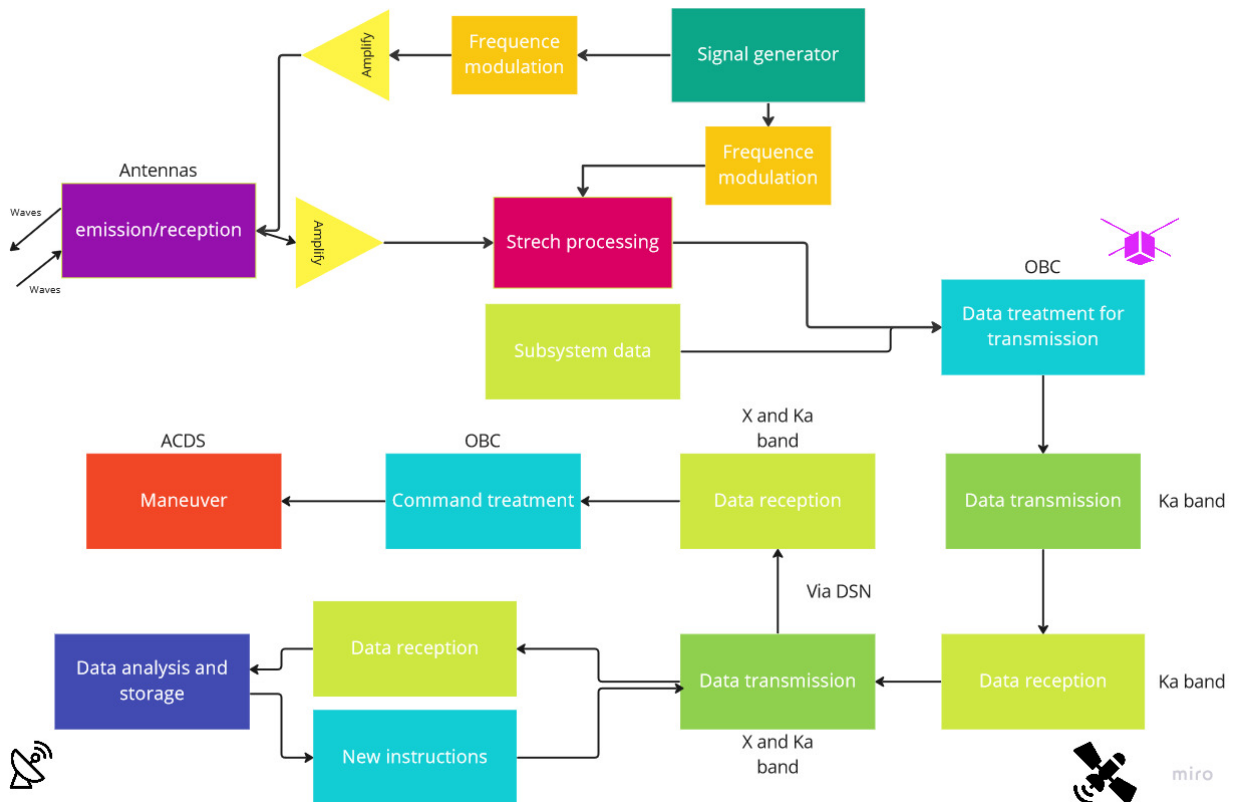


Figure 7.2: Data Management Plan Functional Diagram.

7.3 Post-processing of radargram data

Once the IF waveform data is downlinked and stored as numeric files on Earth, they will be processed and analysed by scientific teams. To do so, a first step is to perform Fourier transform of each IF on the ground, in order to obtain an A-scan plot, or echo power to range plot. By making

a series of A-scan plots obtained in different locations as the spacecraft moves along the orbit, a B-scan plot can be obtain, or depth-to-location plot, which is also called a radargram. This data process is illustrated on Figure 7.3. Data can then be visualised in the shape of radargrams, where each point represent an intensity of reflection at a defined depth.

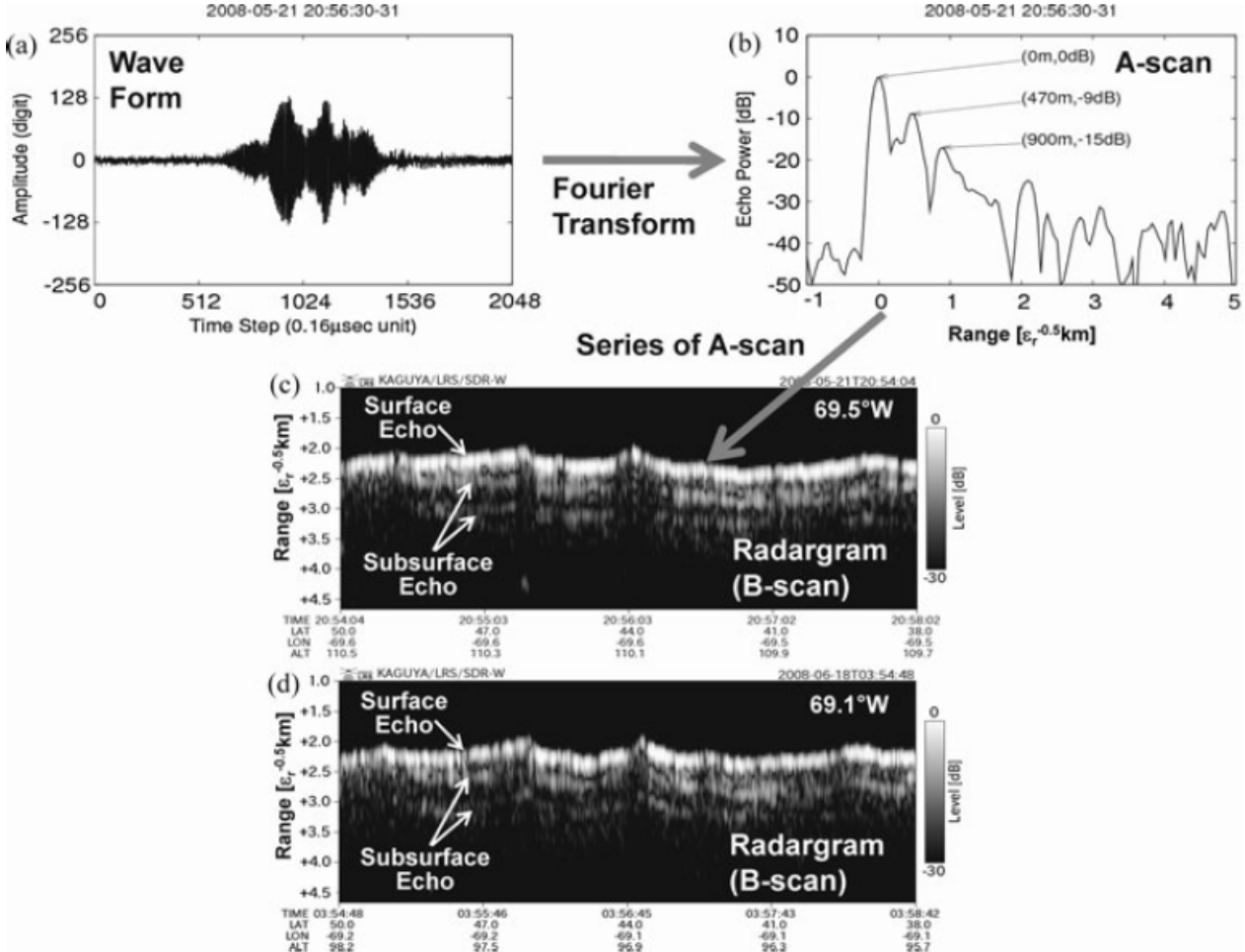


Figure 7.3: (a) The waveform of sounder echo, (b) A-scan plot derived from the waveform data, (c) radargram in longitude of 69.5°W made by series of A-scan plots, and (d) radargram in longitude of 69.1°W . Figure reproduced from [16].

Some steps of post-processing can then be applied in order to facilitate the analysis and interpretation of the radargrams [58]. First of all we apply resampling, in order to resample the radargram scans to a constant number of scans per unit distance before any other signal process. Then other processes can be done. The most basal one is the gain function, illustrated on figure 7.4. As echoes coming from deeper in the subsurface are weaker than echo coming from shallower depth, it may be difficult to distinguish features in the data at later time. We can correct this effect by applying a gain function which increases the amplitude of echo reflectors depending on their time of arrival. Another classical post-processing includes the bandpass filtering that will remove unwanted frequencies in the raw radargrams, by decomposing signals into a combination of individual pure frequencies which have different amplitudes and phases. This can be done with high frequency noises, but for other random smaller noise, when stacked together we can remove the random noises and enhance the small recorded signals as we can see on Figure 7.5. That is methods of smoothing and stacking. Another method will be background removal of the noise. This noise appears across

radargrams as bands of constant horizontal reflections, and to remove them we can calculate the average pulse across the entire radargram and then subtract this average pulse from each individually recorded pulse. Another process would be deconvolution, a signal processing method to help reduce multiple reflections and echoes recorded on radargrams as well as to minimize the effects of the transmitted pulse.

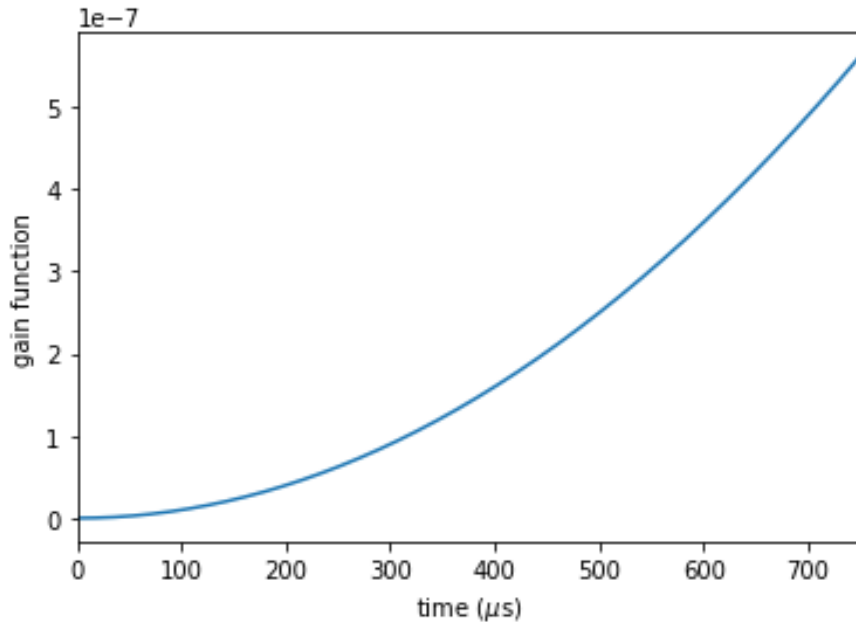


Figure 7.4: Illustration of the gain function. The gain function allows the correction of amplitude of reflectors given their time of arrival.

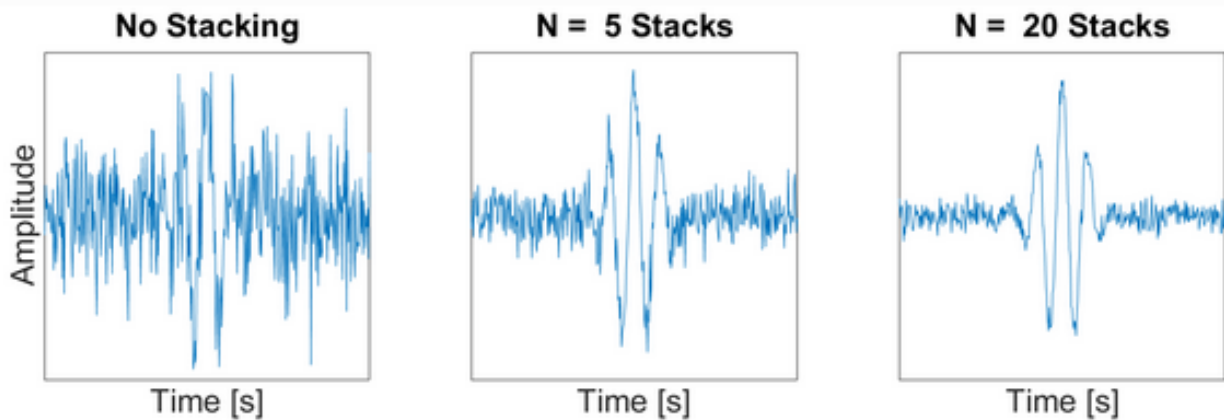


Figure 7.5: Illustration of how stacking improve signal to noise ratio.

There are different softwares to do these post-processings such as RGPR (link to Github) or GeoReader (link to GeoReader website). Because it is very analog to seismic reflection, there is also the possibility to use Seismic Unix to post-process radargram data (link to wiki).

Chapter 8

Mission life cycle, planning and management

Being integrative, collaborative, and multi-faceted in nature, space mission planning and management is an indubitably challenging task. Right from imagining the mission to realization and to the close out of the mission, it has to pass through a lots of activities to achieve the goals and objectives of the mission and planning the project is the key to success of the mission. The management of the project primarily comprises of three major inter-related aspects : managing the technical side of the mission, managing the working teams, and managing the cost and schedule [59].

Seeking a prudent and stabilized planning often gets encountered with numerous constraints: cost, and schedule being the utmost constraint offered to the mission. Furthermore, these constraints are sometimes conflicting and of opposing interests [60]. Our mission Diplona, which is a proposal to NASA SIMPLEx project call in itself bolster specific constraints over Mass and Cost of the mission as presented in detail at section 1.1. Like any other mission, the ability to optimize the overall design, human power, and schedule without compromising the end-goal of the mission will drive the fate of the mission in terms of it's overall cost. And to do so, various teams will work on Diplona co-operatively, namely the scientific team, engineering team and project planning and control team.

The mission starts from a broad spectrum of ideas and with time specifications, simplifications, conceptualization, and realizations are achieved with higher and higher maturity. With the advancement of time, the project needs to enter into specific review and decision points, which is known by mission phases among space exploration community. Looking from the top, there are two phases of mission: project formulation and implementation. During the formulation phase, the following tasks are accomplished; technical study and various alternatives, technological risk assessment and mitigation, preliminary cost and schedule planning, identifying relevant industrial bases and supplier etc. Whereas in the implementation phase; acquisition, detail designing, manufacturing, conducting tests, integration, approval, launching and operations to finally decommissioning are performed. To achieve both the formulation and the implementation in overall, Diplona is being proposed in six phases, namely from Phase A to Phase E.

Apart from the instrument design, fabrication, integration and test cost, the project cost will be dependent to a large extent on project time/schedule and working team hiring. That being the case, the real art of budget planning for the mission would be answering these questions: when, how many and for how much duration. With the target to best optimize every aspect of the mission Diplona, this chapter explains in detail the Diplona schedule and phases, budget required in each phases and overall teams in the subsequent sub-sections of this chapter.

8.1 Scheduling : Mission phases

The project will move through phases as it will progress from concept to operations and finally decommissioning. In view of the fact that Diplona is the response to NASA-SIMPLEX call, Diplona phases nomenclature is adopted same as of the NASA. As it will be a secondary mission to a main big mission, our proposal only concerns until the launch i.e., pre-launch preparation and post-arrival to Ceres. Therefore, during the journey to Ceres, the project will be in dormant stage.

Pre-launch phases includes:

- Phase A: Concept and Technology development,
- Phase B: Preliminary design and technology completion,
- Phase C: Final design and fabrication,
- Phase D: Assembly and Integration.

Post-arrival to Ceres phases:

- Phase E: Operation,
- Phase F: Mission extension.

Figure 8.1 gives the anticipated timelines of each phase. One may argue the four years gap between the main mission launch and Phase D, however it is imperative that this is an anticipated timeline, and main mission launch is also not firmly decided yet, so having a window period of this much is quite insignificant to bother about.



Figure 8.1: Anticipated phase timelines for Diplona. The duration is not to scale.

Routinely it will be evaluated at discrete points to obtain formal approval throughout the progress of the phases which are commonly known by Key Decision Points (KDP) among NASA community. Figure 8.2 shows the KDP with phases and corresponding review steps taken to transfer from one phase to another.

As explained earlier, undoubtedly the project will progress in the expenses of budget. And budget presentation to the approval team will also be the key deciding point. It is of utmost necessity that budgeting is done carefully so as not to under-estimating with the fear of getting rejected and also not to over-estimating to keep large contingency. The Diplona budget is being proposed phase-wise. The successive section discusses in detail the roles to be accomplished in each phase and budget required to execute and progress.

8.2 Phase-wise budget Estimation

There are several methods that various organizations use to estimate the budget for small satellite missions. Some of the most commonly used methods are:

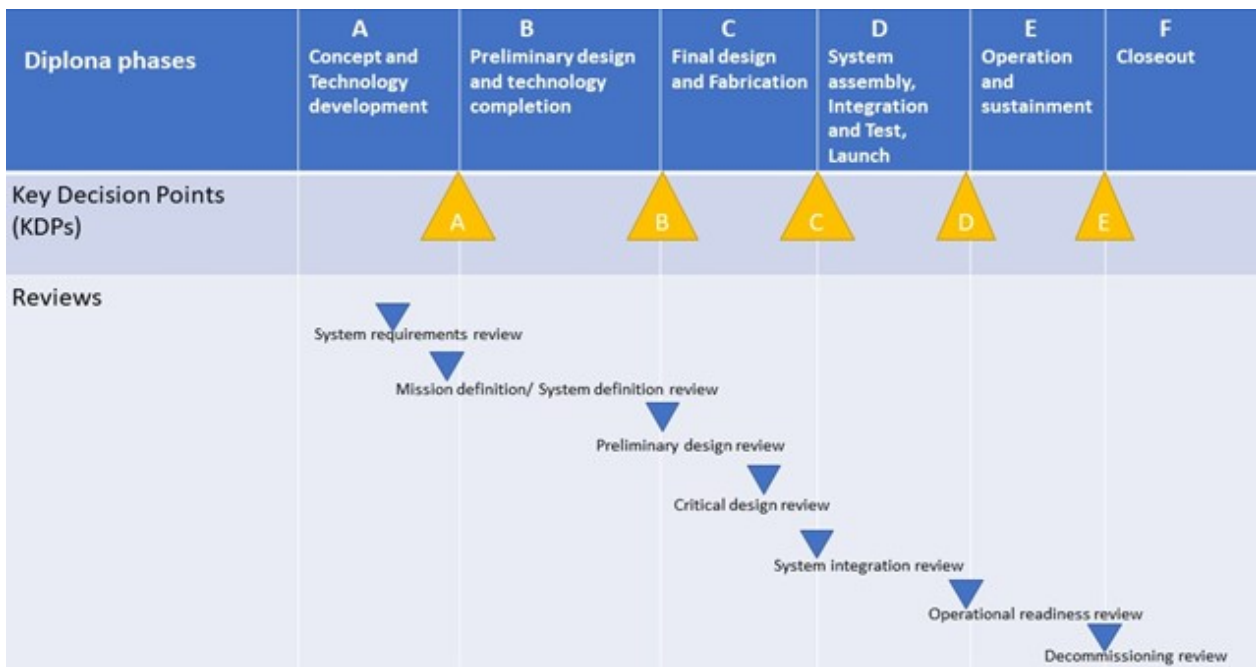


Figure 8.2: Key Decision points and Reviews at each phases and transfers. The picture has been redrawn, reproduced, and adjusted as per Diploma requirements from the NASA project management handbook 2014 version.

1. Bottom-up Estimation: Also known as Grassroots, this method involves breaking down the mission into smaller, more manageable components, and estimating the cost of each component. This provides a detailed and accurate estimate of the mission's cost, but can be time-consuming and requires a great deal of expertise.
2. Top-down Estimation: This method involves starting with a rough estimate of the mission's overall cost, and then breaking it down into smaller components. This method is quicker than the bottom-up method, but is often less accurate.
3. Analogous Estimation: This method involves using the cost of a similar mission to estimate the cost of the new mission. This can be useful when there is limited data on the new mission, but it is important to consider the differences between the two missions, as they may affect the cost estimate.
4. Parametric Estimation: This method uses mathematical models to estimate the cost of a mission based on key parameters such as mission duration, number of satellites, and payload mass. This method can be quick and effective, but it requires accurate data on the mission's parameters.

Owing to the uncertainties, complexity of missions, and lack of data, it is often realized that no single method for budget estimation is perfect because each method has its own strengths and weaknesses, and no method can provide a completely accurate estimate of the cost of a mission. In our proposal also we have used different approaches and tried to estimate the budget by combining mainly Grassroots or bottom-up methods and analogous method. Analogous method has been mainly used for instrument cost. For each phase key areas have been found and the cost of each component has been estimated based on team personnel, hardware, software etc. requirements. In

the subsections following each phase details have been described. Note that large part of information presented in the subsections following are from the NASA project management handbook [59]. And whenever there was a need of human personnel team, we followed the job post level and salaries given by Centre national de la recherche scientifique (CNRS) in France according to Table 8.1.

Post Level	Post name in English.
NC	Researcher
IR	Research Engineers
IE	Study engineers
AI	Assistant Engineers
T	Technicians
Doctoront	PhD/Post-Doc

Table 8.1: Post Level names.

8.2.1 Phase A: Concept and Technology development

This phase will focus on the initial concept and technology development of a mission. During this phase, the team will perform studies and analysis to assess the feasibility of the mission, identify any potential technical or operational risks, and determine the necessary technology developments that need to be made. The outcome of Phase A will be a Concept Study Report, which will provide a detailed assessment of the mission and lay the foundation for future phases of development. We proposed to start Diploma Phase A from October 2023 and lasting for six months. The team consisting of principal Investigator, Deputy PI and Management (Budget, Manager and Purchasing) will remain throughout the mission, in this proposal from now on-wards it will be called the Fixed Team. Along with the fixed team, the teams required in this phase are tabled in Table 8.2. The CNRS level of post and number of such posts required are given in last column of the table. The numbers in brackets is unique code based on the experiences level which will affect the salary of the post. And the number in the start is the actual number of post required. Please note wherever the level of the post has not been defined (written as Level depends) the salary of the post has been estimated from the average salary found on Glass-door in Paris region. After adding everything for six month's Phase A the total estimated budget range is given in the last row of table 8.2.

Tasks to follow	Team required	Post level with number of posts required
Develop mission concept	4 members - Core Science Team	2 NC(1) + 1 NC(2) + Doctoront
Systems engineering study	3 members - Core Engineers Team	1 IR(8) + 1 AI(22) + 1 IE(13)
Collaborating with subject matter experts	2 Subject matter experts	Level depends
Environmental compliance plan	1 Environmental compliance Specialist	Level depends
Reliability plan, quality control plan	1 PA/QA Engineer	Level depends
Outreach and communication Team	3 Members	Level depends
Anticipated phase A Duration : 6 months		
Estimated cost range for phase A : € 0.38-0.53 million		

Table 8.2: Key areas of Phase A and team required.

8.2.2 Phase B: Preliminary design and technology completion

This phase will involve in finalizing the design of the payload, and support systems, as well as finishing any necessary technology developments. The objective of Phase B will be to refine the

mission design, eliminate remaining technical risks, and prove that the required technology can be integrated effectively. The focus will be on completing the preliminary design and verifying the availability of the necessary technology. The outcome of this phase is sought to be a Preliminary Design Review, which would assess the progress of the mission design and confirm that the mission is on course for successful implementation. After Phase A, this phase is expected to start from April 2024 for ten months. Along with the fixed team, the teams required in this phase are tabled in Table 8.3. After adding everything for ten month's Phase B the total estimated budget range is given in the last row of table 8.3.

Tasks to follow	Team required	Post level with number of posts required
Preliminary design	Core+3 member Engineers Team A	TeamA: 1AI(20)+1AI(21)+1IE(15)
Payload(Radar) design	1 Instrument PI	1 IR(7)
Public Outreach Team	3 Members communication and Public team	same from phase A
Environmental compliance plan	1 Environmental compliance Specialist	same from phase A
Reliability plan, quality control plan	1 PA/QA Engineer	same from phase A
Anticipated phase B Duration : 10 months		
Estimated cost range for phase B : € 0.6-0.83 million		

Table 8.3: Key areas of Phase B and team required.

8.2.3 Phase C: Final design and fabrication

During this phase, the mission design will be finalized, and the necessary components and systems will be built. The goal of Phase C would be to develop a complete, verified, and tested design for the mission, including the payload, and ground support systems. The outcome of Phase C will be a Critical Design Review, which will provide a comprehensive evaluation of the mission design, including a detailed assessment of the cost, schedule, and technical feasibility. The results of the Critical Design Review determine whether the mission is ready to proceed to Phase D, which involves the final preparation for launch and mission operations. With the instrument Principal Investigator (PI), the engineers team is proposed to increase by introducing Team B to go forward with the Manufacturing: This team is responsible for building and assembling the components of the mission, payload, and ground support systems. The team may include engineers, technicians, and production specialists. The management team from Fixed team will help in contract, shipments order etc. Diploma phase C is proposed from February 2025 and lasting for about of eleven months. Along with the fixed team, the teams required in this phase are tabled in Table 8.4. After adding everything for eleven month's Phase C the total estimated budget range is given in the last row of table 8.4. For the instrument cost a lump-sum amount of 200000 € has been taken based on previous small sat missions.

Tasks to follow	Team required	Post level with number of posts required
To complete the detailed design	Instrument PI+Engineers Team A+Team B	Team B-4 IR(9)
Manufacturing and assembly	Project Management Team	From Fixed Team
Instrument(Fabrication+Ready-Made)	"	"
Public Outreach Team	3 members communication and Public team	same from phase B
Environmental compliance plan	1 Environmental compliance Specialist	same from phase A
Reliability plan, quality control plan	1 PA/QA Engineer	same from phase A
Anticipated phase C Duration : 11 months		
Estimated cost range for phase C : € 0.91-1.27 million		

Table 8.4: Key areas of Phase C and team required.

8.2.4 Phase D: System Assembly, Integration and Test, Launch

During this phase, the spacecraft and its components are integrated and tested, and the mission is prepared for launch. The goal of Diploma Phase D will be to integrate all of the components of the mission, payload, and ground support systems, and to test the systems to ensure that they are ready for launch. This phase essentially will also include final preparations for mission operations, such as the development of flight software, the establishment of ground stations, and the training of mission personnel. Note that being a piggyback to main mission our phase D timing may change but for now we propose to start our Phase D from December 2025 for 11 months. The outcome of Phase D would be the successful launch of the mission, which marks the beginning of mission operations.

Tasks to follow	Team required	Post level with number of posts required
Integration and test	@LATMOS	NA
Prepare launch, operations	Mission operation manager	1 IR(7)
"	5 members Mission Operation Team	1 NC(3)+1 IE(14)+3 Doct
"	Navigation/Mission Design Team	1 AI(19)+1 IE(13)
Public Outreach Team	3 members communication and Public team	same from phase B
Environmental compliance plan	1 Environmental compliance Specialist	same from phase A
Reliability plan, quality control plan	1 PA/QA Engineer	same from phase A
Anticipated phase D Duration : 11 months		
Estimated cost range for phase D : € 1.04-1.45 million		

Table 8.5: Key areas of Phase D and team required.

In order to test the resistance of the cubesat to the various parameters influencing the optimal use of the nano-satellite, a test phase (Phase D) will be carried out within the Laboratoire Atmosphères, Observations Spatiales (LATMOS). Indeed, it is first necessary to take into account the launch of the rocket containing our cubesat. The relatively powerful vibrations of the launch can damage the structure and the components of the cubesat. A vibrating platform is then used to recreate these vibrations.

The space vacuum is an extremely hostile environment (variable extreme temperatures, radiation, etc.), so it is necessary to perform "ambient" tests in tanks, which recreate the conditions that the cubesat will undergo. The cubesat will be developed in two copies, one which will undergo all the tests presented above and a second which will be launched in order to ensure the mission. Finally, the deployment and more globally the setup of the cubesat is tested in order to evaluate the smooth running and the efficiency of the cubesat. Along with the fixed team, the teams required in this phase are tabled in Table 8.5. After adding everything for eleven month's Phase D the total estimated budget range is given in the last row of table 8.5.

8.2.5 Phase E: Operations and Sustainment

After the long journey of six years to Ceres, if everything goes good Diploma Phase E: Operations and Sustainment will be the final phase of the mission starting from March 2036 for three months of exploration to Ceres. This phase will cover the operational phase of a mission, from launch through the end of the mission's planned activities. During this phase, the satellite will be operated and monitored, and any necessary maintenance and repairs will be performed. The goal of Phase E will be to ensure the continued, successful operation of the mission and to achieve its scientific objectives as described in previous chapters. This may involve a wide range of activities, such as, managing ground communications and data processing, and performing scientific observations and

data analysis. The outcome of Phase E will be the successful completion of the mission, with all of its planned scientific objectives accomplished. Along with the fixed team, the teams required in this phase are tabled in Table 8.6. After adding everything for three month's Phase C the total estimated budget range is given in the last row of table 8.6.

Tasks to follow	Team required	Post level with number of posts required
System operators and maintainers	3 Technicians	1 T(25)+1 T(26)+1 T(27)
Collect engineering and science data	EPS, ACS C-DH	1 IR(8)
"	Radio/Ground communication	1 IR(8)
"	Flight software, Propulsion	1 IR(8)+1 Doct
Process and analyze mission data	Science Core Team	Frome phase A
Public Outreach Team	3 members communication and Public team	same from phase B
Anticipated phase E Duration : 3 months		
Estimated cost range for phase E : € 0.23-0.32 million		

Table 8.6: Key areas of Phase E and team required.

After successful operation and data collection on Ceres, closeout Phase F will be the final phase of the mission, following the successful completion of the mission's objectives and the cessation of mission operations with uncontrolled hitting of the satellite on the surface of Ceres.

In summary Figure 8.3 illustrates the range of budget required in each phase with the total budget range of 3.17-4.4 million euros.

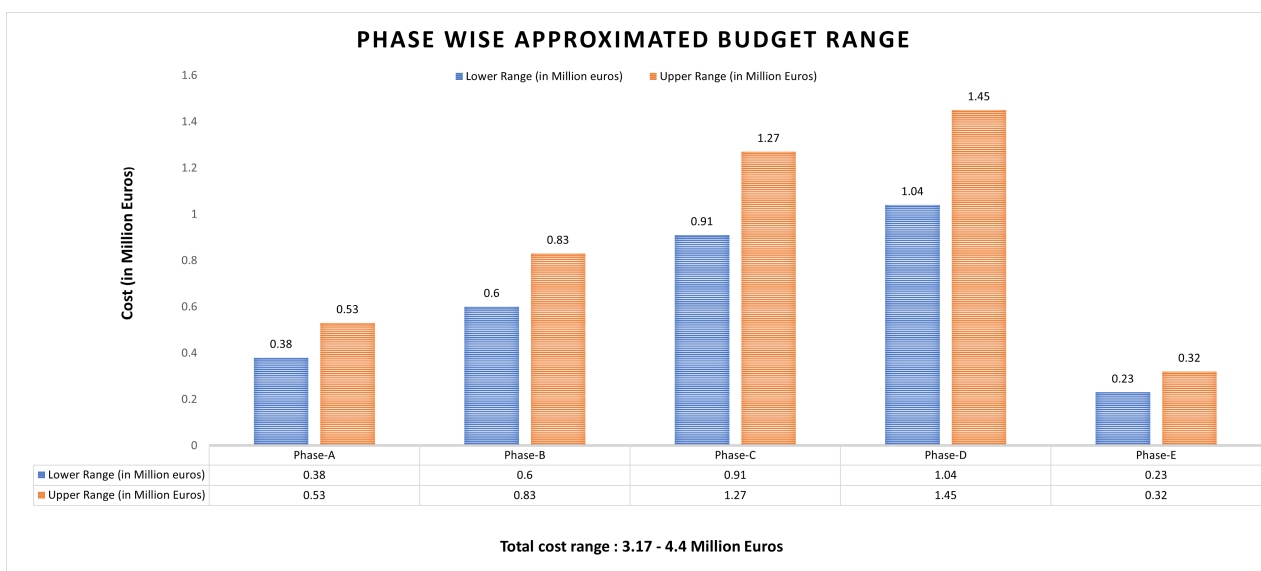


Figure 8.3: Phase wise budget.

The distribution of a mission's budget across different sectors can vary depending on the specifics of the mission and the priorities of the funding agency. However, in general, a significant portion of the budget for a NASA mission is typically allocated to the following sectors:

1. Development and Production: This includes the cost of designing, building, testing, and launching the spacecraft, as well as ground support systems. This is typically the largest single component of a mission's budget.
2. Science Instrumentation: This covers the cost of developing and building the scientific instruments that will be used on the spacecraft to perform observations and gather data.

3. Mission Operations: This covers the cost of operating the spacecraft and monitoring its performance during the mission, including data processing and analysis.
4. Science and Data Analysis: This covers the cost of conducting scientific research and analyzing the data collected by the spacecraft.
5. Program Management: This covers the cost of managing the overall mission, including budgeting, scheduling, and contract management.

Figure 8.4 shows the percentage of total budget across different sectors for our Diploma mission.

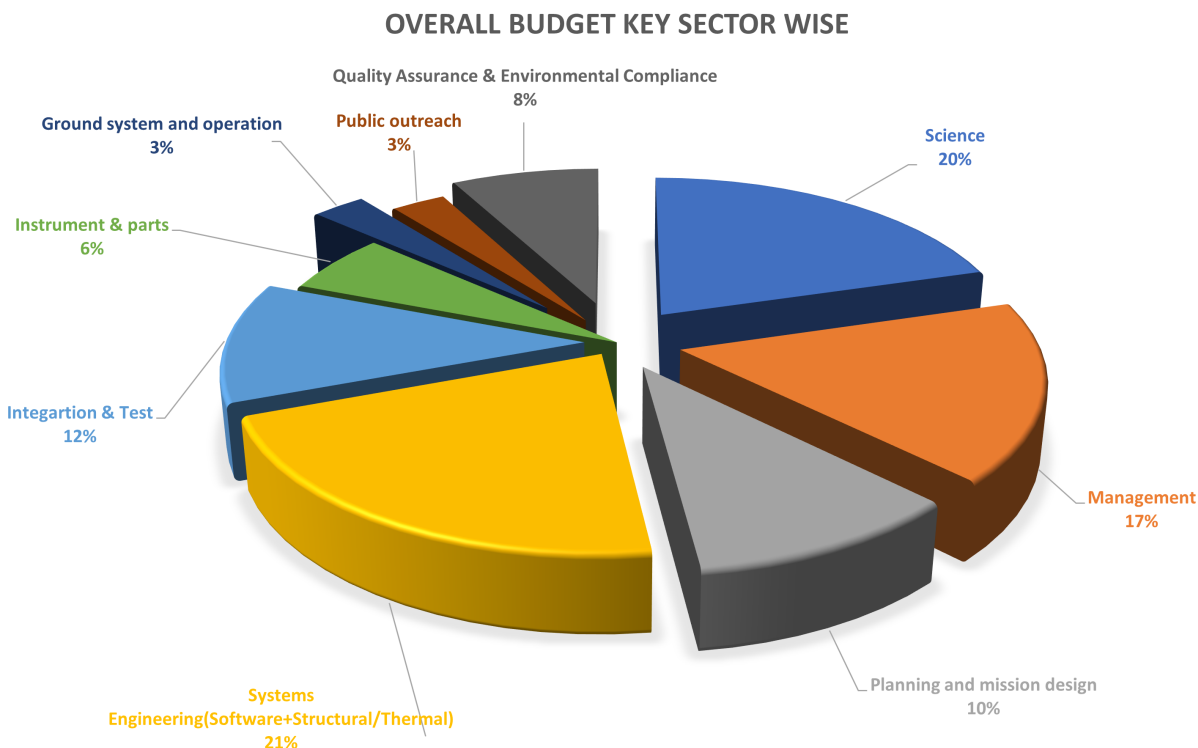


Figure 8.4: Budget percentage sector wise. Note how science and engineering represent half of the total mission budget, including only 6% for components (instrument and parts).

8.3 Diploma overall team

The organizational structure of a space mission team can vary depending on the specifics of the mission and the organization responsible for carrying it out. However, in general, a space mission team will include individuals from a variety of disciplines. Figure 8.5 highlights the organizational chart of Diploma Team members.

Project Management: This team is responsible for overseeing the overall management of the mission, including budgeting, scheduling, and contract management.

Engineering: This team includes individuals with expertise in spacecraft design and development, as well as systems engineering, electrical engineering, and mechanical engineering, computer science engineering etc.

Science: This team includes individuals with expertise in the scientific goals of the mission, such as planetary science, astrophysics, or earth science.

Operations: This team is responsible for operating the spacecraft and monitoring its performance during the mission, including data processing and analysis.

Payload Development: This team is responsible for developing and building the scientific instruments that will be used on the spacecraft.

Mission Assurance: This team is responsible for ensuring that the mission is executed in accordance with established safety, reliability, and quality standards.

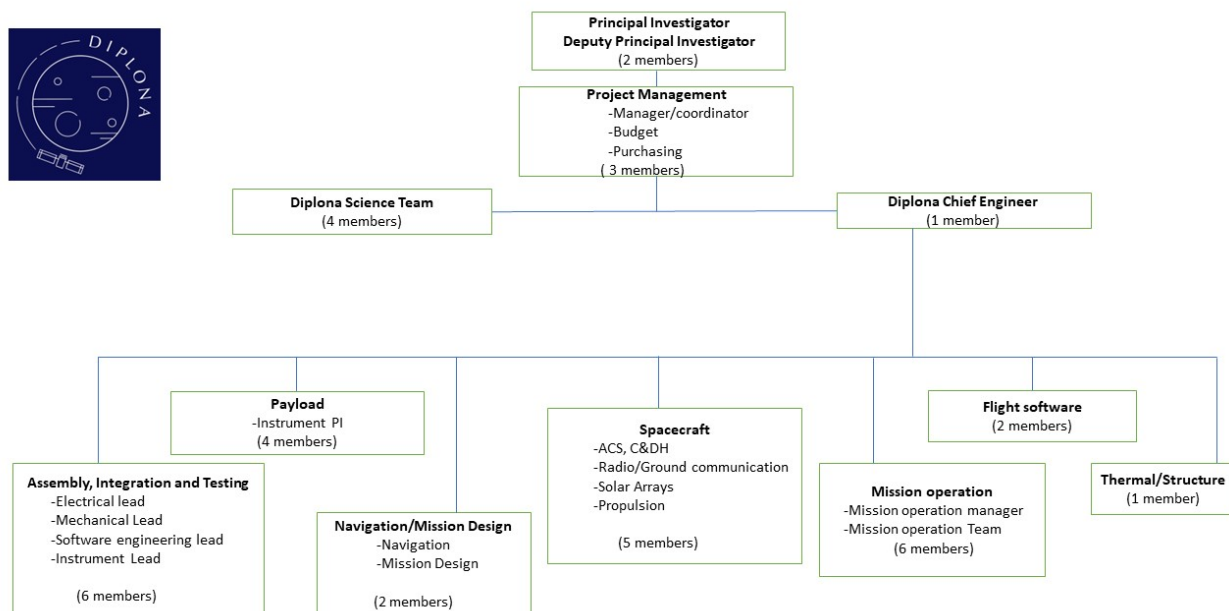


Figure 8.5: DIPLONA overall Team.

Chapter 9

Conclusion

The study of the subsurface of Ceres using the proposed 3U cubesat mission Diploma has the potential to be a valuable and innovative approach in understanding this fascinating dwarf planet. The seven-metre antenna will scan the subsurface of Ceres and highlight the different layers and structures. These scans can then be analysed by scientists to give geological section of the areas. These information will give a new overview of Ceres' surface and subsurface layout.

The main targets have been selected and being proposed in order to answer morphological, chemical or mineralogical details. The four sites proposed - Haulani Crater, Occator Crater, Urvara Crater and Ahuna Mons - will be studied during different orbits of the spacecraft around Ceres to collect data. These orbits will be completed by secondary targets - Juling Crater, Ikapati Crater and Samhain Catena - to increase the scientific interest of the data.

The Diploma mission budget proposed also highlights the feasibility of a low cost mission in direction to Ceres. The radar is one of the most accessible way to study the dwarf planet and obtain relevant and interesting results. Building a radar into a 3U cubesat is an innovative way to study celestial objects and could be a real breakthrough in space exploration at low cost. This study is only the details of a potential phase 0 in the mission development. Once the project submitted to the jury, it would reach the next phases as presented in the project life cycle chapter that are composed of the study of prototype, the construction of the spacecraft and security tests over the instruments across the different phases of the mission.

Moreover, the Ceres Sample Return mission is about to complete Diploma's data by collecting sample of the surface. The comparison of the results would give really interesting information to help answering to aspects such as the presence of a water ocean in subsurface. The Diploma mission would be useful to give some context about the landing site of CSR as it will fly over the site several times.

Our study successfully demonstrates the capability of sending a 3U CubeSat mission to study Ceres and its subsurface using a radar. Through careful planning and execution, we were able to demonstrate the feasibility of using CubeSats for in-depth exploration of celestial bodies. This study provides the valuable insights into the potential of small satellites for improving our understanding of the solar system and has paved the way for further research and development in this field.

Chapter 10

Acknowledgement

We would like to express our sincerest gratitude to all the individuals who have contributed to the success of this space mission to Ceres project. This project has been a thrilling and enriching venture that would not have been possible without the help and support of many dedicated people.

First and foremost, we would like to thank the engineering and planetary science students who worked tirelessly on this project. Their determination, team spirit, and creativity were pivotal in making this mission a mission project that seems consistent with the current state of knowledge on Ceres.

We also want to thank the specialists who brought their expertise and knowledge to the project. Their contribution was invaluable and helped to drive the project forward.

Finally, we would like to thank the engineering school and planetary science master's program that gave us the opportunity to undertake this project. Their support and trust in us was essential in allowing us to realize our vision.

In conclusion, we are deeply grateful to all those who contributed to this project. We hope that our space mission to Ceres will be a success and that we will be able to continue to work together on exciting projects in the future.

Chapter 11

Appendix

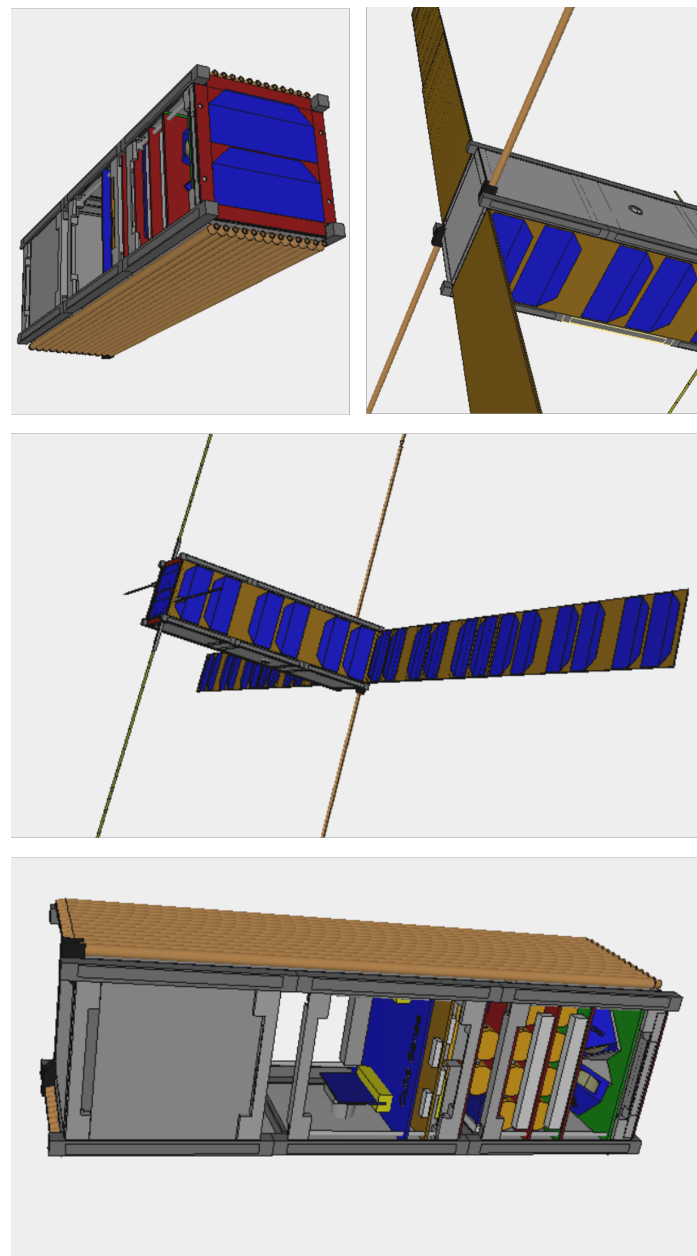


Figure 11.1: Multiple views of Diplona from our IDM CIC model.

Bibliography

- [1] Julie Castillo-Rogez, Henry Hsieh, Hejiu Hui, Wing-Huen Ip, Hanlun Lei, Jian-Yang Li, Federico Tosi, Liyong Zhou, Jessica Agarwal, Antonella Barucci, Pierre Beck, Adriano Campo Bagatin, Fabrizio Capaccioni, Andrew Coates, Gabriele Cremonese, Rene Duffard, Manuel Grande, Ralf Jaumann, Geraint Jones, Esa Kallio, Yangting Lin, Olivier Mousis, Andreas Nathues, Jürgen Oberst, Adam Showman, Holger Sierks, Stephan Ulamec, and Mingyuan Wang. Gauss - genesis of asteroids and evolution of the solar system: A sample return mission to ceres. Technical report, European space agency, Max Planck Institute for Solar System Research, 2020.
- [2] Julie Castillo-Rogez, John Brophy, William Frasier, John Elliott, Jahning Woo, Raul Polit-Casillas, Io Kleiser, Gregory Lantoine, Mineh Vanigh, and Alfred Nash. Exploration of Ceres Habitability - Mission Concept Study. Planetary Mission Concept Study Report, National Aeronautics and Space Administration (NASA), Jet Propulsion Laboratory, California Institute of Technology, 2020. Pre-Decisional Information – For Planning and Discussion Purposes Only.
- [3] Oriane Gassot, Paolo Panicucci, Giacomo Acciarini, Helena Bates, Manel Caballero, Pamela Cambianica, Maciej Dziewiecki, Zelia Dionnet, Florine Engl, Selina-Barbara Gerig, Felix Hessinger, Lucy Kissick, Moritz Novak, Carmine Pellegrino, Angèle Pontoni, Tânia M. Ribeiro, Clemens Riegler, Nini Berge, Nikolaus Huber, Richard Hynek, Bartosz Kędziora, Adam Kiss, Maurice Martin, and Javier Navarro Montilla. Calathus: A sample-return mission to Ceres. *Acta Astronautica*, 181:112–129, April 2021.
- [4] Simone Marchi, Carol A. Raymond, and Christopher T. Russell. Vesta and Ceres. Insights from the Dawn Mission for the Origin of the Solar System. Cambridge University Press, March 2022.
- [5] De Sanctis Maria Cristina, Ammannito E., Raponi Andrea, Marchi S., Mccord Tanya, McSween Harry, Capaccioni Fabrizio, Capria Maria, Carrozzo Filippo, Ciarniello Mauro, Longobardo A., Tosi Federico, Fonte Sergio, Formisano Michelangelo, Frigeri Alessandro, Giardino Marco, Palomba Ernesto, Turrini Diego, and Russell C.T. Ammoniated phyllosilicates with a likely outer solar system origin on (1) ceres. *Nature*, 528:241–244, 12 2015.
- [6] Thomas B. McCord and Christophe Sotin. Ceres: Evolution and current state. *Journal of Geophysical Research: Planets*, 110(E5), 2005.
- [7] David Williams, D.L. Buczkowski, David Crown, Alessandro Frigeri, Kynan Hughson, Thomas Kneissl, Katrin Krohn, Scott Mest, J. Pasckert, Thomas Platz, Ottaviano Ruesch, Franziska Schulzeck, C.T. Russel, H. Sizemore, Andrea Nass, Ralf Jaumann, and C. Raymond. Final dawn lam-based global geologic map of ceres. 01 2019.
- [8] H. Hiesinger, S. Marchi, N. Schmedemann, P. Schenk, J. H. Pasckert, A. Neesemann, D. P. O'Brien, T. Kneissl, A. I. Ermakov, R. R. Fu, M. T. Bland, A. Nathues, T. Platz, D. A. Williams, R. Jaumann, J. C. Castillo-Rogez, O. Ruesch, B. Schmidt, R. S. Park, F. Preusker, D. L. Buczkowski, C. T. Russell, and C. A. Raymond. Cratering on ceres: Implications for its crust and evolution. *Science*, 353(6303):aaf4759, 2016.
- [9] K. D. Duarte, B. E. Schmidt, H. T. Chilton, K. H. G. Hughson, H. G. Sizemore, K. L. Ferrier, J. J. Buffo, J. E. C. Scully, A. Nathues, T. Platz, M. Landis, S. Byrne, M. Bland,

- C. T. Russell, and C. A. Raymond. Landslides on Ceres: Diversity and Geologic Context. *Journal of Geophysical Research: Planets*, 124(12):3329–3343, 2019. _eprint: <https://agupubs.onlinelibrary.wiley.com/doi/pdf/10.1029/2018JE005673>.
- [10] Indujaa Ganesh, Lynn M. Carter, and Isaac B. Smith. Sharad mapping of arsia mons caldera. *Journal of Volcanology and Geothermal Research*, 390:106748, 2020.
- [11] J. E. C. Scully, P. M. Schenk, J. C. Castillo-Rogez, D. L. Buczkowski, D. A. Williams, J. H. Pasckert, K. D. Duarte, V. N. Romero, L. C. Quick, M. M. Sori, M. E. Landis, C. A. Raymond, A. Neesemann, B. E. Schmidt, H. G. Sizemore, and C. T. Russell. The varied sources of faculae-forming brines in Ceres' Occator crater emplaced via hydrothermal brine effusion. *Nature Communications*, 11(1):3680, August 2020. Number: 1 Publisher: Nature Publishing Group.
- [12] O. Ruesch, T. Platz, P. Schenk, L. A. McFadden, J. C. Castillo-Rogez, L. C. Quick, S. Byrne, F. Preusker, D. P. O'Brien, N. Schmedemann, D. A. Williams, J.-Y. Li, M. T. Bland, H. Hiesinger, T. Kneissl, A. Neesemann, M. Schaefer, J. H. Pasckert, B. E. Schmidt, D. L. Buczkowski, M. V. Sykes, A. Nathues, T. Roatsch, M. Hoffmann, C. A. Raymond, and C. T. Russell. Cryovolcanism on ceres. *Science*, 353, 2016.
- [13] K. Krohn, R. Jaumann, K. A. Otto, F. Schulzeck, A. Neesemann, A. Nass, K. Stephan, F. Tosi, R. J. Wagner, F. Zambon, I. von der Gathen, D. A. Williams, D. L. Buczkowski, M. C. De Sanctis, E. Kersten, K. D. Matz, S. C. Mest, C. M. Pieters, F. Preusker, T. Roatsch, J. E. C. Scully, C. T. Russell, and C. A. Raymond. The unique geomorphology and structural geology of the Haulani crater of dwarf planet Ceres as revealed by geological mapping of equatorial quadrangle Ac-6 Haulani. *Icarus*, 316:84–98, December 2018.
- [14] David A. Crown, Hanna G. Sizemore, R. Aileen Yingst, Scott C. Mest, Thomas Platz, Daniel C. Berman, Nico Schmedemann, Debra L. Buczkowski, David A. Williams, Thomas Roatsch, Frank Preusker, Carol A. Raymond, and Christopher T. Russell. Geologic mapping of the Urvara and Yalode Quadrangles of Ceres. *Icarus*, 316:167–190, December 2018.
- [15] J. C. Castillo-Rogez, John Brody, Michael T. Bland, Debra Buczkowski, Robert Grimm, A. Hendrix, Kelly Miller, Thomas Prettyman, Lynnae Quick, Carol Raymond, Jennifer Scully, Michael M. Sori, Yasuhito Sekine, David Williams, and Michael Zolensky. Planetary science decadal survey planetary mission concept study report: Ceres: Exploration of ceres' habitability. Report Federal Government Series, 2020.
- [16] T. Ono, A. Kumamoto, Y. Kasahara, Y. Yamaguchi, A. Yamaji, T. Kobayashi, S. Oshigami, H. Nakagawa, Y. Goto, K. Hashimoto, Y. Omura, T. Imachi, H. Matsumoto, and H. Oya. The lunar radar sounder (lrs) onboard the kaguya (selene) spacecraft. *Space Science Reviews*, 154(1-4):145–192, July 2010.
- [17] Alex S. Konopliv, Ryan S. Park, Andrew T. Vaughan, Bruce G. Bills, Sami W. Asmar, Anton I. Ermakov, N. Rambaux, Carol A. Raymond, Julie C. Castillo-Rogez, Christopher T. Russell, David E. Smith, and Maria T. Zuber. The ceres gravity field, spin pole, rotation period and orbit from the dawn radiometric tracking and optical data. *Icarus*, 299:411–429, 2018.
- [18] Thomas B. McCord and Francesca Zambon. The surface composition of ceres from the dawn mission. *Icarus*, 318:2–13, 2019. The Composition of Ceres.
- [19] Jian Yang Li, Vishnu Reddy, Andreas Nathues, Lucille Le Corre, Matthew R.M. Izawa, Edward A. Cloutis, Mark V. Sykes, Uri Carsenty, Julie C. Castillo-Rogez, Martin Hoffmann,

- Ralf Jaumann, Katrin Krohn, Stefano Mottola, Thomas H. Prettyman, Michael Schaefer, Paul Schenk, Stefan E. Schröder, David A. Williams, David E. Smith, Maria T. Zuber, Alexander S. Konopliv, Ryan S. Park, Carol A. Raymond, and Christopher T. Russell. Surface albedo and spectral variability of ceres. *Astrophysical Journal Letters*, 817(2), February 2016. Publisher Copyright: © 2016. The American Astronomical Society. All rights reserved..
- [20] Maria Cristina De Sanctis, Eleonora Ammannito, Harry Y. McSween, Andrea Raponi, Simone Marchi, Fabrizio Capaccioni, Maria Teresa Capria, Filippo Giacomo Carrozzo, Mauro Ciarniello, Sergio Fonte, Michelangelo Formisano, Alessandro Frigeri, Marco Giardino, Alessia Longobardo, Gianfranco Magni, L.A. McFadden, Ernesto Palomba, Carle M. Pieters, Federico Tosi, Francesca Zambon, Carol A. Raymond, and Christopher T. Russell. Localized aliphatic organic material on the surface of ceres. *Science*, 355:719 – 722, 2017.
 - [21] M. C. De Sanctis, A. Raponi, E. Ammannito, M. J. Toplis M. Ciarniello, J. C. Castillo-Rogez H. Y. McSween, B. L. Ehlmann, F. G. Carrozzo, S. Marchi, F. Tosi, F. Zambon, F. Capaccioni, M. T. Capria, S. Fonte, M. Formisano, A. Frigeri, M. Giardino, A. Longobardo, G. Magni, E. Palomba, L. A. McFadden, C. M. Pieters, R. Jaumann, P. Schenk, R. Mugnuolo, C. A. Raymond, and C. T. Russell. Bright carbonate deposits as evidence of aqueous alteration on (1) ceres. *Nature*, 536, 2016. The Composition of Ceres.
 - [22] Elodie Lesage, Frédéric Schmidt, François Andrieu, and Hélène Massol. Constraints on effusive cryovolcanic eruptions on europa using topography obtained from galileo images. *Icarus*, 361, 2021.
 - [23] O. Ruescha, L.C. Quickc, M.E. Landis, M.M. Sori, O. Cadek, P. Brožf, K.A. Ottog, M.T. Bland, S. Byrne, J.C. Castillo-Rogezi, R. Jaumanng H. Hiesinger and, L.A. McFaddenk, A. Nathues, A. Neesemann, F. Preusker, T. Roatschg, P.M. Schenk, J.E.C. Scullyi, M.V. Sykes, D.A. Williams, C.A. Raymondi, and C.T. Russell. Bright carbonate surfaces on ceres as remnants of salt-rich water fountains. *Icarus*, 320, 2019.
 - [24] Marchi S, Ermakov AI, Raymond CA, Fu RR, O'Brien DP, Bland MT, Ammannito E, De Sanctis MC, Bowling T, Schenk P, Scully JE, Buczkowski DL, Williams DA, Hiesinger H, and Russell CT. The missing large impact craters on ceres. *Nature Communications*, 2016.
 - [25] D. L. Buczkowski, B. E. Schmidt, D. A. Williams, S. C. Mest, J. E. C. Scully, A. I. Ermakov, F. Preusker, P. Schenk, K. A. Otto, H. Hiesinger, D. O'Brien, S. Marchi, H. Sizemore, K. Hughson, H. Chilton, M. Bland, S. Byrne, N. Schorghofer, T. Platz, R. Jaumann, T. Roatsch, M. V. Sykes, A. Nathues, M. C. De Sanctis, C. A. Raymond, and C. T. Russell. The geomorphology of ceres. *Science*, 353(6303):aaf4332, 2016.
 - [26] A. I. Ermakov, R. R. Fu, J. C. Castillo-Rogez, C. A. Raymond, R. S. Park, F. Preusker, C. T. Russell, D. E. Smith, and M. T. Zuber. Constraints on ceres' internal structure and evolution from its shape and gravity measured by the dawn spacecraft. *Journal of Geophysical Research: Planets*, 122(11):2267–2293, 2017.
 - [27] M. T. Bland, C. A. Raymond, R. Fu, S. Marchi, J. C. Castillo, S. D. King, P. Schenk, F. Preusker, R. S. Park, and C. T. Russell. Is Ceres' deep interior ice-rich? Constraints from crater morphology. In AGU Fall Meeting Abstracts, pages P43C–2118, December 2016.
 - [28] Roger R. Fu, Anton I. Ermakov, Simone Marchi, Julie C. Castillo-Rogez, Carol A. Raymond, Bradford H. Hager, Maria T. Zuber, Scott D. King, Michael T. Bland, Maria Cristina De Sanctis, Frank Preusker, Ryan S. Park, and Christopher T. Russell. The interior structure of ceres as revealed by surface topography. *Earth and Planetary Science Letters*, 476, 2017.

- [29] Rafael Ribeiro de Sousa, Alessandro Morbidelli, Rodney Gomes, Ernesto Vieira Neto, Andre Izidoro, and Abreuçon Atanasio Alves. Dynamical origin of the dwarf planet ceres. *Icarus*, 379:114933, 2022.
- [30] Committee on the Planetary Science and Astrobiology Decadal Survey, Space Studies Board, Division on Engineering and Physical Sciences, and National Academies of Sciences, Engineering, and Medicine. *Origins, Worlds, and Life: A Decadal Strategy for Planetary Science and Astrobiology 2023-2032*. National Academies Press, Washington, D.C., 2022. Pages: 26522.
- [31] Robert Grimm, Julie Castillo-Rogez, Carol Raymond, and Andrew R. Poppe. Feasibility of characterizing subsurface brines on Ceres by electromagnetic sounding. *Icarus*, 362:114424, July 2021.
- [32] Jesper Lindkvist, Mats Holmström, Shahab Fatemi, Martin Wieser, and Stas Barabash. Ceres interaction with the solar wind. *Geophysical Research Letters*, 44(5):2070–2077, 2017. _eprint: <https://agupubs.onlinelibrary.wiley.com/doi/pdf/10.1002/2016GL072375>.
- [33] Roberto Seu, Roger J. Phillips, Daniela Biccari, Roberto Orosei, Arturo Masdea, Giovanni Picardi, Ali Safaeinili, Bruce A. Campbell, Jeffrey J. Plaut, Lucia Marinangeli, Suzanne E. Smrekar, and Daniel C. Nunes. Sharad sounding radar on the mars reconnaissance orbiter. *Journal of Geophysical Research: Planets*, 112(E5), 2007.
- [34] R. Jordan, G. Picardi, J. Plaut, K. Wheeler, D. Kirchner, A. Safaeinili, W. Johnson, R. Seu, D. Calabrese, E. Zampolini, A. Cicchetti, R. Huff, D. Gurnett, A. Ivanov, W. Kofman, R. Orosei, T. Thompson, P. Edenhofer, and O. Bombaci. The mars express marsis sounder instrument. *Planetary and Space Science*, 57(14):1975–1986, 2009.
- [35] Takayuki Ono, Atsushi Kumamoto, Hiromu Nakagawa, Yasushi Yamaguchi, Shoko Osahigami, Atsushi Yamaji, Takao Kobayashi, Yoshiya Kasahara, and Hiroshi Oya. Lunar radar sounder observations of subsurface layers under the nearside maria of the moon. *Science*, 323(5916):909–912, 2009.
- [36] T. Kobayashi, S. R. Lee, A. Kumamoto, and T. Ono. Gpr observation of the moon from orbit: Kaguya lunar radar sounder. In *Proceedings of the 15th International Conference on Ground Penetrating Radar*, pages 1037–1041, 2014.
- [37] T. Kaku, J. Haruyama, W. Miyake, A. Kumamoto, K. Ishiyama, T. Nishibori, K. Yamamoto, Sarah T. Crites, T. Michikami, Y. Yokota, R. Sood, H. J. Melosh, L. Chappaz, and K. C. Howell. Detection of intact lava tubes at marius hills on the moon by selene (kaguya) lunar radar sounder. *Geophysical Research Letters*, 44(20):10,155–10,161, 2017.
- [38] Takao Kobayashi, Jung Ho Kim, Seung Ryeol Lee, Hiroshi Araki, and Takayuki Ono. Simultaneous observation of lunar radar sounder and laser altimeter of kaguya for lunar regolith layer thickness estimate. *IEEE Geoscience and Remote Sensing Letters*, 7(3):435–439, 2010.
- [39] Lorenzo Bruzzone and Renato Croci. Radar for icy moon exploration (rime). In *2019 IEEE 5th International Workshop on Metrology for AeroSpace (MetroAeroSpace)*, pages 330–333, 2019.
- [40] Essam Heggy, Giovanni Scabbia, Lorenzo Bruzzone, and Robert T. Pappalardo. Radar probing of jovian icy moons: Understanding subsurface water and structure detectability in the juice and europa missions. *Icarus*, 285:237–251, 2017.

- [41] Mark S. Haynes. Surface and subsurface radar equations for radar sounders. *Annals of Glaciology*, 61(81):135–142, 2020.
- [42] Marco Mastrogiovanni. Dual frequency orbiter-radar system for the observation of seas and tides on titan: Extraterrestrial oceanography from satellite. *Remote Sensing*, 11:1898, 08 2019.
- [43] R. Jordan, G. Picardi, J. Plaut, K. Wheeler, D. Kirchner, A. Safaeinili, W. Johnson, R. Seu, D. Calabrese, E. Zampolini, A. Cicchetti, R. Huff, D. Gurnett, A. Ivanov, W. Kofman, R. Orosei, T. Thompson, P. Edenhofer, and O. Bombaci. The mars express marsis sounder instrument. *Planetary and Space Science*, 57(14):1975–1986, 2009.
- [44] Jan Hendrik Pasckert, Nico Schmedemann, Andreas Nathues, Harald Hiesinger, and Carolyn H. van der Bogert. The young resurfacing events at Ceres’ Occator Crater: Seismic shaking or deposition of cryovolcanic material? *Icarus*, 389:115259, January 2023.
- [45] D. L. Buczkowski, B. E. Schmidt, M. E. Landis, J. E. C. Scully, K. H. G. Hughson, P. M. Schenk, T. H. Prettyman, J. C. Castillo-Rogez, C. A. Raymond, and C. T. Russell. Fractures and Furrows on Lobate Flows in Occator Crater, Ceres: Morphologic Evidence of Ice Content. 52nd Lunar and Planetary Science Conference, page 1765, March 2021.
- [46] D. L. Buczkowski, D. A. Williams, J. E. C. Scully, S. C. Mest, D. A. Crown, P. M. Schenk, R. Jaumann, T. Roatsch, F. Preusker, A. Nathues, M. Hoffmann, M. Schaefer, S. Marchi, M. C. De Sanctis, C. A. Raymond, and C. T. Russell. The geology of the occator quadrangle of dwarf planet Ceres: Floor-fractured craters and other geomorphic evidence of cryomagma-tism. *Icarus*, 316:128–139, December 2018.
- [47] F. Zambon, A. Raponi, F. Tosi, M. C. De Sanctis, L. A. McFadden, F. G. Carrozzo, A. Longobardo, M. Ciarniello, K. Krohn, K. Stephan, E. Palomba, C. M. Pieters, E. Ammannito, C. T. Russell, and C. A. Raymond. Spectral analysis of Ahuna Mons from Dawn mission’s visible-infrared spectrometer. *Geophysical Research Letters*, 44(1):97–104, 2017. _eprint: <https://onlinelibrary.wiley.com/doi/pdf/10.1002/2016GL071303>.
- [48] Jian-Yang Li, Lucy A. McFadden, Joel Wm. Parker, Eliot F. Young, S. Alan Stern, Peter C. Thomas, Christopher T. Russell, and Mark V. Sykes. Photometric analysis of 1 ceres and surface mapping from hst observations. *Icarus*, 182(1):143–160, 2006.
- [49] F. Tosi, F. G. Carrozzo, A. Raponi, M. C. De Sanctis, G. Thangjam, F. Zambon, M. Ciarniello, A. Nathues, M. T. Capria, E. Rognini, E. Ammannito, M. Hoffmann, K. Krohn, A. Longobardo, E. Palomba, C. M. Pieters, K. Stephan, C. A. Raymond, and C. T. Russell. Mineralogy and temperature of crater Haulani on Ceres. *Meteoritics & Planetary Science*, 53(9):1902–1924, 2018. _eprint: <https://onlinelibrary.wiley.com/doi/pdf/10.1111/maps.13078>.
- [50] A. Longobardo, A. Galiano, E. Ammannito, F. G. Carrozzo, M. C. De Sanctis, E. Palomba, F. Zambon, A. Frigeri, M. Ciarniello, A. Raponi, F. Tosi, M. T. Capria, K. Stephan, C. A. Raymond, and C. T. Russell. Mineralogy of the Urvara–Yalode region on Ceres. *Icarus*, 318:241–250, January 2019.
- [51] A. Nathues, M. Hoffmann, N. Schmedemann, R. Sarkar, G. Thangjam, K. Mengel, J. Hernandez, H. Hiesinger, and J. H. Pasckert. Brine residues and organics in the Urvara basin on Ceres. *Nature Communications*, 13(1):927, February 2022. Number: 1 Publisher: Nature Publishing Group.

- [52] D. Y. Wyrick and D. L. Buczkowski. Pit Crater Chains Across the Solar System: Evidence for Subterranean Tectonic Caves, Porosity and Permeability Pathways on Planetary Bodies. *Journal of Geophysical Research: Planets*, 127(12):e2022JE007281, 2022. _eprint: <https://agupubs.onlinelibrary.wiley.com/doi/pdf/10.1029/2022JE007281>.
- [53] COPSPAR Panel on Planetary Protection. Cospar policy on planetary protection approved on 3 june 2021. COSPAR, 2021.
- [54] MARSIS Instrument Information - PDS NASA website. https://pds.nasa.gov/ds-view/pds/viewInstrumentProfile.jsp?INSTRUMENT_ID=MARSIS&INSTRUMENT_HOST_ID=MEX.
- [55] SHARAD Instrument Information - PDS NASA website. https://pds.nasa.gov/ds-view/pds/viewInstrumentProfile.jsp?INSTRUMENT_ID=SHARAD&INSTRUMENT_HOST_ID=MRO.
- [56] Satellite frequency bands - ESA website. https://www.esa.int/Applications/Telecommunications_Integrated_Applications/Satellite_frequency_bands.
- [57] Deep Space Network - NASA website. <https://www.jpl.nasa.gov/missions/dsn>.
- [58] Daniel R. Nüesch and Erich H. Meier. Radar post-processing. In F. Toselli, editor, Applications of Remote Sensing to Agrometeorology, pages 181–197, Dordrecht, 1989. Springer Netherlands.
- [59] Expanded Guidance for NASA Systems Engineering 2016 Version .
- [60] NASA Space Flight Program and Project Management Handbook 2014 version.